The onset of bubble vibration

ISBN 978-90-9023828-9

The movie depicted in the footnote was made with the Brandaris 128 and shows a SonoVue microbubble with a size of 4.3 μm diameter insonified with a frequency of 1.7 MHz and an acoustic pressure of 80 kPa (see chapter 10).

Cover design by Pascale Petitiaux.
Printed in the Netherlands by Optima Grafische Communicatie, Rotterdam.

The onset of bubble vibration

Het begin van belvibratie

Proefschrift

ter verkrijging van de graad van doctor aan de Erasmus Universiteit Rotterdam op gezag van de rector magnificus, Prof.dr. S.W.J. Lamberts, en volgens besluit van het College voor Promoties.

De openbare verdediging zal plaatsvinden op vrijdag 23 januari 2009 om 16:00 uur door

Marcia Emmer

geboren te Heerhugowaard

Promotiecommissie

Promotoren:	Prof.dr.ir. N. de Jong Prof.dr.ir. A.F.W. van der Steen
Overige Leden:	Prof.dr.ir. M. de Jong Prof.dr. P.N. Burns Dr. A.M. Versluis

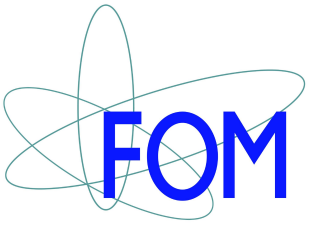

The research described in this thesis is part of the research program of the 'Stichting voor Fundamenteel Onderzoek der Materie' (FOM) which is financially supported by the 'Nederlandse Organisatie voor Wetenschappelijk Onderzoek' (NWO). It was carried out at the department of Biomedical Engineering of the Erasmus Medical Center in Rotterdam, the Netherlands.

Contents

List of symbols

b	Constant	-
c	Speed of sound	m s^{-1}
C	Compression amplitude	-
C_s	Constant	-
d	Thickness	m
D	Bubble diameter	m
D_{th}	Thermal diffusivity	m^2 s^{-1}
E	Expansion amplitude	-
E_k	Kinetic energy	N m
G_s	Shell shear modulus	Pa
I	Pixel intensity	-
K	Power law constant	N $m^{2(y-1)}$
K_V	Compression modulus	Pa
M	Mach number	-
$P(t)$	Acoustic driving pressure	Pa
P_s	Scattered sound pressure	Pa
p	Pressure	Pa
R	Bubble radius	m
$R_{buckling}$	Below this radius, the surface buckles and $\sigma = 0$	m
$R_{rupture}$	Above this radius, the surface ruptures and $\sigma = \sigma_w$	m
Re_l	Reynolds number	-
r	Radial distance	m
S_f	Shell friction parameter	N s m^{-1}
S_p	Shell elasticity parameter	N m^{-1}
t	Time	s
V	Volume	m^3
We	Weber number	-
y	Power law exponent	-
Z	Surface viscosity exponent	-

δ	Damping	-
Γ	Surface molecular concentration	m^2
γ	Interfacial tension	N m^{-1}
κ	Polytropic gas exponent	-
κ_s	Shell viscosity parameter	kg s^{-1}
λ	Relaxation time	s
μ	Dynamic viscosity	Pa s
ρ	Density	kg m^{-3}
σ	Surface tension	N m^{-1}
$\sigma_{break-up}$	Surface tension where surface ruptures	N m^{-1}
χ	Shell elasticity parameter	N m^{-1}
ω	Angular frequency	rad s^{-1}

Superscript

$\dot{}$	Time derivative
$\ddot{}$	Second time derivative

Subscript

ac	Acoustic
e	Equilibrium
g	Gas
i	Internal
l	Liquid
s	Shell
w	Water
∞	Infinity
0	Initial, resting state
1	Inner
2	Outer

1 Introduction

Their main constituent is smaller than the thinnest hair. It is even smaller than an average body cell, and it is in the human body, to be more precise in the blood vessels that it does its job. In most cases, simply by being very flexible. If necessary, it transports and releases drugs or genes to various locations. It targets and binds to specific cells. It can even be used to destroy. Their beauty and fabulous capabilities will be further explored and exploited. Ultrasound contrast agents have come to stay!

1.1 Medical ultrasonography

Ultrasound contrast agents are used in a diagnostic imaging technique called medical ultrasonography. In this technique, ultrasound is applied to visualize tissue in the human body. It is a popular imaging technique due to a number of advantages, it is (1) a real-time modality (routinely 20-30 frames/s or more), (2) inexpensive, equipment is installed worldwide, (3) portable, equipment can be taken to bedside, ambulance or private practice office, (4) safe, e.g. no ionising radiation is necessary and (5) widely applicable, provided that air (lungs) and bone are avoided, all soft tissue can be imaged.

An ultrasound system generates ultrasound waves. Ultrasound waves used for medical applications have frequencies typically in the MHz range. These ultrasound waves travel through the human body and are partially reflected from the layers between different tissues. Specifically, the ultrasound is reflected anywhere there are density or compressibility changes in the tissue in the body. Part of these reflections (i.e. echoes) return to the ultrasound system, which receives and processes them into an image. In this way, the size and structure of the tissue can be visualized in echo images, as these images

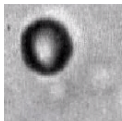

may also reveal possible pathologies or lesions in the tissue.

The ultrasonography technique is widely used in medicine. It is probably best known for its use in prenatal care, but the technique is applied in all sorts of medical specialisms. Echocardiography is for example the most used imaging technique in clinical cardiology (Galema et al., 2007). Despite the frequent use of ultrasound for cardiac diagnoses, echocardiography is technically challenging. The heart has to be imaged through a small acoustic window in between the ribs. The air in the lungs and the bone from the ribs should be avoided, because they are such great reflectors that no significant ultrasound signal can be expected from tissue that is lying behind.

In cardiac diagnoses, the regional wall motion, the ejection fraction and the presence of left ventricular thrombus are often examined, which requires delineation of the borders of the heart wall. This is feasible in most patients, but in obese patients or patients with lung disease, echo image quality is often insufficient. These patients comprise approximately 10-20% of routine echocardiographic examinations (Mulvagh et al., 2000). For these patients and others, ultrasound contrast agents have been developed (see Fig 1.1).

1.2 Ultrasound contrast agents

1.2.1 The first ultrasound contrast agent

In 1968, it was reported that the injection of agitated saline in the aortic root resulted in “a cloud of echoes between the undulating margins of the aortic root” (Gramiak and Shah, 1968). It appeared that gas ‘mini bubbles’ in the agitated saline acted as great contrast enhancers. Normally blood is a poor ultrasound scatterer and it remains dark in an echo image. The addition of gas bubbles to the blood pool by Gramiak and Shah (1968) greatly increased backscattered ultrasound, and resulted in an enhanced contrast between the aortic root wall and the blood. Nowadays, agitated saline is still used for the detection of right-to-left shunts in the heart (Soliman et al., 2007).

Before gas bubbles could be widely applied as ultrasound contrast agents, some improvements were necessary. Bubbles produced by agitation are both large and unstable, diffusing into solution in less than 10 seconds (Goldberg et al., 2001). Moreover, they are effectively removed by the lungs. Unless administered by intracoronary or aortic root injection, the bubbles are unable to traverse the pulmonary circulation to opacify the left cardiac chambers. To enter into the systemic circulation after an intravenous injection, the bubbles should have a size smaller than 10 μm diameter and should persist in solution for several minutes.

It was found empirically that a small admixture of the patient’s blood to the saline improved the stability and effectiveness of the agitated saline as a contrast agent (Blomley et al., 2007). Surfactant from the blood formed a coating around the gas core to prolong the lifetime of the microbubble. It was however not before the end of the 1980s that sufficient stable microbubbles were produced and marketed. A collection of ultrasound contrast agents that have been developed since is depicted in Fig 1.2.

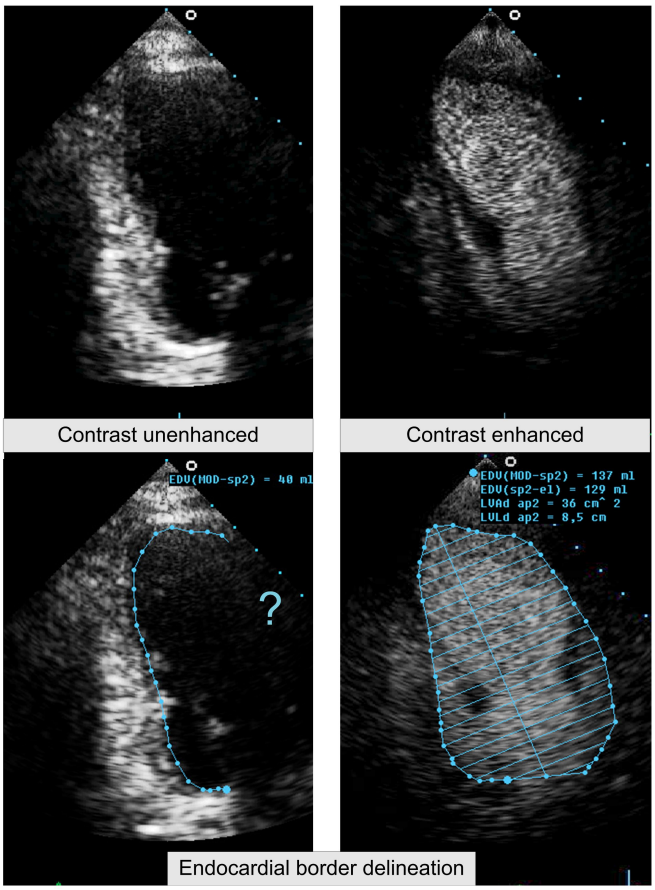

Figure 1.1: Heart left ventricle recorded from apical position. Bottom images show that contrast enhancement using an ultrasound contrast agent improves the detection of the heart wall border, which is useful to study the wall motion and the ejection fraction of the heart.
Images by courtesy of Dr. F.J. ten Cate of the Erasmus MC, Rotterdam, the Netherlands.

1.2.2 Modern ultrasound contrast agents

A gas bubble is unstable due to the surface tension between the gas core and the surrounding liquid, which tends the bubble to decrease in size. The addition of a coating reduces this surface tension and inhibits the diffusion of the gas. In 1994, Albunex (Molecular Biosystems, San Diego, CA, UCA) was the first commercially available contrast agent that was approved for human use in the USA. Albunex has a coating made of human

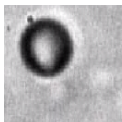

Figure 1.2: Ultrasound contrast agent vials

serum albumin. Soon the second contrast agent, Levovist (Bayer Schering Pharma AG, Berlin, Germany) came available in Europe and Japan in 1996. Levovist consists of galactose microcrystals whose surfaces provide absorption sites on which air bubbles form when suspended in water. A trace amount of palmitic acid further stabilizes Levovist microbubbles.

A new generation of contrast agents has been marketed since 1997. These newer contrast agents are stabilized by an albumin (e.g. Optison, GE Healthcare, Chalfont St Giles, UK), a polymer (e.g. Sonazoid, GE Healthcare, Chalfont St Giles, UK) or have a phospholipid coating (e.g. SonoVue, Bracco, Milan, Italy and Definity, Lantheus Medical Imaging, North Billerica, MA, USA). Moreover, they contain high-molecular-weight inert gases such as perfluorocarbon, which have a lower solubility and diffusivity compared to air in liquid (Goldberg et al., 2001). The perfluorocarbons are exhaled after several passes through the lungs. A summary of currently available contrast agents is given in Table 1.1.

1.2.3 Interaction of microbubbles with ultrasound waves

The contrast agent microbubbles owe their function to the high compressibilty of the gas core in comparison with surrounding liquid and tissue. This results in a high backscattering of ultrasound. Moreover, the microbubbles can act as resonant systems with resonant frequencies within the same range as medical ultrasound frequencies. A resonant microbubble has a strong increase in scattering cross-section compared to nonresonant microbubbles, e.g. a free gas microbubble has a resonant scattering cross-section that is an order of a thousand times greater than its geometrical cross-section (Pace et al., 1997).

The microbubble starts to vibrate in the ultrasound pressure field. At low amplitudes, these vibrations can be described with the theory for harmonic oscillators (Leighton, 1994). The compressibility of the gas core generates the stiffness of the oscillator and

Table 1.1: Currently available ultrasound contrast agents

Name	Manufacturer	Gas	Coating	Approved	Year	Available
Echovist	Bayer Schering Pharma AG	air	galactose	EU, Japan, Canada	1991	-
Albunex	Molecular Biosystems	air	human albumin	EU, USA, Canada	1994	-
Levovist	Bayer Schering Pharma AG	air	galactose, trace palmitin	worldwide[1]	1996	[2]
Optison	GE Healthcare AS	C3F8	human albumin	EU, USA	1997	EU, USA[3]
Definity	Lantheus Medical Imaging	C3F8	phospholipids	EU, USA, Canada	2001	USA, Canada
SonoVue	Bracco	SF6	phospholipids	EU, China, South Am.	2001	EU, China, South Am.
Imagent	Alliance Pharmaceutical Corp	C6F14	phospholipids	USA	2002	-
Sonazoid	Amersham Health	C4F10	lipids	Japan	2006	Japan

[1]: Approved in 65 countries, but not in the USA

[2]: Expected to finish in 2010

[3]: Temporary not available from 2006-2008

the vibrations of the microbubble are dampened due to the liquid viscosity, the radiation of ultrasound and thermal effects.

A coated microbubble is additionally dampened due to the coating. The coating thereby influences the microbubble's response to an ultrasound wave. For example, the resonant frequency of an encapsulated microbubble is generally higher than that of a free gas microbubble and the resonant peak is lower and broader (Khismatullin, 2004; van der Meer et al., 2007). To date, the impact of a coating on the behavior of gas microbubbles is however not fully understood, see also chapter 2.

1.3 Imaging strategies

The composition of the coating influences the stiffness of the microbubble and thus it influences the response of the microbubble to an ultrasound wave. This has led to different strategies to visualize the microbubbles in echo images. For the rigid shelled microbubbles such as Quantison (Andaris Ltd., Nottingham, UK) and BiSphere (Point Biomedical Corp., San Carlos, CA, USA), relatively high acoustic powers (mechanical indices (MI) > 1) are applied to deliberately disrupt these microbubbles and thereby release the gas (Frinking et al., 1999; Bouakaz et al., 2005). This results in strong microbubble-specific signals, which are easily differentiated from tissue signals.

The alternative approach is appropriate for microbubbles with more flexible coatings

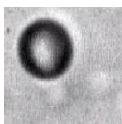

such as the phospholipid-coated contrast agents Definity, SonoVue, and BR14 (Bracco Research, Geneva, Switzerland). These microbubbles are able to oscillate both linearly and nonlinearly at relatively low acoustic pressures.

It is generally assumed that coated microbubbles oscillate linearly at acoustic pressures up to 50-100 kPa and nonlinearly above these acoustic pressures (Becher and Burns, 2000; Goldberg et al., 2001; Deng and Lizzi, 2002; Blomley et al., 2007; O'Brien, 2007). 'Linear oscillation' refers to a linear relationship between amplitude of oscillation and the acoustic pressure applied and it refers to symmetrical oscillations with equal compression and expansion amplitudes, resulting in responses containing the fundamental frequency only. For larger acoustic pressures, the oscillation amplitudes become asymetrical, because a microbubble resists compression more strongly than expansion. The coated microbubbles will rupture at very high acoustic pressures, e.g. above 1 MPa. In this thesis, it is shown that this general distinction between linear and nonlinear responses should be used with care.

The nonlinear responses of the microbubbles are exploited for imaging. As a result of the nonlinear oscillations of the microbubbles, the backscattered energy of the microbubbles contains higher harmonic, subharmonic or even ultraharmonic energy in addition to energy at the fundamental frequency of the ultrasound wave (Schrope et al., 1992; Shi and Forsberg, 2000; Chomas et al., 2002). Backscattered energy from tissue does not contain these harmonics or to a much lesser extent. These harmonics can therefore be used to differentiate the microbubbles from tissue to further enhance the contrast between bubbles (in the blood vessels) and surrounding tissue in the echo image.

Examples of imaging techniques that exploit these harmonics are second harmonic imaging (Schrope and Newhouse, 1993), pulse inversion imaging (Hope Simpson et al., 1999), power modulation imaging (Brock-Fisher et al., 1996), and combinations of these imaging techniques. These techniques have been implemented in commercial clinical ultrasound systems.

1.4 Safety of ultrasound contrast agents

Today, the clinical use of ultrasound contrast agents is widespread. In 2006, Blomley et al. (2007) estimated that 1 million of diagnostic examinations using approved ultrasound contrast agents had been performed, based on manufacturer sales data. Main et al. (2007) mentions that by the end of 2007, Definity has been administered to approximately 2 million patients since product approval in 2001. Figure 1.3 shows estimated sales figures for 2008.

Despite great promise and increasing use worldwide, the ultrasound contrast agents are mainly used by specialist centers and still account for a small proportion of diagnostic ultrasound examinations (Blomley et al., 2007). This is probably caused by the fact that the use of ultrasound contrast agents is still relatively new and their safety is with or without good reason not unambiguous, which is briefly discussed here.

Like all other contrast agents used in medicine, adverse events can occur with ultra-

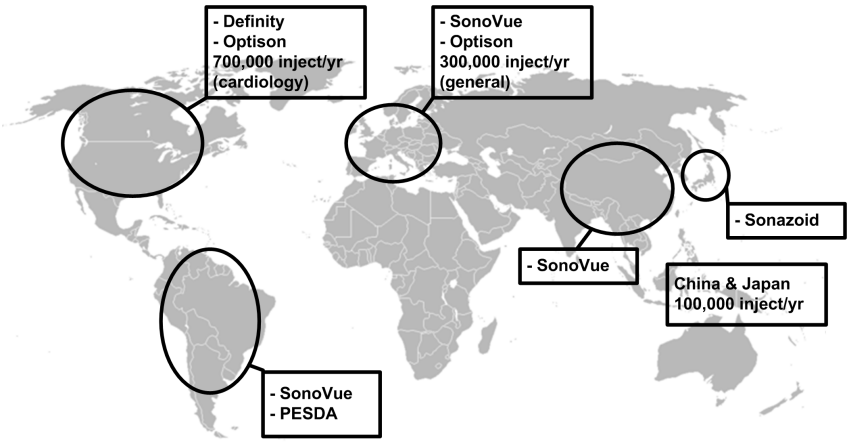

Figure 1.3: Estimated sales figures of ultrasound contrast agents in 2008.

sound contrast agents (Dijkmans et al., 2005). These adverse events are mainly allergic reactions (van Camp et al., 2007), which are in general nonserious (Blomley et al., 2007), but sometimes these reactions can be very serious (anaphylactoid reactions) (van Camp et al., 2007).

In cardiac applications, the reporting of some adverse events (not necessarily allergic) after the use of ultrasound contrast agents has led to some restrictions imposed by the European Medicines Agency (EMEA) and the U.S. Food and Drug Administration (FDA).

A post-marketing analysis of 157,838 studies of SonoVue brought to light 19 cases of severe, non-fatal (0.012%) and three cases of fatal adverse events (0.002%) after the use of this contrast agent (EMEA, 2004a). Based on these rates, EMEA recommended not to use SonoVue in cardiology in May 2004. These recommendations were partly reversed in November 2004, but there are still some restrictions such as the presence of resuscitation equipment and to keep the patient under medical supervision for at least 30 minutes following the infusion of SonoVue (EMEA, 2004b).

In October 2007, the FDA announced a 'black box' warning for perflutren-containing ultrasound contrast agents such as Definity, contraindicating their use in patients with serious cardiac illnesses (FDA, 2008). These warnings followed post-marketing reports of 4 patient deaths. In July 2008, several contraindications were removed by the FDA, but similar restrictions as imposed by the EMEA on the use of ultrasound contrast agents persist (FDA, 2008).

The findings by EMEA and FDA are opposed by many cardiologists, who have debated that a causal relationship between these fatal adverse events and the use of an ultrasound contrast agent is uncertain (Main et al., 2007; Blomley et al., 2007). It is debated that even if all of the reported events occurred as a direct result of contrast administra-

tion, this would still result in a very low risk comparable with the use of other contrast agents or other investigations in cardiology such as exercise treadmill testing (Dijkmans et al., 2005; Blomley et al., 2007; Main et al., 2007). Finally, it is mentioned here that recently a large study on 18,671 patient events has shown no increased mortality risk associated with Definity-enhanced echocardiography examinations in hospitalized patients (Kusnetzky et al., 2008).

Since safety issues and costs determine the clinicial future of ultrasound contrast agents (Galema et al., 2007), the restrictions by the EMEA and FDA have great consequences on the use of ultrasound contrast agents. In some cardiac applications, their use is simply forbidden. In all other cardiac applications, their use has become more expensive.

1.5 Other applications of ultrasound contrast agents

The vast majority of contrast examinations worldwide is still used for endocardial border delineation (van Camp et al., 2007) (Fig 1.1). The ultrasound contrast agents are also used to increase the intensity of Doppler signals for the detection of blood flow, which is useful in both cardiology and radiology applications. In radiology, ultrasound contrast agents are used to examine blood flow in liver and kidneys, but also to visualize the vasculature of malignant tumors.

Contrast agent microbubbles have originally been developed for diagnostic purposes. Molecular imaging and therapeutic application of coated microbubbles in combination with ultrasound are more recent developments that receive a lot of attention. Molecular imaging is a new discipline that unites molecular biology and *in vivo* imaging. It enables the visualisation of the cellular function and the follow-up of the molecular process in living organisms without perturbing them. Different modalities can be used for molecular imaging such as MRI and SPECT, but also contrast-enhanced ultrasound (Liang and Blomley, 2003).

In therapeutic applications, the microbubbles are used for treatment of diseases. Oscillating microbubbles can be used to trigger the endothelial cell membranes or tight junctions between these cells to open for bioactive materials that normally cannot enter these cells and the tissue that is lying behind (van Wamel et al., 2006; Kooiman et al., 2006). This opening is transient (van Wamel et al., 2006). Ultrasound can be applied locally and therefore these microbubbles can be used to locally enhance the delivery of drugs or genes to the body (Unger et al., 2004). It has also been reported that oscillating microbubbles can be used to reversibly open the bloodbrain barrier for the local delivery of drugs in the brain (Unger et al., 2004; Dijkmans et al., 2004).

In addition the microbubbles can be applied as a drug delivery system. The microbubbles are excellent candidates to carry bioactive compounds. Kooiman et al. (2008) have recently built such a drug delivery system, consisting of polymeric microbubbles that are able to transport lipophilic drugs. Moreover, the microbubbles could be composed such that they carry ligands on their surface. These ligands bind to specific sites in the body,

such as the receptors of tumor cells or receptors of cells that are part of an atherosclerotic plaque (Klibanov, 2005). When insonified, they visualize these sites and in addition could be triggered to locally release the drugs or genes they were carrying.

A final example of other coated microbubble applications is to use these microbubbles to induce vascular injury and cell damage. At high acoustic pressures, the microbubbles are able to oscillate with great amplitudes. A fast collapsing microbubble generates a flow, which could damage body cells. This damaging capacity could be exploited to treat cancer by destroying blood vessels in malignant tumors (Skyba et al., 1998).

1.6 Rationale and scope

The expansion of applications for ultrasound contrast agents could not have been achieved without fundamental research to the behavior of bubbles in an ultrasound field. Whereas the behavior of free gas microbubbles at low and moderate amplitudes is generally known, the impact of an additional coating on the behavior of insonified bubbles has still not been fully elucidated. The aim of this thesis is to gain fundamental knowledge on the behavior of coated microbubbles in an ultrasound field. This knowledge is useful to further exploit the capabilities of ultrasound contrast agents.

To gain this knowledge, we study the vibrations of individual microbubbles in a major part of this thesis. Individual microbubbles are best studied using a high-speed camera. Commercially available high-speed cameras are not able to catch bubble vibrations with frequencies in the MHz range. It is therefore that the labs of Biomedical Engineering (Erasmus MC) and Physics of Fluids (University of Twente) decided to build together their own high-speed camera system. This has resulted in the Brandaris 128, which is capable of recording 128 frames at frame rates up to 25 million frames per second (Chin et al., 2003) (Fig 1.4). One recording consists of six movies of 128 frames with an interval time of 80 ms between the movies. The camera system can also be programmed to record twelve movies of 64 frames, 24 movies of 32 frames etc.

In this thesis, we used the Brandaris 128 to investigate the responses of phospholipid-coated microbubbles. Phospholipid-coated contrast agents represent a significant part of the contrast agents currently used, see Table 1.1 and Fig 1.3. A distinct feature of these contrast agents is that they contain microbubbles with a coating that is both flexible and stable, which allows microbubble vibrations at a broad range of acoustic pressures and in this way these contrast agents can be applied in imaging techniques at both low and moderate acoustic pressures.

This research started by posing the question what happens when an acoustic pressure field hits these phospholipid-coated microbubbles. Does a coated microbubble always respond to an imposed force or is it necessary that this force exceeds a certain value before the microbubble starts to vibrate?

Based on current knowledge, we expect that the microbubble starts to vibrate as soon as the acoustic pressure field arrives at the microbubble. This is based on the general assumption that coated microbubbles oscillate linearly at acoustic pressures below 50-

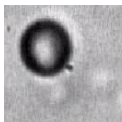

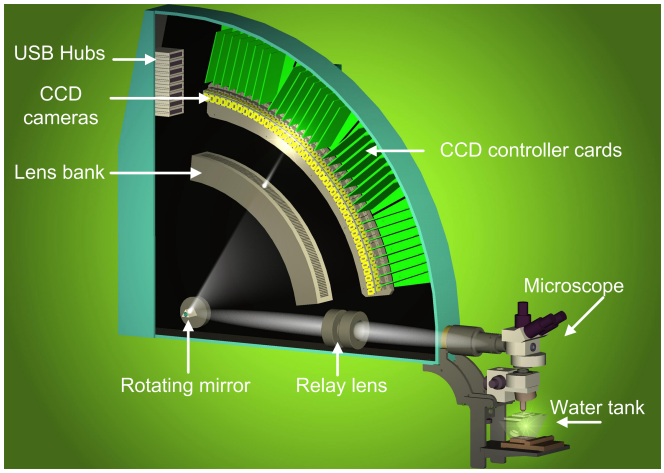

Figure 1.4: Drawing of the Brandaris 128 high-speed camera system. The microscope and relay lenses project the image of the microbubble on a fast rotating mirror. The image is reflected at an angle by the mirror and sweeps along 128 CCD cameras. Increasing the speed of the rotating mirror leads to frame rates up to 25 million frames per second.

100 kPa as mentioned in section 1.3. This assumption implies that there is a linear relationship between the amplitudes of the bubble oscillation and the acoustic pressure field, which means that any acoustic pressure applied, even if it is just above 0 Pa, leads to a vibration of the bubble. When we consider a more familiar situation, this linear relationship does not seem very plausible.

Imagine a big box on the ground (Fig 1.5). When we try to move this box, we first have to overcome the static friction between the box and the ground before the kinetic friction takes over. An initial force is necessary to overcome this static friction and before the force applied exceeds this initial value, the box does not start to move.

The onset of bubble vibration may be comparable to the onset of box motion. The microbubble coating adds friction to the bubble system, which may act similar to the static friction of the box. This would mean that the microbubble does not respond to any acoustic pressure applied.

1.7 Outline

The concept of a model describing the bubble dynamics is explored, which is followed by an overview of current available theoretical descriptions of coated microbubbles in chapter 2. Chapter 3 presents a model for phospholipid-coated microbubbles. This model is able to predict compression-only behavior. This behavior was observed in a large study with the high-speed camera system that is presented in chapter 4. The onset of coated

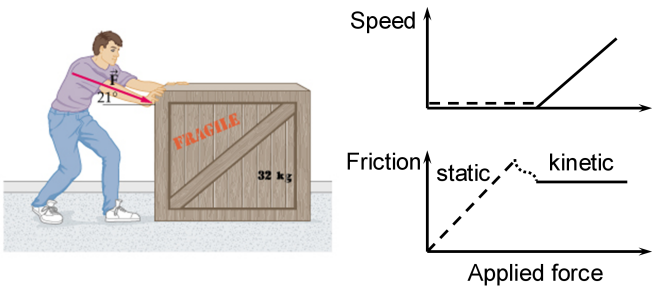

Figure 1.5: The onset of box motion.

bubble vibration was investigated in chapter 5. This resulted in the observation of threshold behavior. In chapter 6, pressure-dependent acoustic behavior was measured, which could be explained by the optically observed threshold behavior. We utilized pressure-dependent scattering for imaging in a clinical setting in chapter 7 and 8. Furthermore, the influence of compression-only behavior on the radial modulation imaging technique was studied in chapter 9. Finally, it was tested in chapter 10, if modifications to the composition of the phoshpolipid-coatings would lead to an enhancement of compression-only and threshold behavior.

2

Ultrasound contrast agent models

2.1 Introduction

Models are vehicles for learning about the world. Significant parts of scientific investigation are carried out on models rather than on reality itself, because by studying a model, features and facts can be discovered of the system that the model describes. Models allow for quantitative reasoning to observations of the world, in hope of seeing aspects that may have escaped the notice of others (Silvert, 2000). This cognitive function of models has been widely acknowledged in the literature, and some even suggest that models give rise to a new style of reasoning, so-called 'model based reasoning' (Frigg and Hartmann, 2006).

Models can perform two fundamentally different representational functions. On the one hand a model can be a representation of a selected part of the world. Such models are either phenomenological models or data models. On the other hand, a model can represent a theory in the sense that it interprets the laws and axioms of that theory (Frigg and Hartmann, 2006). These functions are not mutually exclusive as scientific models can be representations in both senses at the same time. A model of a coated microbubble is a good example of such a combination of representations.

The contrast agent microbubble is described as a phenomenological model when it is represented as a monolayer of lipids surrounded by liquid. A phenomenological model typically refers only to some aspects of the phenomenon in question, and two models of the same phenomenon may be different due to conceptual or aesthetic differences by the modelers and decisions made during the modeling process (Frigg and Hartmann, 2006). Other examples of these models are the Bohr model of an atom and the double helix

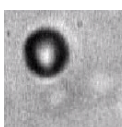

model of DNA.

Within the group of phenomenological models, there is also the data model. The data model is a corrected, rectified, regimented, and in many instances idealized version of the data we gain from immediate observations, the so-called raw data (Frigg and Hartmann, 2006). Characteristically, one first eliminates errors (*e.g.* removes points from the data that are due to faulty observation) and then present the data in a 'neat' way, for instance by drawing a smooth curve through a set of points. Data models play a crucial role in confirming theories because it is the data model and not the often messy and complex raw data that we compare to a theoretical prediction.

The contrast agent microbubble can also be represented by a theoretical model. This concept in modern logic implies that a model is a structure that makes all sentences of a theory true, where a theory is taken to be a set of sentences in a formal language. The structure is a 'model' in the sense that it is what the theory represents (Frigg and Hartmann, 2006). This concept is particularly pertinent in physics, where general laws, such as Newton's Second Law, lie at the heart of a theory. These laws are applied to a particular system, *e.g.* the coated-bubble, by choosing a force balance, making assumptions about the type of gas in the bubble etc. The resulting model is then an interpretation (or realization) of the general law.

The purpose of this chapter is to explore the concept of a 'coated-microbubble model' and underlying assumptions. We start with a detailed examination of the governing equation of the motion of a bubble, the Rayleigh-Plesset equation. Next, the benefits of adding a coating to a free microbubble are discussed and finally an overview of publications considering a variety of coated-bubble models is given.

2.2 The Rayleigh-Plesset equation

There are currently two main classes of theoretical descriptions for ultrasound contrast agents (Leighton and Dumbrell, 2004). The first class involves acoustic scatter cross-sections (see for example Medwin (1977)). This class has the advantage that it is easily related to measurements and deals with populations in which contrast agents usually occur. It has however also an empirical basis and cannot be related to single-bubble dynamics. The second class of contrast agent models has a more fundamental physical basis and consists of models describing single-bubble dynamics. Existing models for free gas single bubbles are adapted to incorporate the effects of the contrast agent microbubble coating. In future, a third class may develop which is describing the ultrasound contrast agent using finite element modeling (*e.g.* Pauzin et al. (2007)).

In this thesis, it is focused on the second class of bubble models, which finds its history in the research to inertial cavitation. Inertial cavitation intrigued many when it became apparent that during the collapse of a gas cavity significant amounts of energy are released, for example high enough to seriously damage screw-propellers of ships. Lord Rayleigh pioneered the research to the motion of bubbles by his treatment of the collapse of an empty cavity in a liquid in 1917 (Rayleigh, 1917). This cavity remained

spherical at all times and was located in an incompressible liquid. The main step from cavitation collapses towards bubble dynamics was the introduction of a variable external driving pressure and of the influence of surface tension by Plesset (1949). Plesset described the dynamics of vapour-filled bubbles and Noltingk and Neppiras (1950) did the same for gas-filled bubbles. The effect of viscosity on the equation of motion of a bubble in an incompressible liquid was considered by Poritsky. These contributions led together to the Rayleigh-Plesset-Noltingk-Neppiras-Poritsky (RPNNP) equation (Lauterborn, 1976), nowadays more commonly called 'the Rayleigh-Plesset equation'.

The archetype of most bubble models is easily derived, see for example Leighton (1994). It starts with the pressure inside a bubble p_i that consists of a gas pressure p_g and a liquid vapour pressure p_v:

$$p_i = p_g + p_v \tag{2.1}$$

The pressure within a bubble at rest is greater than the pressure immediately outside the bubble p_l as a result of the surface tension forces $p_\sigma = \frac{2\sigma}{R_0}$, σ is the surface tension.

$$p_i = p_l + \frac{2\sigma}{R_0} \tag{2.2}$$

where R_0 is the bubble resting radius. It is assumed that the pressure in the liquid changes in a quasi-static manner such that outside the bubble it has value p_l. Because the change is quasi-static, the pressure throughout the liquid must be spatially uniform and so also equal to p_l. At equilibrium, the liquid pressure is equal to the ambient pressure p_0. The gas pressure at equilibrium is

$$p_{g,e} = p_0 + \frac{2\sigma}{R_0} - p_v \tag{2.3}$$

The pressure in the gas can be calculated choosing an ideal polytropic gas law $p_g \propto R^{-3\kappa}$, with κ is the polytropic gas exponent. The polytropic exponent is 1 when the bubble behaves isothermally and equal to the ratio of specific heats for bubbles that behave adiabatically. Whether an isothermal or adiabatic law must be applied depends on the ratio between the time available for the heat diffusion into the liquid and the length that needs to be traveled in the gas, which can be determined using the Péclet number, $Pe = \frac{R_0^2\omega}{D_{th}}$ with D_{th} is the thermal diffusivity and ω the frequency of oscillation (Prosperetti, 1991; Khismatullin and Nadim, 2002). When $Pe >> 1$ the bubble tends to the adiabatic limit. Combining Eq (2.3) with the polytropic law results in

$$p_g = p_{g,e}\left(\frac{R_0}{R}\right)^{3\kappa} = \left(p_0 + \frac{2\sigma}{R_0} - p_v\right)\left(\frac{R_0}{R}\right)^{3\kappa} \tag{2.4}$$

The pressure at the bubble wall is derived by combining Eq (2.1, 2.2, and 2.4)

$$p_l = \left(p_0 + \frac{2\sigma}{R_0} - p_v\right)\left(\frac{R_0}{R}\right)^{3\kappa} + p_v - \frac{2\sigma}{R} \tag{2.5}$$

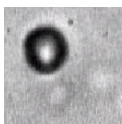

Next step is to relate the dynamical motion of the bubble to an implied pressure. At a time $t < 0$, the hydrostatic pressure is p_0 and the bubble is at rest. At time $t > 0$, an acoustic driving pressure $P(t)$ is superimposed on p_0, so that the liquid pressure at a point remote from the bubble is $p_\infty = p_0 + P(t)$. Consequently the bubble radius will change to some new value $R(t)$. During this process, the liquid will acquire a kinetic energy

$$E_k = \frac{1}{2}\rho_l \int_R^\infty \dot{r}^2 4\pi r^2 dr \tag{2.6}$$

where $\dot{r}$ is the time derivative of r. It is assumed that the liquid is incompressibile and thus the density ρ_l remains constant. Then conservation of mass says that mass flow through a sphere with radius r equals the mass flow through the radius of the bubble R, which leads to the following relation

$$\frac{\dot{r}}{\dot{R}} = \frac{R^2}{r^2} \tag{2.7}$$

Using Eq (2.7), Eq (2.6) is integrated, which results in $2\pi\rho_l \dot{R}^2 R^3$. The kinetic energy generated by the moving liquid is equated to the difference in work done remote from the bubble by p_∞ and the work done by the pressure p_l in the liquid immediately outside the bubble wall, which gives

$$\int_{R_0}^{R} (p_l - p_\infty) 4\pi R^2 dR = 2\pi\rho_l \dot{R}^2 R^3 \tag{2.8}$$

Differentiating with respect to R results in the equation of motion for a bubble in its most basal form. It was already derived in 1879 by Besant (Stride, 2008).

$$\frac{(p_l - p_\infty)}{\rho_l} = \frac{3}{2}\dot{R}^2 + R\ddot{R} \tag{2.9}$$

where $\ddot{R}$ is the second derivative of R with respect to time.

The liquid pressure calculated with Eq (2.5) is substitued in Eq (2.9). The force acting on the bubble is included in Eq (2.9) by expanding p_∞ to $p_0 + P(t)$. The resulting equation describes the response of a spherical bubble to a time-varying pressure field in an incompressible liquid

$$\rho_l \left(R\ddot{R} + \frac{3}{2}\dot{R}^2 \right) = \left(p_0 + \frac{2\sigma}{R_0} - p_v \right) \left(\frac{R_0}{R} \right)^{3\kappa} + p_v - \frac{2\sigma}{R} - p_0 - P(t) \tag{2.10}$$

This initial treatment can be improved to incorporate the effects of viscosity. Starting from the Navier-Stokes equations assuming liquid incompressibility and including viscous effects in the boundary conditions leads to the same result as Eq (2.10) with the viscous damping term added, $-\frac{4\mu\dot{R}}{R}$ (μ is the dynamic viscosity) (Leighton, 1994). The resulting equation is called the 'Rayleigh-Plesset equation':

$$\rho_l \left(R\ddot{R} + \frac{3}{2}\dot{R}^2 \right) = \left(p_0 + \frac{2\sigma}{R_0} - p_v \right) \left(\frac{R_0}{R} \right)^{3\kappa} + p_v - \frac{2\sigma}{R} - \frac{4\mu\dot{R}}{R} - p_0 - P(t) \tag{2.11}$$

The Rayleigh-Plesset equation is nonlinear, as one would expect from a system where, except at low amplitude, the expansion cannot be symmetric with the compression. At low amplitudes this equation gives the direct small-amplitude approximation of the resonant frequency of a free gas bubble and therefore shows that in the small amplitude limit, the bubble can tend to behave as a forced linear oscillator (Leighton, 1994).

2.3 Other equations of motion

Assuming liquid incompressibility has the result that the speed of sound in the liquid becomes infinite. When the bubble wall has a speed much lower than the speed of sound $\dot{R} << c$, this is a valid assumption, but at large bubble oscillations, an extended version of the Rayleigh-Plesset equation should be used, such as formulations from the Herring-Keller/Keller-Miksis or Gilmore-Akulichev families (Vokurka, 1986). These equations incorporate radiation damping. A practically good applicable, but also a robust and accurate equation (Hilgenfeldt et al., 1996) for the description of motion of a free gas bubble appeared to be the equation defined by Keller and Miksis (1980):

$$\begin{aligned} \rho_l \left(R\ddot{R} + \frac{3}{2}\dot{R}^2 \right) &= \left(p_0 + \frac{2\sigma}{R} \right) \left(\frac{R_0}{R} \right)^{3\kappa} \left(1 - \frac{3\kappa}{c}\dot{R} \right) \\ &\quad - \frac{2\sigma}{R} - \frac{4\mu_l \dot{R}}{R} - p_0 - P(t) \end{aligned} \tag{2.12}$$

2.4 Damping in the equation of motion

Damping tends to reduce the amplitude of oscillations of the bubble. Energy losses by damping occur through three mechanisms (Leighton, 1994)

Radiation damping	Energy is radiated away from the bubble as acoustic waves.
Viscous damping	Work is done against viscous forces.
Thermal damping	Energy is lost through thermal conduction between the gas and the surrounding liquid.

Based on the work of Prosperetti (1977), the contributions of the different damping terms for small-amplitude forced oscillations of a free gas bubble were derived in Leighton (Fig 4.39 Leighton (1994)). Viscous damping is independent of insonation frequency in a Newtonian fluid. It is the dominant source of damping for microbubbles with a resting diameter of 1 μm, but its influence diminishes as the size of the bubble becomes larger. General trends are that radiation damping is negligible at low insonation frequencies and thermal damping at high insonation frequencies. The transition from low to high frequency highly depends on bubble size and is in the order of 1 MHz for bubbles with resting sizes of 10 μm diameter and 10 MHz for bubbles of 1 μm diameter.

Thermal damping is of particular interest, in that none of the above mentioned formulations in themselves include any net thermal losses. Thermal damping for the time-

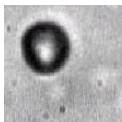

dependent nonlinear oscillations of bubbles requires rigorous treatments that are not easily incorporated in the bubble models (*e.g.* Nigmatulin et al. (1981); Prosperetti (1991); Preston et al. (2002)). This is therefore one of the reasons that thermal damping is often neglected. Another possibility is to replace it by a 'thermal viscosity' (*e.g.* van der Meer et al. (2007)).

Also in the derivation by Prosperetti (1977) damping due to heat transfer was calculated using an effective liquid viscosity and a polytropic approximation to account for the expansion and compression of the gas bubble interior. The stiffness of the bubble is mainly determined by the polytropic characteristics of the gas. When a value for the polytropic index between the isothermal and adiabatic case is taken, the stiffness of the bubble may be adjusted to account for heat flow across the bubble wall. Then its value must vary during the oscillatory cycle, otherwise there are no thermal losses (Leighton and Dumbrell, 2004).

Devin (1959) calculated the viscous, acoustic, and thermal damping constants of bubbles oscillating at small amplitude at resonance (see also Medwin (1977)). These calculations also give an expression for the polytropic exponent κ. Eller (1950) extended this work to give expressions for the damping constants off resonance. The derivations for these damping terms have an empirical basis as is referred to at the beginning of section 2.2 and are valid for limited conditions.

A thermal damping derived for small smplitudes is *e.g.* not valid in the field of sonoluminescence (Brenner et al., 2002). Sonoluminescence happens when a gas bubble collapses so strongly that the energy focusing at collapse leads to light emission. Tögel and Lohse (2003) incorporated a more physical model for thermal damping in the Keller-Miksis equation (Eq (2.12)) to describe single bubble sonoluminescence. For other examples it is referred to the review by Brenner et al. (2002).

2.5 The addition of a coating

Equation (2.2) shows that there is an excess pressure within the bubble, generated to balance p_σ, which tends to raise the partial pressure of the gas within the bubble to greater than the partial pressure of the gas that is dissolved in the surrounding liquid. Therefore, all else being equal, a bubble will tend to dissolve. Using the equation by **?** and the parameter values given by **?**, it is calculated that in air saturated water, an air bubble with a diameter of 5 μm disappears in approximately 6.7 s and an air bubble with a diameter of 2.5μm disappears in approximately 95 ms at room temperature and ambient pressure.

The lifespan of free gas microbubbles is therefore too short for them to be of practicle use as a ultrasound contrast agent in the human body. It takes at least 12 s for a contrast agent to pass from a peripheral vein (*i.e.* the site of injection) to the end-organ (Goldberg et al., 2001). Consequently, the gas bubbles have to be stabilized in order to achieve sufficient long persistence as well as to survive the pressure changes in the heart.

Most ultrasound contrast agents are stabilized against dissolution by the presence

of additional materials at the gas-liquid interface, such as phospholipids, albumin and polymers and by the use of low soluble filling gases such as sulfur hexafluoride and perfluorobutane (Table 1.1). In case of an elastic solid shell (composed from albumin or polymers), the bubble's stability is enhanced by supporting a strain to counter the effect of a surface tension.

Surfactants such as phospholipids promote stability by greatly reducing the surface tension at the interface. The higher chemical potential of a gas inside the bubble will result in the tendency of the gas to diffuse through the surface layer of the microbubble into the suspending medium. If the molecules of the surface layer are closely packed, the encapsulated gas encounters resistance to diffusion into the acqueous environment, which also enhances the bubble's stability.

2.6 Ultrasound contrast agent models

In the following sections an overview of existing models on ultrasound contrast agent microbubbles is given. A selection was made. The purpose is to present frequently cited models and to capture trends in coated bubble modeling over the past years. For each model, the governing equation of motion for the bubble wall and the constitutive law for the coating material is given. Furthermore, each summary contains the source for the coating parameter values and the main implications of the model. For a quick overview, the reader is referred to section 2.7 and Table 2.1 at the end of this chapter.

2.6.1 De Jong (1994)

In 1994, De Jong et al. laid the foundation for ultrasound contrast agent modeling by their theoretical description of the vibration of an encapsulated microbubble. The description is an extension to the equation of motion of a gas bubble in water and models the air-filled, albumin-coated contrast agent Albunex (Molecular Biosystems Inc., San Diego, USA). The backbone of the model is the Rayleigh-Plesset equation defined by Eatock et al. (1985). In this equation, the viscosity of surrounding liquid is not a separate term as in Eq (2.11), but it is part of a total damping term δ_t. Terms for damping by the liquid viscosity δ_{vis}, thermal δ_{th} and radiation damping δ_{rad} were derived under linear conditions and lumped together in one damping parameter (Medwin, 1977).

The influence of the encapsulation was captured in two parameters, the shell elasticity S_p and the shell friction S_f, which were added to the equation of motion. Their values were determined under linear conditions for Albunex microbubbles by fitting calculated acoustic transmission and scattering values to measurements (de Jong and Hoff, 1993).

$$\begin{aligned}\rho_l\left(R\ddot{R}+\frac{3}{2}\dot{R}^2\right) &= \left(p_0+\frac{2\sigma}{R_0}-p_v\right)\left(\frac{R_0}{R}\right)^{3\kappa}+p_v-\frac{2\sigma}{R}\\ &\quad -2S_p\left(\frac{1}{R_0}-\frac{1}{R}\right)-\delta_t\omega\rho_l R\dot{R}-p_0-P(t) \quad (2.13)\end{aligned}$$

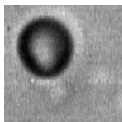

where $\delta_t = \delta_{rad} + \delta_{vis} + \delta_{th} + \delta_{fr}$ and $\delta_{fr} = S_f/(4\pi R^3 \rho_l \omega)$.

2.6.2 Church (1995)

The model by Church (1995) is essentially not very different from the model by de Jong et al. (1994). This model was also dedicated to Albunex and describes the encapsulation as an elastic solid. It has however a more rigorous theoretical basis.

Church used a generalized Rayleigh-Plesset model that accounted for the shell thickness and viscoelastic properties. The Kelvin-Voigt constitutive law was applied, which is essentially Hooke's law for an incompressible material and predicts the stresses developing on the shell for small displacements. The bubble was surrounded by incompressible, Newtonian liquid. Analytical solutions to the Eq (2.14) are presented in the paper including the fundamental and second harmonic response.

$$\begin{aligned}\rho_s R_1 \ddot{R}_1 \left[1 + \left(\frac{\rho_l - \rho_s}{\rho_s}\right)\frac{R_1}{R_2}\right] + \quad \rho_s \dot{R}_1^2 \left[\frac{3}{2} + \left(\frac{\rho_l-\rho_s}{\rho_s}\right)\left(\frac{4R_2^3 - R_1^3}{2R_2^3}\right)\frac{R_1}{R_2}\right] = \\ p_0 \left(\frac{R_{01}}{R_1}\right)^{3\kappa} - \frac{2\sigma_1}{R_1} - \frac{2\sigma_2}{R_2} - p_0 - P(t) \\ - 4\frac{\dot{R}_1}{R_1}\left(\frac{V_s\mu_s + R_1^3\mu_l}{R_2^3}\right) \\ - 4\frac{V_s G_s}{R_2^3}\left(1 - \frac{R_{e,1}}{R_1}\right) \qquad (2.14)\end{aligned}$$

The subscripts 1 and 2 refer to the inner and outer radius of the microbubble's shell and the subscripts s and l refer to shell and liquid. $V_s = R_{02}^3 - R_{01}^2$. G_s is the elastic modulus and μ_s is the shear viscosity of the shell. $R_{e,1}$ is the unstrained equilibrium position of the inner radius, which is in general not equal to R_{01}. For the full equation of $R_{e,1}$, see Church (1995).

Thermal and acoustic damping were not part of the derivation of the equation of motion (2.14). These extra damping terms were derived based on the work of Devin (1959); Eller (1950) and added to the linearized expressions for extinction and scattering cross sections. Shell parameters for Albunex microbubbles were based on the study by de Jong and Hoff (1993).

An important outcome is the finding that a coated microbubble is much stiffer than a free gas microbubble and resonates at a much higher frequency than free bubbles of the same size. The damping provided by the viscosity of the shell dominates thermal effects for bubble radii less than approximately 10 μm. Furthermore, it was indicated that in the weak nonlinear regime, the fundamental response of the microbubble is proportional to the acoustic pressure applied whereas the second harmonic response follows the square of the driving pressure.

2.6.3 Hoff (2000)

Hoff et al. (2000) applied the model by Church (1995) in the limit of small shell thickness in comparison with the radius. In this study, the viscoelastic shell parameters of

Nycomed (Nycomed Amersham, Oslo, Norway) were determined. Nycomed is composed of polymer coated, air-filled microbubbles. The shear modulus G_s and viscosity μ_s of a polymeric material are in general frequency dependent, but it is assumed that they are constant for the frequencies considered (1-8 MHz). The following equation of motion was derived,

$$\begin{aligned}\rho_l\left(R\ddot{R}+\frac{3}{2}\dot{R}^2\right) &= p_0\left(\left(\frac{R_0}{R}\right)^{3\kappa}-1\right)-P(t)\\ &\quad -4\mu_l\frac{\dot{R}}{R}-12\mu_s\frac{d_{s,0}R_0^2}{R^3}\frac{\dot{R}}{R}\\ &\quad -12G_s\frac{d_{s,0}R_0^2}{R^3}\left(1-\frac{R_0}{R}\right)\end{aligned} \tag{2.15}$$

where $d_{s,0}$ is the thickness of the shell at the resting state.

Calculations from this model are compared with acoustic attenuation measurements in the linear range. In the linearized expressions for the extinction and scattering cross-section, thermal and acoustic damping terms were added, as was also suggested by Church (1995). Based on these linearized expressions and measurements, it was concluded that the shell strongly alters the acoustic behavior of the bubbles. The stiffness and viscosity of the particles are mainly determined by the shell and not by the air inside. The resonance frequency of a coated microbubble is greater than the resonance frequency of an equally sized free gas microbubble.

2.6.4 Morgan (2000)

The study by Morgan et al. (2000) is innovative in several respects. Previous studies treated relatively hard-shelled microbubbles. Morgan et al. investigated a phospholipid-coated contrast agent, MP1950 (Mallinckrodt, Inc., St. Louis, MO, USA), which has a more flexible coating allowing for larger oscillation amplitudes compared to hard-shelled microbubbles. Furthermore, they used streak images of vibrating single microbubbles to determine the values of the shell parameters. The values of the shell parameters were obtained by fitting the optical radius-time curves to the theoretical predictions.

The bubble model is based on the modified Herring equation. This equation was adapted from Vokurka (1986) to include the coating. Coating effects are represented by two additional terms. The first shell term incorporates the elasticity of the shell (χ) and is based on a study by Glazman (1983). It is commented that in a subsequent study, Marmottant et al. (2005) showed that this elasticity term leads to an effective surface tension that decreases when the microbubble is inflated, which is not realistic. The second shell term is a damping term because of the viscosity of the shell (μ_s) and is similar to

the derivation of terms by Church (1989). The equation is given by:

$$\begin{aligned}\rho_l\left(R\ddot{R}+\frac{3}{2}\dot{R}^2\right) &= \left(p_0+\frac{2\sigma}{R_0}+\frac{2\chi}{R_0}\right)\left(\frac{R_0}{R}\right)^{3\kappa}\left(1-\frac{3\kappa}{c}\dot{R}\right)\\ &\quad -\frac{4\mu_l\dot{R}}{R}-\frac{2\sigma}{R}\left(1-\frac{1}{c}\dot{R}\right)-\frac{2\chi}{R}\left(\frac{R_0}{R}\right)^2\left(1-\frac{3}{c}\dot{R}\right)\\ &\quad -12\mu_s d_s\frac{\dot{R}}{R(R-d_s)}-p_0-P(t)\end{aligned} \tag{2.16}$$

The results indicated that the elasticity parameter χ had a far smaller effect than the viscosity parameter μ_s on the bubble's response. They could set the elasticity term to zero in many examples without effect. Second, they found that the elasticity parameter did not change with bubble radius in contrast with the viscosity parameters that appeared to increase with bubble radius in a linear manner.

2.6.5 Khismatullin (2002)

An effort to a more rigorous theoretical description of radial motion of microbubbles in blood was made by Khismatullin and Nadim (2002). They used a Kelvin-Voigt model for the encapsulation, similar to Church (1995), but instead of a Newtonian liquid surrounding the microbubble, they considered the outside liquid to be slightly compressible and viscoelastic and applied a 4-constant Oldroyd model. A Maxwell model is a more simple description of a viscoelastic material, but it depends on the frame of reference and is not symmetrical in three dimensions, which is the case for an Oldroyd model. After a lengthy derivation (for the resulting equation it is referred to Khismatullin and Nadim (2002)), they arrive at examinations in the limit of small-amplitude oscillations, hence they are restricted to first and second harmonic responses.

This model was not made with a specific contrast agent in mind. Shell parameters were obtained from literature, *e.g.* de Jong et al. (1994). It was concluded that the total damping of the radial oscillations is mainly determined by the shell viscosity and that in the case of a viscoelastic liquid, the contribution of liquid viscosity to the total damping coefficient is below that for a Newtonian liquid. The resonant peaks in the scattering cross-section curves are very sensitive to the shell parameters but not to the liquid parameters.

2.6.6 Chatterjee (2003)

The model by Chatterjee and Sarkar (2003) considers thin-shelled agents, specifically the dynamics of Optison (GE Healthcare, Chalfont St Giles, UK) are simulated. Optison is a contrast agent consisting of perfluoropropane-filled microbubbles with a sonicated albumin coating. Chatterjee and Sarkar (2003) start their motivation by argueing that homogeneous (in all three dimensions) shell properties and isotropic conditions are not

consistent with a shell that is only a few molecules thick and expect that the shell is highly nonhomogeneous in the thickness direction.

They suggest a molecular model of the shell as an alternative for the traditional approach of a shell with bulk-incompressible material properties. Molecular models are however expensive to compute and Chatterjee and Sarkar (2003) suggest a different approach by using an interface model that has a continuum character only in the in-plane direction and therefore does not suffer from the above criticism.

The shell was modeled using the Newtonian interfacial rheological model, which means that only viscous interfacial stresses are taken into account. The model interface has no thickness and the properties of the shell are formulated as an interfacial dilatational viscosity κ_s and an interfacial tension γ (which is actually the same as σ, but we follow the notation by Chatterjee and Sarkar (2003) and Sarkar et al. (2005) here).

$$\begin{aligned} \rho_l \left(R\ddot{R} + \frac{3}{2}\dot{R}^2 \right) &= \left(p_0 + \frac{2\gamma_0}{R_0} \right) \left(\frac{R_0}{R} \right)^{3\kappa} \\ &\quad - \frac{4\mu_l \dot{R}}{R} - \frac{2\gamma}{R} - \frac{4\kappa_s \dot{R}}{R^2} - p_0 - P(t) \end{aligned} \tag{2.17}$$

Parameters for Optison were determined by fitting the model to attenuation data, which required the assumption of small-amplitude oscilations and using a linearized equation of motion. It is stated that material properties were assumed to be independent of the amplitude of oscillation and the transmit frequency (1-10 MHz). The obtained values were $\gamma = 0.9$ N/m and $\kappa_s = 0.08$ kg/s. It was expected that the surface tension would decrease due to the absorption of surface active material, this is in contrast with the obtained value of 0.9 N/m, which is much higher than 0.072 N/m for a pure gas-water interface. The explanation for this is that in the absence of an explicit surface elasticity term, all elastic effects were lumped in the surface tension term. In the follow-up study by Sarkar et al. (2005) the Newtonian viscous encapsulation was changed into a non-Newtonian viscoleastic interface.

The model predicted a nonlinear subharmonic response in contrast to the model by Hoff et al. (2000). It is stressed by Chatterjee and Sarkar (2003) that the coating drastically reduces the influence of the resonance frequency on the backscattering of the contrast agent.

2.6.7 Allen (2004)

The approach by Allen and Rashid (2004) has a wide scope and a purely mechanical setting compared to most studies dedicated to ultrasound contrast agents. The model was tested for an ultrasound setting using representative physical parameters based on the studies by Church (1995) and Hoff et al. (2000). Allen and Rashid (2004) consider the case of a polymeric sphere. Whereas previous models mostly used Hooke's law to describe the stress-strain relationship of the coating, Allen and Rashid (2004) used the extended law for large deformations, the neo-Hookean constitutive equation.

A neo-Hookean material is a type of hyperelastic material. Hyperelasticity, or rubber elasticity, is often observed in polymers. These polymers are cross-linked. When a stress is applied to this cross-linked polymer, the polymer chains can initially move relative to each other. Then, at a certain point the covalent cross links will not allow more stretching of the polymer chains, which causes a dramatic increase in the elastic modulus of the material.

A generalized form of the neo-Hookean solid is the Mooney-Rivlin solid. Tsigliflis and Pelekasis (2008) apply the Mooney-Rivlin material law to model the polymer contrast agent Sonazoid. The Mooney-Rivlin solid model usually fits experimental data better than the Neo-Hookean solid model does, but requires an additional empirical constant.

In the model by Allen and Rashid (2004), the coating is assumed to have a certain thickness, hence an inner radius R_1 and outer radius R_2 are defined. Furthermore, the coating is represented by a shear modulus G_s and a density ρ_s. The coating is surrounded by Newtonian fluid and the gas core consists of an ideal adiabatic gas. Like in most studies, thermal damping was not taken into account.

The governing equation was investigated computationally for different system parameters in an ultrasound setting. A key feature of the system response mentioned is that it has the possibility of unstable expansion of the shell under large-amplitude forcing.

$$
\begin{aligned}
M(x)\frac{d^2x}{dr^2} + H(x)\left(\frac{dx}{dr}\right)^2 + G(x)\frac{dx}{dr} + K(x) &= -\frac{1}{q} \\
M(x) &= (1-\beta)\frac{x^2}{(x^3+\Delta)^{1/3}} + \beta x \\
H(x) &= (1-\beta)\left(\frac{3x^4+4x\Delta}{2(x^3+\Delta)^{4/3}}\right) + \frac{3}{2}\beta \\
K(x) &= \left(\frac{1+\Delta}{x^3+\Delta}\right)^{4/3} - \frac{1}{x^4} + 4\left(\frac{1+\Delta}{x^3+\Delta}\right)^{1/3} - \frac{4}{x} - \frac{p_{g,0}}{G_s}\left(\frac{x_0}{x}\right)^{3\kappa} \\
G(x) &= 4\left(\frac{\mu}{R_1\sqrt{G_s\rho_f}}\right)\frac{x^2}{\Delta+x^3}
\end{aligned}
\tag{2.18}
$$

where $x = R/R_1$ is the dimensionless time dependent inner radius, $\Delta = R_2^3/R_1^3 - 1$ and $\beta = \rho_s/\rho_l$.

2.6.8 Sarkar (2005)

Chatterjee and Sarkar (2003) already mentioned in their study that the calculated surface tension they found had no physical basis. Sarkar et al. (2005) therefore improved the model by Chatterjee and Sarkar (2003) by extending the interfacial tension with an elasticity term χ that depends on the shell interfacial area, $\gamma = \gamma_0 + \chi\left[\left(\frac{R}{R_0}\right)^2 - 1\right]$.

The same procedure was followed as in Chatterjee and Sarkar (2003) to determine the shell parameters of the contrast agent Sonazoid (GE Healthcare, Chalfont St Giles, UK). Sonazoid is a polymer-coated microbubble filled with perfluorocarbon. The interfacial tension γ_0 was 0.019 N/m, the dilatational viscostity κ_s was 0.01 kg/s and the dilatational elasticity χ was 0.51 N/m.

$$\begin{aligned}\rho_l\left(R\ddot{R}+\frac{3}{2}\dot{R}^2\right) &= p_{g,0}\left(\frac{R_0}{R}\right)^{3\kappa}-\frac{4\mu_l\dot{R}}{R}-\frac{4\kappa_s\dot{R}}{R^2}\\ &\quad-\frac{2\gamma_0}{R}-\frac{2\chi}{R}\left[\left(\frac{R}{R_e}\right)^2-1\right]-p_0-P(t)\\ p_{g,0} &= p_0+\frac{2\gamma_0}{R_0}+\frac{2\chi}{R_0}\left[\left(\frac{R}{R_e}\right)^2-1\right]\end{aligned} \tag{2.19}$$

Predictions for fundamental and subharmonic scattering were compared with predictions from the models by Chatterjee and Sarkar (2003) and Hoff et al. (2000). Calculated fundamental scattering values were comparable between the models and approximated measured values. This was not the case for the subharmonic scattering. The models showed different results for the frequencies applied with respect to measured subharmonic scattering. The performance of the model by Chatterjee and Sarkar (2003) without shell elasticity was better than the viscoelastic model, which consistenly underpredicted the subharmonic responses. They proposed for future work an elasticity parameter that "softens" with increasing fractional area.

2.6.9 Marmottant (2005)

The goal of the formulation by Marmottant et al. (2005) is to model phospholipid-coated microbubbles at large amplitudes. Inspired by the surface tension measurements of flat monolayers using Langmuir-Blodgett balances, they define an effective surface tension, which depends on the surface concentration of molecules. This resulted in a description of bubble dynamics governed by an *ad hoc* law for the surface tension.

The lipid coating is considered to be a viscoelastic solid in a narrow regime of radii. In this regime, the coating is modeled similar to the first approach by de Jong et al. (1994). Outside this regime, the bubble is assumed to be buckled or ruptured. In the first case, the bubble is smaller than a defined $R_{buckling}$, the surface tension and the elastic term vanish. In the second case, when the surface tension exceeds $\sigma_{break-up}$, which is identical to when R exceeds $R_{rupture}$, the coating breaks up and the surface tension becomes equal to that of free bubbles and the elastic term becomes zero.

Whereas the elasticity of the coating depends on the bubble radius, the viscosity remains constant. For this term, Chatterjee and Sarkar (2003) were followed. The modified Rayleigh-Plesset equation by Keller and Miksis (1980) was used, see Eq (2.12). Responses of the phospholipid-coated contrast agents SonoVue and BR14 (Bracco) were

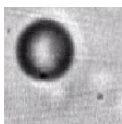

modeled, whereby it was assumed that the gas core consisted of an ideal adiabatic gas.

$$\rho_l\left(R\ddot{R}+\frac{3}{2}\dot{R}^2\right) = \left(P_0+\frac{2\sigma(R_0)}{R_0}\right)\left(\frac{R_0}{R}\right)^{3\kappa}\left(1-\frac{3\kappa}{c}\dot{R}\right) - P_0-\frac{2\sigma(R)}{R}-\frac{4\mu_l\dot{R}}{R}-\frac{4\kappa_s\dot{R}}{R^2}-P_{ac}(t) \quad (2.20)$$

This equation is identical to a free gas bubble equation, except from the effective surface tension $\sigma(R)$ term and the shell viscosity term. The surface tension is expressed in terms of the bubble radius:

$$\sigma(R)=\begin{cases}0 & \text{if } R\leq R_{\text{buckling}}\\ \chi\left(\frac{R^2}{R^2_{\text{buckling}}}-1\right) & \text{if } R_{\text{buckling}}\leq R\leq R_{\text{break-up}}\\ \sigma_{\text{water}} & \text{if ruptured and } R\geq R_{\text{ruptured}}\end{cases} \quad (2.21)$$

Shell parameters (elasticity χ, viscosity κ_s, buckling radius $R_{buckling}$, and $\sigma_{break-up}$) were determined by fitting to optical recordings of vibrating contrast agent microbubbles.

An interesting feature of this model is that it is able to predict 'compression-only behavior'. This term indicates that the compression amplitude is greater than the expansion amplitude. Experiments with the high-speed camera system Brandaris 128 have revealed the existence of such asymmetric oscillations by the microbubbles, see de Jong et al. (2007) and chapter 4 of this thesis. The definition of a buckling radius and the sharp increase of the effective surface tension during the expansion phase provides an asymmetry in capillary pressure that is displayed in the radial response by compression-only behavior. In addition, it was recently found that this model is capable of predicting threshold behavior and subharmonic responses (Overvelde et al., 2008).

2.6.10 Doinikov (2007)

Most models treat the coating as an elastic solid using the Kelvin-Voigt constitutive equation. Others have considered the coating as a viscous Newtonian fluid. Doinikov and Dayton (2007) propose a Maxwell constitutive equation. A Maxwell material behaves at fast expansion as a solid and at slow expansion as a fluid. Moreover, stresses in a Maxwell material can relax with time. According to Doinikov and Dayton (2007), a linear Maxwell constitutive equation is the appropriate choice to describe the motion of a lipid-coated microbubble.

The gas core is assumed to be adiabatic and is surrounded by a viscous Newtonian fluid. The goal is to demonstrate physical differences between the Maxwell shell model, the Kelvin-Voigt and the viscous Newtonian based models (*e.g.* (Sarkar et al., 2005) in the regime of linear oscillation. The parameters consist of a shell density ρ_s, a relaxation time λ, a shell viscosity μ_s an inner radius R_1 and outer radius R_2 and accompanying surface tensions σ_1 and σ_2. Parameter values are chosen based on values found in the

literature.

$$\begin{aligned}\rho_s R_1 \ddot{R}_1 \quad \left[1+\left(\tfrac{\rho_l-\rho_s}{\rho_s}\right)\tfrac{R_1}{R_2}\right] + \rho_s \dot{R}_1^2 \left[\tfrac{3}{2}+\left(\tfrac{\rho_l-\rho_s}{\rho_s}\right)\left(\tfrac{4R_2^3-R_1^3}{2R_2^3}\right)\tfrac{R_1}{R_2}\right] = \\ \left(p_0+\tfrac{2\sigma_1}{R_{1,0}}+\tfrac{2\sigma_2}{R_{2,0}}\right)\left(\tfrac{R_{1,0}}{R_1}\right)^{3\kappa} - \tfrac{2\sigma_1}{R_1} - \tfrac{2\sigma_2}{R_2} - p_0 - P(t) \\ - 4\mu_l \tfrac{R_1^2\dot{R}_1}{R_2^3} - 4\mu_s \tfrac{B(t)(R_{2,0}^3-R_{1,0}^3)}{R_1^3 R_2^3} \\ \text{where} \quad B(t)+\lambda\dot{(}B)(t) = R_1^2\dot{R}_1 \end{aligned} \tag{2.22}$$

The damped resonance frequency of a coated-bubble is higher than that of a free bubble when the elastic properties of the shell dominate its viscous properties. For an elastic shell such as with the Kelvin-Voigt shell model, this is always the case. Maxwell shells can however behave in both a viscous and elastic manner, depending on the choice of shell parameters. In general, it can be said that the Maxwell-coated bubbles compared to Kelvin-Voigt-coated microbubbles show more resemblance with free gas bubbles.

2.6.11 Stride (2008)

Stride (2008) considers bubbles that are stabilized by surfactants. The presence of a layer of adsorbed molecules onto the gas-liquid interface has a significant effect upon the microbubble's stability and its dynamic behavior, because this layer affects the surface tension of the gas-liquid interface. Like in the studies by Sarkar et al. (2005) and Marmottant et al. (2005), this is the starting point of the study by Stride (2008). Whereas the model by Marmottant et al. (2005) has an *ad hoc* law for the interfacial tension, Stride (2008) defines a continuous interfacial tension σ and shell viscosity μ_s, that vary as a function of the surface molecular concentration Γ.

The basis of the model is similar to most previous models. A spherical coated gas bubble of instantenous radius R is considered, which is suspended in an infinite, incompressible, Newtonian liquid. The thickness of the surfactant coating is neglected since it is much smaller than the radius of the microbubble.

$$\rho_l\left(R\ddot{R}+\frac{3}{2}\dot{R}^2\right) = p_g(R) - \frac{4\mu_l\dot{R}}{R} - \frac{2\sigma}{R} - \frac{4\mu_s\dot{R}}{R^2} - p_0 - P(t) \tag{2.23}$$

The interfacial tension σ and the surface viscosity μ_s are however not constant as with most previous bubble models, but depend on the bubble radius R and additional constants. σ for an insoluble film depends upon the concentration of adsorbed surfactant molecules at the interface and is expressed as

$$\sigma = \sigma_0 + \frac{K\Gamma_0^{y+1}}{(y+1)}\left(1-\left(\frac{R_0}{R}\right)^{2(y+1)}\right) \tag{2.24}$$

where σ_0 is the initial interfacial tension for $R=R_0$ and Γ is the initial concentration of surfactant on the bubble surface. K and y are respectively the constants of proportionality

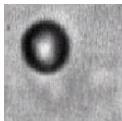

and exponent relating σ and Γ through a power law (Stride, 2008). Similarly, μ_s depends upon $\Gamma \propto R^{-2}$, which is given by

$$\mu_s = \mu_{s,0} exp\left(\frac{Z R_{buckling}^2}{(R^2 - R_{buckling}^2)}\right) \tag{2.25}$$

where $\mu_{s,0}$ and Z are constants for a given surfactant and $R_{buckling}$ is the limiting bubble radius beneath which the surface buckles and the interfacial tension will be reduced to zero (Stride, 2008).

The values of the parameters are based on values found in literature. The effect of a coating on the resonance frequency and amplitude of the microbubble response is investigated by comparing the results for a coated-microbubble with a free gas microbubble. Following Marmottant et al. (2005), this model is able to predict radial responses showing compression-only behavior. Stride (2008) explains that both the interfacial tension (Eq (2.24)) and surface viscosity terms (Eq (2.25)) may be nonlinear depending on the values of y and Z. In addition, there may exist upper and lower concentration limits for which the interfacial tension is respectively zero (corresponding to the buckling radius $R_{buckling}$) and equal to the 'clean' liquid-gas interfacial tension and at which there will be sharp changes in the resistance to oscillation.

2.6.12 Tsiglifis (2008)

The aim of the paper by Tsiglifis and Pelekasis (2008) is to model the microbubble dynamics at large acoustic pressures. In previous studies often Hooke's law was applied to model the coating behavior. Hooke's law assumes a constant stress-strain relationship and thus a constant elasticity (the Young's modulus) of the coating independent of the degree of stretch imposed on the coating. In this paper, the effect of strain softening and hardening of the coating is investigated. Strain softening implies that the stress-strain relationship has a decreasing slope as the deformation increases and strain hardening has the opposite result.

Barthès et al. (2002) have shown that a Mooney-Rivlin constitutive law can be used to model a strain softening capsule and that the Skalak law can be used to model a strain hardening membrane. Tsiglifis and Pelekasis (2008) implements both types of materials in a Keller and Miksis (1980) equation and compare the results with a Kelvin-Voigt based model.

The following nonlinear differential equation describing spherically symmetric oscillations in a compressible liquid is used

$$(1 - M\dot{R}')R'\ddot{R}' + \left(\frac{3}{2} - \frac{M\dot{R}'}{2}\right)\dot{R}'^2 = (1 + M\dot{R}')(p_l|_{r=R} - p_0' - P(t)') + MR'\tfrac{d}{dt}(p_l|_{r=R} - P(t)') \tag{2.26}$$

where primed letters denote dimensionless variables, M is the Mach number, $M = \omega R_0/c$, which is assumed to be small, but not negligible. The model is completed by

calculating the liquid pressure $p_l|_{r=R}$ that is exerted on the membrane by formulating a force balance for the gas-liquid interface, which relates this liquid pressure to the instanteneous pressure inside the bubble, the viscous stresses in the liquid and the viscoelastic stresses that develop on the membrane due to its radial deformation and velocity. The viscoelastic stresses on the membrane follow from the constitutive equation governing the mechanical behavior of the membrane.

This constitutive law is substituted into the equation for $p_l|_{r=R}$ resulting in the following expressions. In case of the strain-hardening Skalak law,

$$\begin{aligned} P_l|_{r=R} &= \left(\frac{1}{R'}\right)^{3\kappa}\left[p'_0+\frac{2}{We}+2G'_s\left[\left(\frac{1}{1-u'_0}\right)^2(1-C_s)\right.\right. \\ &\left.\left.+C_s\left(\frac{1}{1-u'_0}\right)^6-1\right]\right]+-\frac{2}{WeR'}-\frac{4\dot{R}'}{Re_lR'} \\ &-\frac{2G'_s}{R'}\left[\left(\frac{R'}{1-u'_0}\right)^2(1-C_s)+C_s\left(\frac{R'}{1-u'_0}\right)^6-1\right] \\ &-\frac{4\dot{R}'}{Re_lR'^2}\mu'_s \end{aligned} \tag{2.27}$$

where We is the Weber number, Re_l is the Reynolds number, and u_0 is the initial displacement of the radial wall that determines the residual stresses inside the membrane. Parameter C_s is always positive and controls the extend of area incompressibility of the membrane. In case of red blood cells $C_s >> 1$ in order to accommodate the almost incompressible nature of the membrane area.

For the strain-softening Mooning-Rivlin law, the following expression was derived

$$\begin{aligned} P_l|_{r=R} &= \left(\frac{1}{R'}\right)^{3\kappa}\left[p'_0+\frac{2}{We}+2G'_s[1-(1-u'_0)^6]\right. \\ &\left.\left[1+b\left[\left(\frac{1}{1-u'_0}\right)^2-1\right]\right]\right]+\frac{2}{WeR'}-\frac{4\dot{R}'}{Re_lR'} \\ &-\frac{2G'_s}{R'}\left[1-\left(\frac{1-u'_0}{R'}\right)^6\right] \\ &\left[1+b\left[\left(\frac{R'}{1-u'_0}\right)^2-1\right]\right]-\frac{4\dot{R}'}{Re_lR'^2}\mu'_s \end{aligned} \tag{2.28}$$

where parameter b ranges between 0 and 1. The case with $b = 0$ corresponds to a neo-Hookean membrane and when b tends to zero the membrane becomes softer.

The shear modulus G'_s and shell viscosity μ'_s have different values for the different constitutive laws. These values were fitted and based on experimental data found in literature for SonoVue (Gorce et al., 2000), Sonazoid (Sarkar et al., 2005) and Albunex

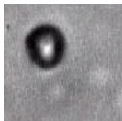

(de Jong and Hoff, 1993). Acoustic responses from the strain softening and strain hardening models were compared to responses from a Kelvin-Voigt approach. Furthermore, the effect of an increasing acoustic pressure on the amplitude of microbubble oscillation was investigated for different values of b and C_s. They found that a microbubble with a coating with a strain-softening nature shows an abrupt increase in oscillation amplitude when the acoustic pressure is increased, which they compare with the threshold behavior as was experimentally found by Emmer et al. (2007b) (chapter 5), see also the discussion in chapter 11.

2.7 Summary of developments in UCA modeling

Over the years, a great variety of coated bubble models have been developed. The basis of the Rayleigh-Plesset equation has remained unchanged. Modeling of the shell has developed analogous to the development of new contrast agents and the release of new experimental data.

The first coated bubble models applied the Kelvin-Voigt constitutive equation, which predicts a linear relationship between stress and strain. The contrast agents available at the time had an albumin shell (*e.g.* Albunex and Quantison) and were considered to be relatively stiff and elastic. The advantage of the Kelvin-Voigt law is that the coating is modeled from a physical basis using two parameters, the elasticity and the viscosity. Models applying the Kelvin-Voigt constitutive equation are de Jong et al. (1994); Church (1995); Hoff et al. (2000); Khismatullin and Nadim (2002) and Marmottant et al. (2005), the latter used this law for the regime of small oscillation amplitudes.

Morgan et al. (2000); Marmottant et al. (2005); Tsiglifis and Pelekasis (2008) assume that the liquid surrounding the bubble is slightly compressible. The other models assume an incompressible Newtonian liquid except for Khismatullin and Nadim (2002), who investigated the effect of a compressible liquid in the coated bubble dynamics and came to the conclusion that the effect of the liquid is outweighed by the effect of the coating.

The models by Morgan et al. (2000); Chatterjee and Sarkar (2003) were the first models that did not contain the Kelvin-Voigt constitutive equation. Chatterjee and Sarkar (2003) consider Optison and argue that the albumin shell is only a few molecules thick, which they model with a Newtonian interfacial rheological model whereby only viscous interfacial stresses are taken into account. Morgan et al. (2000) consider MP1950, which has a coating consisting of a flexible monolayer of phospholipid molecules. Both approaches however resulted in models whereby the physical basis can be argued. To improve this physical basis, Sarkar et al. (2005) extended the model by Chatterjee and Sarkar (2003) with an elasticity term. This elasticity term is the same as the term used in the model by de Jong et al. (1994) and in the linear regime of the model by Marmottant et al. (2005).

Doinikov and Dayton (2007) applied instead of the Kelvin-Voigt constitutive law, the linear Maxwell constitutive law in order to improve the predictions for lipid-coated microbubbles. This had the result that this model contains six parameters to describe

the coating instead of two as for the Kelvin-Voigt equation. However, also this model is especially designed for small amplitude oscillations.

Since 2004, models have been developed that contain constitutive equations valid for large deformations of the coating. The first of these kind of models was defined by Allen and Rashid (2004). They considered polymer spheres, which were assumed to have a neo-Hookean elastic response. The coating has a certain elasticity, but does not have a viscosity. The next model specifically developed for large deformations was proposed by Marmottant et al. (2005). This model is characterized by an *ad hoc* effective surface tension. In the linear regime, the model by Marmottant et al. (2005) equals that of de Jong et al. (1994). The elasticity of the coated bubbles changes between the different regimes (buckled, elastic, ruptured) whereas the viscosity remains constant. This model is capable of predicting nonlinear behavior such as compression-only behavior and subharmonic responses.

Recently, Tsiglifis and Pelekasis (2008) modeled the coating using a dynamic elasticity term. A constitutive law relates the elasticity of the coating to the microbubble radius. The coating elasticity can either 'soften' or 'harden', which also requires the addition of an empirical parameter. The coating viscosity remains fixed like in the model by Marmottant et al. (2005).

Finally, Stride (2008) has defined a model, which is not specifically meant for large deformations, but it does include two dynamic coating parameters. The coating viscosity as well as the coating elasticy depend on the instantaneous radius of the microbubble. These coating viscosity and elasticity do not follow from a constitutive law, but from a description of interfacial tension for insoluble films. The model by Stride (2008) has four additional parameters, which are necessary to set the coating elasticity and viscosity.

2.8 Conclusions

We have seen that two different representations of the coated microbubble can be adopted to predict its dynamics, which are the phenomenological model and the theoretical model. The phenomenological model has a more practical point of view compared to the theoretical model and translates experimentally observed behavior into physical relationships. Within the scope of this approach the coating can be considered as a collection of interacting molecules, which results in specific coating properties. Examples of models which have been built from this philosophy are the models by de Jong et al. (1994); Marmottant et al. (2005); Stride (2008).

Using a theoretical model, the individual molecules of the coating are disregarded, the coating is considered as a continuum. The behavior of such a continuum can be predicted using a constitutive law. Church (1995) followed this approach and more recently Doinikov and Dayton (2007) and Tsiglifis and Pelekasis (2008) did the same.

It is apparent that these approaches are not mutually exclusive. In the phenomenological model, physical laws are applied to derive separate terms, but also a constitutive law such as the Mooney-Rivlin law is essentially phenomenological. It is therefore important

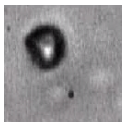

to realize the benefits and drawbacks of both approaches. The phenomenological approach has the advantage that it results in a more physically understandable model, but it has a less rigorous basis compared to the theoretical approach. The theoretical approach has a more firm mathematical basis, but also has a greater risk that the coating is modeled using a large number of parameters. A large number of empirical parameters increases the possibilities to fit predictions by the model to experimentally obtained results, but their physical value should be discussed.

The ultimate coated bubble model is able to predict experimentally observed coated bubble responses for all possible input parameters, such as different transmit frequencies, acoustic pressures and bubble radii. The ultimate coated bubble model has not been achieved yet. For this purpose, we need to improve our knowledge on coated bubble behavior in ultrasound fields, which is therefore one of the motivations for this thesis.

Table 2.1: Ultrasound contrast agent models

Author	Year	Governing equation	Liquid model	Constitutive equation	Coating elasticity	Coating viscosity	Coating thickness	Amplitude regime
De Jong	1994	Rayleigh-Plesset	Newtonian	Viscoelastic	S_p [N/m]	S_f [kg/s]	-	small
Church	1995	Rayleigh-Plesset	Newtonian	Kelvin-Voigt	G_s [Pa]	μ_s [Pa s]	thick	small
Hoff	2000	Rayleigh-Plesset	Newtonian	Kelvin-Voigt	G_s [Pa]	μ_s [Pa s]	thin	small
Morgan	2000	Modified Herring	Newtonian	Viscoelastic	χ [N/m]	μ_s [Pa s]	thin	semi-large
Khismatullin	2002	Same order as Keller-Miksis	Oldroyd	Kelvin-Voigt	G_s [Pa]	μ_s [Pa s]	thin	small
Chatterjee	2003	Rayleigh-Plesset	Newtonian	Newtonian viscous	[1]	κ_s [kg/s]	-	small
Allen	2004	Rayleigh-Plesset	Newtonian	neo-Hookean	G_s [Pa]	-	thick	large
Sarkar	2005	Rayleigh-Plesset	Newtonian	Viscoelastic	χ [N/m]	κ_s [kg/s]	-	small
Marmottant	2005	Keller-Miksis	Newtonian	Dynamically viscolelastic	χ [N/m]	κ_s [kg/s]	-	large
Doinikov	2007	Rayleigh-Plesset	Newtonian	Maxwell	[2]	μ_s [Pa s]	thin	small
Stride	2008	Rayleigh-Plesset	Newtonian	Dynamically viscoelastic	[3]	$\mu_s(R)$ [Pa s]	-	large
Tsiglifis	2008	Keller-Miksis	Newtonian	Skalak	$G_s(R)$ [Pa], C	μ_s [Pa s]	-	large
Tsiglifis	2008	Keller-Miksis	Newtonian	Mooney-Rivlin	$G_s(R)$ [Pa], b	μ_s [Pa s]	-	large

[1]: σ [N/m] is fitted to experimental data

[2]: shell parameters consist of σ_1 [N/m], σ_2 [N/m], λ [s], and ρ_s [kg/m^3]

[3]: elasticity part of $\sigma(R)$ [N/m], which follows from surface lipid concentration

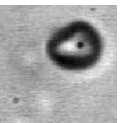

3

A model for large amplitude oscillations of coated bubbles accounting for buckling and rupture

Philippe Marmottant, Sander van der Meer, Marcia Emmer, Michel Versluis,
Nico de Jong, Sascha Hilgenfeldt, and Detlef Lohse

Journal of the Acoustical Society of America, 2005, 118(6):3499-3505

Abstract We present a model applicable to ultrasound contrast agent bubbles that takes into account the physical properties of a lipid monolayer coating on a gas microbubble. Three parameters describe the properties of the shell: a buckling radius, the compressibility of the shell and a break-up shell tension. The model presents an original non-linear behaviour at large amplitude oscillations, termed compression-only, induced by the buckling of the lipid monolayer. This prediction is validated by experimental recordings with the high-speed camera Brandaris 128, operated at several millions of frames per second. The effect of aging, or the resultant of repeated acoustic pressure pulses on bubbles, is predicted by the model. It corrects a flaw in the shell elasticity term previously used in the dynamical equation for coated bubbles. The break-up is modeled by a critical shell tension above which gas is directly exposed to water.

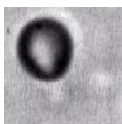

3.1 Introduction

To enhance ultrasound echographic imaging, micrometric coated bubbles are used as contrast agents. Coating materials include lipid monolayers, polymer shells, or thick solid shells. The coating stabilizes the bubbles and prevents their coalescence. Pulmonary alveoli in the lungs have a lipidic coating for the same reason (Crane and Hall, 2001). The coating modifies the effective surface tension. Since surface tension plays a crucial role in the dynamics of small bubbles, when the capillary pressure term is of the order of the static ambient pressure, the coating is expected to strongly influence the dynamics.

All current models developed to describe coated bubble oscillations implicitly assume small deformations of the bubble surface: however, in practice, insonifying contrast agent bubbles produces oscillations with large variations in the surface area. We will present in this manuscript a model designed to incorporate the effect of a coating on the microbubble response to ultrasound, and to specifically capture the high-amplitude dynamics.

We focus on phospholipidic monolayer coatings, used in several contrast agent bubbles (Klibanov, 2002). The phospholipid molecules naturally adsorb to the interface (Lee et al., 2001) and shield the water from the air, reducing the surface tension σ to a value lower than that of pure water (73 mN/m). Surface tension can be measured in a flat monolayer with the Langmuir-Blodgett balance, or on centimetric bubbles (Crane et al., 1999), showing its dependence on the surface concentration of molecules.

The compression of the monolayer decreases the area available per molecule. When this area reaches that covered by the lipid molecules (typically 0.4 nm^2 for phospholipids in the transconfiguration normal to the interface), the effective surface tension decreases sharply, see Fig 3.1. The variation of surface tension with the area A is expressed with the elastic compression modulus defined by $\chi = A\frac{d\sigma}{dA}$ (of order 0.2 N/m for a slow compression, as derived from the steepest slopes of Fig 3.1). Further compression leads to an unstable situation where the monolayer buckles out of plane, while the surface tension nearly vanishes. A spectacular demonstration of the buckling is the appearance of wrinkles on coated bubbles when their gas dissolves out (Borden and Longo, 2002). Buckling can be reversible (**??**). Vanishing surface tensions were revealed by the microscopic observation of bubbles with a monolayer lipid coating in a solid state: these bubbles could assume a steady nonspherical shape (Kim et al., 2003) when deformed with a micropipette, and dissolution was greatly reduced by the absence of the capillary overpressure (Duncan and Needham, 2004).

In contrast, a slow expansion separates molecules from each other: surface tension rises. A monolayer made from pure lipid (one species only) will show phase changes from a two-dimensional (2D) solid state, to a liquid and eventually gaseous state, where surface tension is close to that of water. With a mixture of lipid molecules the phase changes are not necessarily present, and a 2D solid can rupture during expansion, leaving rafts of solid phospholipid molecules separated by clean interfaces (Graner et al., 1995).

Most previous existing experimental data on phospholipidic monolayers were col-

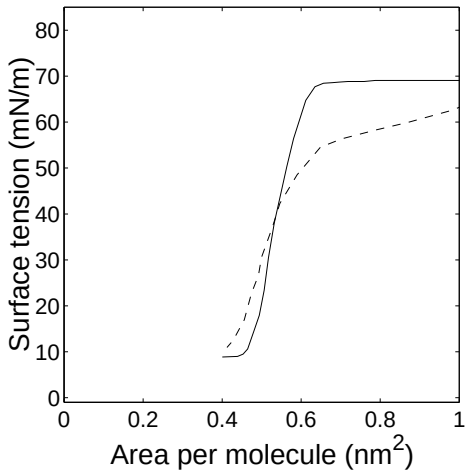

Figure 3.1: Effective surface tension versus area per molecule at the interface for two phospholipids (both present in the contrast agent SonoVue (Schneider et al., 1995)) under *slow compression* at a few percent per minute: distearoylphosphatidylcholine (DSPC), solid line; and dipalmytoylphosphatidylglycerol (DPPG), broken line. Curves redrawn from Pétriat et al. (2004) and Sández et al. (2002).

lected at very slow compression/expansion rates, when molecules at the interface could equilibrate. Only a few experiments tackled the high-frequency and thus out-of equilibrium trends: the buckling surface tension comes closer to zero and the elastic modulus becomes higher (see reported experiments (Crane and Hall, 2001) with pulmonary surfactant compressed within 0.2 s). These findings give some hint to the extrapolation of surface properties to the realm of high frequency oscillations, the one we are going to explore with oscillating contrast agent bubbles.

3.2 Model

3.2.1 Effective surface tension of a bubble during its oscillation

At high frequencies, we propose to model the effective surface tension σ of the lipidic monolayer of a bubble along three linear regimes inspired from the low frequency observations. The regimes depend on the bubble area $A = 4\pi R^2$, with R the bubble radius (see Fig 3.2). This simplified model is designed to capture the coated bubble dynamics with a minimum of parameters.

The model has three parameters only to describe the surface tension: the buckling area of the bubble A_{buckling} below which the surface buckles, an elastic modulus χ that gives the slope of the elastic regime. The third parameter is incorporated to describe

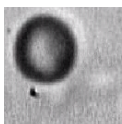

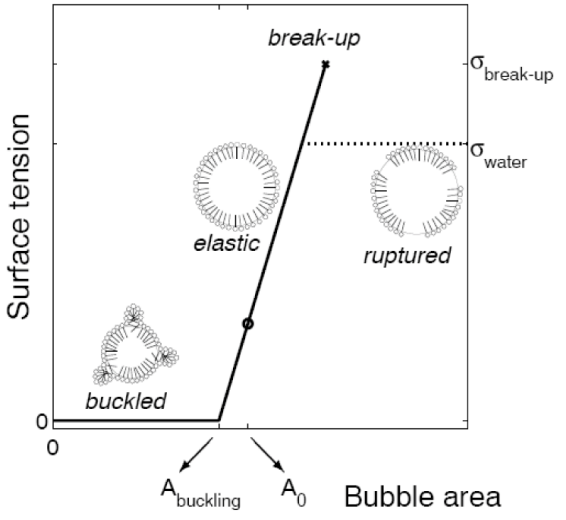

Figure 3.2: Model for the dynamic surface tension of a monolayer coated bubble (continuous line). The coating has a fixed number of lipid molecules, which corresponds to a monolayer at equilibrium (when area A_0). The tension saturates to the water value σ_{water} (broken line) after the break-up tension has been reached ($\sigma_{break-up} > \sigma_{water}$, see main text).

the moment of rupture: the elastic regime holds until a critical break-up tension called $\sigma_{\mathrm{break-up}}$. When this limit has been reached the maximum surface tension saturates at σ_{water}.

We motivate here the modeling of the three states:

- Buckled state, $\sigma = 0$.
  Consistent with experimental findings on the fast compression of pulmonary phospholipid monolayers, we assume a near vanishing surface tension in the buckled state (Crane and Hall, 2001). The buckling area of the bubble depends on the number n of lipid molecules at the interface and on the molecular area at buckling a_{buckling}, with $A_{\mathrm{buckling}} = n\, a_{\mathrm{buckling}}$, with a_{buckling} typically of the order of 0.4 nm^2, see previous section. Note that a first compression of the bubble might *expel* in bulk some molecules into the bulk (Gaines and George, 1966), decreasing the number n. After this transient expulsion, and for moderate driving amplitudes and short exposures, we expect the number of molecules to remain constant, as phospholipids with long carbon chains are poorly soluble.

- Elastic state, $\sigma = \chi \left(\frac{A}{A_{\mathrm{buckling}}} - 1 \right)$.
  The shell is elastic only in a narrow area range. The lower limit is A_{buckling} for

the area, or equivalently R_{buckling} for the radius. The upper limit radius is fixed by the maximum surface tension, which is $\sigma_{\mathrm{break-up}}$ before rupture of the shell giving $R_{\mathrm{break-up}} = R_{\mathrm{buckling}}(1+\sigma_{\mathrm{break-up}}/\chi)^{1/2}$, or σ_{water} after rupture giving $R_{\mathrm{ruptured}} = R_{\mathrm{buckling}}(1+\sigma_{\mathrm{water}}/\chi)^{1/2}$. The elastic regime holds only in a narrow range of radii, since χ is usually large compared to $\sigma_{\mathrm{break-up}}$ or σ_{water}. The value of the elastic modulus can also incorporate the presence of any solid-like shell material that sustains tensile stress (such as the polyethyleneglycol polymer in Sonovue contrast agent bubbles (Schneider et al., 1995). We assign a constant elastic modulus in this state, slightly caricaturing the quasi-static profiles of Fig 3.1, a simplification of the model to facilitate calculation.

Within this regime the surface tension is a linear function of the area, or of the square of the radius, and for small variations around a given radius R_0, it can be writen as:

$$\sigma(R) = \sigma(R_0) + \chi\left(\frac{R^2}{R_0^2} - 1\right) \quad \simeq \sigma(R_0) + 2\chi\left(\frac{R}{R_0} - 1\right) \quad \text{when} \quad |R - R_0| \ll R_0. \tag{3.1}$$

The lipid monolayer behaves as if composed of a thin solid and elastic material, see the appendix for the derivation of the tension of a thin elastic shell.

- Ruptured state, $\sigma = \sigma_{\mathrm{water}}$.
  A fast expansion, such as the one triggered on a bubble by an ultrasonic pressure pulse, does not allow much time for any phase change and the monolayer is likely to break at a critical tension $\sigma_{\mathrm{break-up}}$, exposing bare gas interfaces to the liquid. The bare interface has a tension value of σ_{water}. The break-up tension can be higher than σ_{water}, since any polymer component confers more cohesion to the shell, and shifts the break-up to higher tensions. The introduction of a high tension break-up was motivated by the observation of resistant bubbles, as will be exposed further.

  After break-up we assume that surface tension relaxes to σ_{water}. Even if the phospholipid monolayer rafts are likely to display non-isotropic tensions and shear stresses (being solid), the expansion is uniform before rupture, and the stress is likely to remain close to uniformity on average. The average tension value is settled in this case by the local mechanical equilibrium between the solid rafts and the bare interfaces, the latter pulling with the tension σ_{water}.

3.2.2 Dynamics of the coated bubble

During the oscillation, the dynamical surface tension will vary, since it is a function of the bubble area and therefore of the bubble radius. We therefore write the effective surface tension $\sigma(R)$ to emphasize this dependence. In motion, the balance of normal stresses at the interface reads

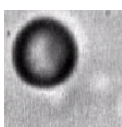

$$P_g(t) - P_l(t) = \frac{2\sigma(R)}{R} + 4\mu\frac{\dot{R}}{R} + 4\kappa_s\frac{\dot{R}}{R^2}, \tag{3.2}$$

with P_g the gas pressure in the bubble, P_l the liquid pressure, μ the surrounding liquid viscosity and κ_s the surface dilatational viscosity from the monolayer. The first term on right-hand side is the capillary pressure term, while the second is the stress arising from the frictions in the liquid and the third from frictions in the shell. The last term was initially derived for a layer of finite and constant thickness ϵ ($\epsilon \ll R$) by Morgan et al. (2000), the dilatational viscosity writing $\kappa_s = 3\epsilon\mu_{\text{lipid}}$, with μ_{lipid} the bulk lipid viscosity. Here we use only κ_s to describe the monolayer shell surface viscosity, following Chatterjee and Sarkar (2003). In this model κ_s does not depend on the surface area, nor does it exhibit any hysteresis. Note that the shear viscosity of the surface does not come into play in the present situation, because of the radial motion of the bubble.

The Laplace capillary pressure term writes $\frac{2\sigma(R)}{R}$ including the effective surface tension, *without any additional terms*, contrary to a previous statement in an article by Glazman (1983), who expressed the capillary pressure by the erroneous expression $\frac{2\sigma}{R} + \frac{\partial\sigma}{\partial R} = \frac{2}{R}(\sigma + \chi(\frac{R_0}{R})^2)$. We demonstrate here why: the capillary overpressure derives from the mechanical equilibrium of all forces acting on the interface (of vanishing mass), that is the infinitesimal work δW of the forces cancels out for small bubble radius variation. By definition, the work associated with a variation dA of the area is σdA (De Gennes et al., 2004), while the pressure work from a variation dV of the volume is $-(P_g - P_l)dV$. Owing to the mechanical equilibrium of the interface, the sum of these works vanishes, and we obtain the static capillary term of Eq (3.2). In the analysis by Glazman, the surface work is expressed incorrectly by $\sigma dA + Ad\sigma$ (instead of σdA) from the differentiation of a surface potential energy $E = \sigma A$: actually this last expression of the surface potential energy ($E = \int \delta W_{surface}$ by definition) is valid only when σ is constant.

The popular model of Morgan et al. (2000) for coated microbubbles improves the description of viscous frictions, but is based on the analysis of Glazman for the elasticity of the lipid shell, equivalent to the introduction of an effective surface tension $\sigma(R) = \sigma_0 + \chi(\frac{R_0}{R})^2$ that fails to describe a coated bubble. Physically it would mean that surface tension always decreases when the bubble is inflated, in contrast with the behavior of lipid monolayers or elastic solid shells.

The hydrodynamics of the liquid motion around the bubble is modeled by the (modified) Rayleigh-Plesset equation $\rho_l(R\ddot{R} + \frac{3}{2}\dot{R}^2) = P_l(t) - P_0 - P_{ac}(t) - \frac{R}{c}\frac{dP_g(t)}{dt}$, with P_0 the ambient pressure, $P_{ac}(t)$ the acoustic pressure, and c the velocity of sound in the liquid. This equation proved to be accurate and robust even in the extreme conditions of sonoluminescence Brenner et al. (2002). We choose an ideal polytropic ideal gas law $P_g \propto R^{-3\kappa}$, with κ the polytropic gas exponent. It is 1 for bubbles behaving isothermally, and equal to the ratio of specific heats for bubbles behaving adiabatically (Prosperetti, 1984) (close to 1.095 for SF_6). In the following, the thermal diffusion length in the gas during a period being small compared to the radius, we use the adiabatic version.

Combining the Rayleigh-Plesset equation and the polytropic gas law with the boundary condition (3.2) we obtain the model for the bubble dynamics:

$$\rho_l\left(R\ddot{R}+\frac{3}{2}\dot{R}^2\right) = \left(P_0+\frac{2\sigma(R_0)}{R_0}\right)\left(\frac{R}{R_0}\right)^{-3\kappa}\left(1-\frac{3\kappa}{c}\dot{R}\right) - \frac{2\sigma(R)}{R}-\frac{4\mu\dot{R}}{R}-\frac{4\kappa_s\dot{R}}{R^2}-p_0-P_{ac}(t) \tag{3.3}$$

with R_0 the equilibrium radius of the bubble. This equation is identical to a free gas bubble equation, except from the effective surface tension $\sigma(R)$ term and the shell viscosity term. The tension expressed in our monolayer model described above, and expressed here in terms of the bubble radius writes:

$$\sigma(R)=\begin{cases}0 & \text{if } R\leq R_{\text{buckling}}\\ \chi\left(\frac{R^2}{R_{\text{buckling}}^2}-1\right) & \text{if } R_{\text{buckling}}\leq R\leq R_{\text{break-up}}\\ \sigma_{\text{water}} & \text{if ruptured and } R\geq R_{\text{ruptured}}\end{cases} \tag{3.4}$$

The third regime appears after rupture of the shell, when $\sigma_{\text{break-up}}$ has been reached (see broken line of Fig 3.2).

For small vibration amplitudes within the tensed elastic state, the surface tension can be linearized around a constant value, with $\sigma(R)\simeq\sigma(R_0)+2\chi\,(R/R_0-1)$, from Eq (3.1). Implemented in the dynamical equation it yields the same pressure term $-2\sigma(R)/R=-2\sigma(R_0)/R-4\chi(1/R_0-1/R)$ as in the model proposed by de Jong et al. (1994) for thin elastic shells. The shell stiffness coefficient S_p they introduced is simply related to the present shell elasticity by $S_p=2\chi$, while their shell friction coefficient writes $S_f=12\pi\kappa_s$. We stress here again that the model by de Jong et al. (1994) is limited to small amplitudes of vibration (for effective tensions bounded between 0 and σ_{water}, or for R in between R_{buckling} and R_{collapse}), while the present model extends the oscillation to unbounded, large amplitudes.

3.2.3 Implications of the model: bubble compressibility

The effective tension model drastically changes the compressibility of the bubble. For slow variations of the ambient pressure P, at frequencies small compared to the resonance frequency, we can compute the equilibrium radius response, see Fig 3.3, setting $\dot{R}=0$ in equations (3.3) and (3.4).

From the equilibrium, we also derive the compression modulus of the bubble, K_V, with:

$$K_V=-V\left(\frac{dP}{dV}\right)=\begin{cases}\kappa P & \text{for the buckled state}\\ \kappa P+\frac{4}{3}\frac{\chi}{R} & \text{for the elastic state}\\ \kappa P+\frac{3\kappa-1}{3}\frac{2\sigma_{\text{water}}}{R} & \text{for the free bubble/ broken shell state}\end{cases} \tag{3.5}$$

with V the bubble volume, a polytropic exponent κ close to 1 for slow and isothermal compressions, and in the limit of $\chi\gg\sigma_{\text{water}}$ (usual for phospholipids). The compression

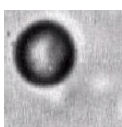

modulus is much higher when the bubble is in the elastic state: this is reflected in the much steeper slope of the curve of Fig 3.3. When the pressure is increased enough the bubble buckles, and becomes very compressible, even more than an uncoated free gas bubble of the same radius (whose internal pressure is increased by capillarity).

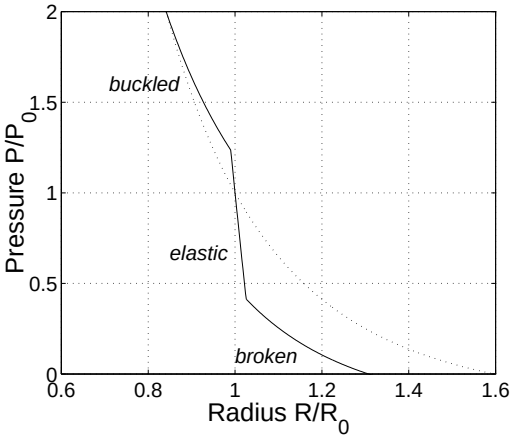

Figure 3.3: Ambient pressure versus equilibrium radius for a coated bubble (continuous line) and a free gas bubble (dotted line). At atmospheric pressure, the bubble radius is $R_0 = 2$ μm. The coated bubble is initially in the elastic state ($R_{\mathrm{buckling}} = 1.98$ μm, $\chi = 1$ N/m.)

The change in compressibility is reflected on the dynamics of small amplitude oscillations as well. The linearization of the equations, setting $R(t) = R_0(1+x(t))$, provides a damped oscillator equation $\ddot{x} + 2\gamma\dot{x} + \omega_0^2 x = -P_{ac}(t)/\rho_l R_0^2$, with a damping coefficient $\gamma = 2\mu/\rho_l R_0^2 + 2\kappa_s/\rho_l R_0^3 + 3\kappa(P_0 + 2\sigma(R_0)/R_0)/2c\rho_l R_0$, and an eigenfrequency simply writing:

$$\omega_0^2 = \frac{3}{\rho_l R_0^2} K_V. \tag{3.6}$$

In the free bubble state, this equation provides the Minnaert frequency as expected. It can be concluded that bubbles in the elastic state have a much higher resonance frequency than free or buckled bubbles, because their compression modulus is higher, consistently with the derivation of de Jong et al. (1994).

3.3 Results

3.3.1 Compression-only behavior

At small acoustic amplitudes, the model presented above provides a linear radius response to the pressure similar to other Rayleigh-Plesset models with constant surface

tension.

Under large pressure amplitudes, the bubble will experience an original nonlinear response. It will likely buckle in its compression phase, which cancels out any surface tension. On the other hand the surface tension rapidly rises during the expansion phase, and this asymmetry in surface tension provides an asymmetry in capillary pressure, especially strong for small bubbles. The radius response curve displays this asymmetry by a 'compression-only' behavior.

Recent experiments, realized with the high-speed camera Brandaris 128 (Chin et al., 2003), reveal the existence of such asymmetric oscillations of bubbles. The experiment was conducted as follows: Sonovue and BR14 contrast bubbles, supplied by Bracco Research SA, Geneva, Switzerland, were prepared in the vial about 24 hours prior to the recording of their dynamics. Both types of bubbles present a phospholipidic coating, Sonovue containing SF_6 gas (Schneider et al., 1995), while BR14 contains the even less soluble C_4F_{10} gas (Schneider et al., 1997). The contrast bubbles were led through a capillary fiber inside a small water-filled container. An Olympus microscope with a 60x high resolution water immersed objective and a 2x magnifier produced an image of the contrast bubbles. The image was then relayed to the high speed framing camera Brandaris 128. A broadband single element transducer was mounted at 75 mm from the capillary. A Tektronix AWG 520 arbitrary waveform generator provided a signal amplified by an ENI A-500 amplifier. The bubble response was investigated with sequential ultrasound bursts of 8 cycles at frequencies ranging from 1.5 MHz to 5 MHz. The camera was operated at a framing rate of 15 million frames per second, resolving the insonified microbubble dynamics. From the images (see Fig 3.4) the radius versus time curves for each individual bubble were extracted (Fig 3.5a), from which the compression-only behavior is apparent.

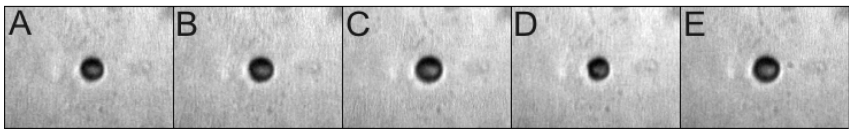

Figure 3.4: Consecutive images of a contrast agent bubble from the high speed camera Brandaris operated at 14.3 million frames per second (time intervals between images are thus 69.8 ns), during one ultrasound cycle, of frequency 2.6 MHz. The bubble radius is initially 1.95 μm, and frame number 4 shows the bubble compression.

This phenomenon is very well modeled with our effective surface tension model, see Fig 3.5b, assuming the bubble to be initially in a tension-less state ($R_{\mathrm{buckling}} = R_0$), and allowing the shell to support elevated tensions. Note that the fitted elastic modulus and shell viscosity of this shell are of the same order of magnitude than the average ones from attenuation measurements on bubble populations by Gorce et al. (2000), who deduced an average shell elasticity $\chi = S_p/2 = 0.55$ N/m and shell friction $\kappa_s = S_f/12\pi = 7.2 \times 10^{-9}$ kg/s.

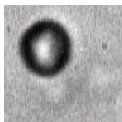

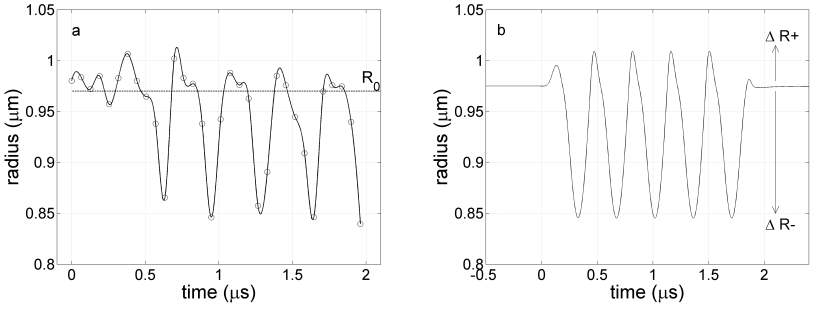

Figure 3.5: (a) Experimental recording of the radius of a SonoVue bubble vs time, with the fast framing camera Brandaris (beginning of a 2.9 MHz pulse with an acoustic pressure of 130 kPa). (b) Simulation. The fitted shell parameters are $R_{\mathrm{buckling}} = R_0 = 0.975$ μm, $\chi = 1$ N/m, $\kappa_s = 15 \times 10^{-9}$ kg/s and $\sigma_{\mathrm{break-up}} > 1$ N/m (resistant shell). The liquid properties are $\rho_l = 10^3$ kg/m^3, μ = 0.001 Pa s, c = 1480 m/s, and the polytropic gas exponent is κ = 1.095.

3.3.2 Aging of micro-bubbles: effect on the oscillation response

The initial effective tension of the monolayer depends on the history of the bubble. During their formation in the vial, lipid molecules are adsorbed at the interface, which reduces the effective surface tension, in proportion to the surface concentration n/A of adsorbed lipid molecules. The bubble is initiated in the tensed elastic state, its area being above the buckling area, $A_{\mathrm{buckling}} = n * a_{\mathrm{buckling}}$.

Dissolution of the gas in the surrounding liquid will 'deflate' the bubble and reduce its area towards a tension-less state (like the deflation of a rubber balloon), below which the bubble will buckle. In the tension-less state dissolution is much slower, since the capillary overpressure (typically an atmospheric pressure for micrometric bubbles) vanishes and the rate of radius decrease is proportional to inside pressure (which determines the dissolution concentration in the liquid according to Henry's law). Bubbles therefore *spontaneously tend to their buckling radius*, and then shrink much more slowly, compared to bubbles of constant surface tension. The reduction of surface tension is the main mechanism to account for increased longevity from the coating, since the gas permeability of 16 and 18-carbons phospholipids coatings is high (Borden and Longo, 2002).

Experiments show that asymmetric oscillations become more pronounced in the course of dissolution, see Fig 3.6. Our interpretation is that the bubble reaches the tension-less state, where buckling occurs. According to the present model, the asymmetry is the signature of the variation in surface tension during each cycle, and this variation is the highest near buckling.

The asymmetry can be monitored by the ratio $\Delta R^+/\Delta R^-$ of the positive and negative radius excursions (defined by $\Delta R^+ = \max(R) - R_0$ and $\Delta R^- = R_0 - \min(R)$, both materialized on Fig 3.5b). Simulations demonstrate indeed that the compression-

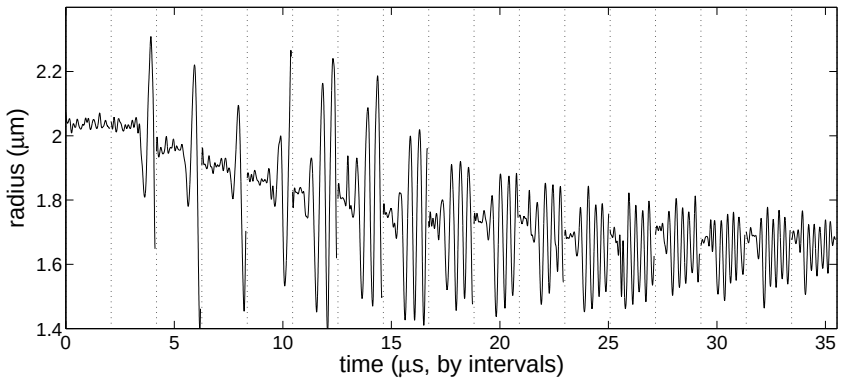

Figure 3.6: Experimental recordings of repeated acoustic pulses of 100 kPa on a single bubble, separated by 50 ms (break of time at vertical lines). The oscillation asymmetry increases pulse after pulse. (Frequency is increasing from 1.5 to 4 MHz, inducing amplitude changes).

only asymmetry ($\Delta R^+/\Delta R^- < 1$), is more pronounced when $R_0/R_{\rm buckling} \sim 1$ (see Fig 3.7), the tension asymmetry during the oscillation being maximal.

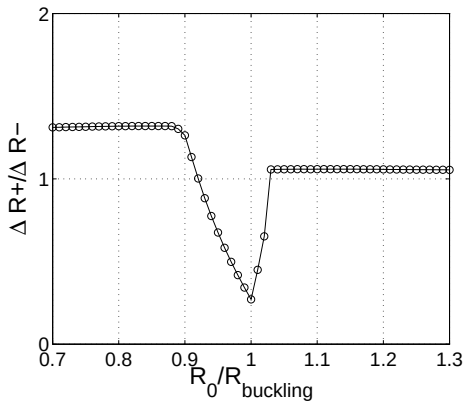

Figure 3.7: Simulated asymmetry of the oscillation for varying starting radii. Acoustic pulse and shell properties: same as Fig 3.5.

This behavior is to be contrasted with the large amplitude oscillation of bubbles with a constant surface tension, which tends to produce higher positive excursions. It is seen on the same figure when the bubble radius is well above $R_{\rm buckling}$ (free bubble state, $\sigma = \sigma_{\rm water}$) or well below $R_{\rm buckling}$ (tension-less state, $\sigma = 0$). The response curve slightly depends on frequency: varying the frequency between 1 and 4 MHz changes

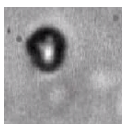

$\Delta R^+/\Delta R^-$ by about 10%.

Repeated pulses on a bubble accelerate the gas dissolution, as evidenced on Fig 3.6 by the sudden decrease after the first pulse and the subsequent pulses. Two mechanisms could account for this effect. First, the initial pulses may expel some lipid molecules and reduce the buckling radius, to which the bubble will relax. Another explanation would be an 'inverse' rectified-diffusion generated by compression-only behaviors. The gas pressure increases during the compression phase, while it remains close to the pressure at rest during expansion (a symmetric oscillation would alternately compress and expand the gas). The concentration of gas in the liquid near the interface being proportional to gas pressure (Henry's law), the asymmetry, even small, tends to force more gas out of the bubble. This 'inverted' rectified-diffusion would be the opposite of the usual rectified-diffusion effect that counteracts dissolution for free gas bubbles (Hilgenfeldt et al., 1996).

A quantitative evaluation of this effect follows from the expression of the rate of dissolution of an oscillating bubble (Fyrillas and Szeri, 1994; Hilgenfeldt et al., 1996)

$$\frac{d}{dt}\overline{R(t)} = \frac{Dc_0}{\rho_g \overline{R(t)}^2}\left(\frac{c_\infty}{c_0} - \frac{\overline{P_g(t)R(t)^4}}{P_0\overline{R(t)^4}}\right)\left(\int_0^\infty \frac{dh'}{(3h'+R(t)^3)^{4/3}}\right)^{-1}, \qquad (3.7)$$

where the overline is the average over one period, this equation being valid for an evolution slow at the scale of the period. The diffusivity of the gas is D, its volumic mass ρ_g, its saturation concentration c_0 and its concentration far from the bubble c_∞. The last factor containing an integration along the variable h' does not changes sign, and tends to R^4 for small amplitude oscillations. A compression-only signal produces a stronger 'averaged' pressure term $\overline{P_g(t)R(t)^4}/\overline{R(t)^4}$ (for instance it amounts to $1.2P_0$ from the simulation of Fig 3.5b), which accelerates dissolution. Even at at $R_{buckling}$, where the capillary overpressure vanishes, inverted rectified diffusion can force dissolution in a fully saturated liquid with $c_\infty/c_0 = 1$.

3.3.3 Rupture of the shell

The shell can withstand finite tensions only in its shell: starting from a compression-only signal and increasing the acoustic pressure step by step shows that a strong positive radius excursion suddenly appears above a critical pressure (see Fig 3.8a). In this new state, the bubble oscillates as a free bubble: we interpret this behaviour as the effect of the shell rupture.

To model the rupture, we assume that above a critical tension, $\sigma_{\mathrm{break-up}}$, the shell breaks up and that part of the bubble surface is uncovered. Once this threshold has been reached, the surface tension upper bound will be the surface tension of water, σ_{water}. We can therefore simulate the effect of an increasing acoustic pressure on a bubble (see Fig 3.8b).

The compression-only behavior ($\Delta R^+/\Delta R^- < 1$) is interrupted by the break-up of the shell: the non-linear behavior then favors positive excursions of the radius, as seen in experiment, as for standard large pressure Rayleigh-Plesset dynamics (see Fig 3.9).

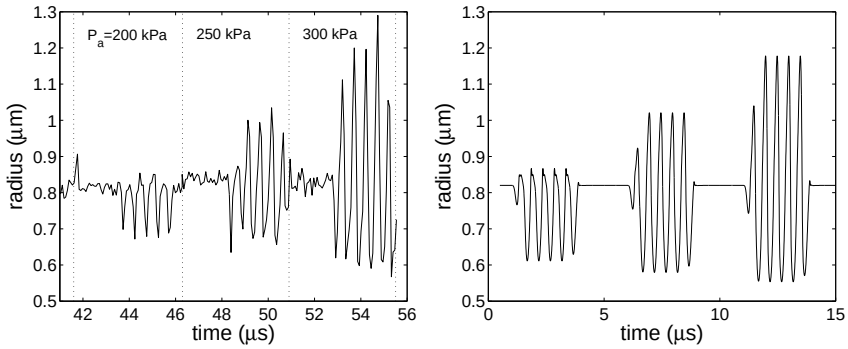

Figure 3.8: Left panel: Experimental recordings of a BR14 bubble response to repeated 2 MHz pulses separated by 60 ms, with an increasing acoustic pressure. Right panel: Simulation with the same acoustic pressures. The fitted shell parameters are $R_{\mathrm{buckling}} = R_0 = 0.82$ μm, $\chi = 1$ N/m, $\kappa_s = 7.2 \times 10^{-9}$ kg/s, while the critical break-up is $\sigma_{\mathrm{break-up}} = 0.13$ N/m.

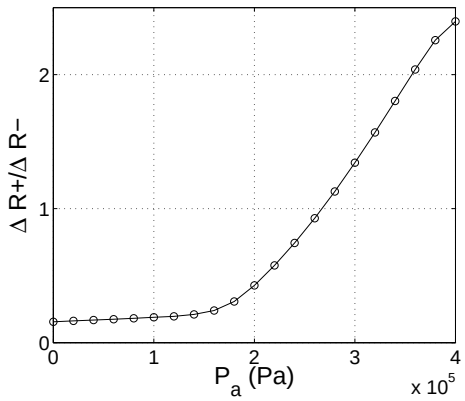

Figure 3.9: Simulated asymmetry of the oscillation for varying starting radii. Acoustic pulse and shell properties: same as Fig 3.8b.

3.4 Conclusions

We presented a simple model for the dynamical properties of coated contrast agents bubbles, with three parameters: a buckling surface radius, a shell compressibility and a break-up shell tension. It predicts a compression-only behavior of the bubble, a highly non-linear response. It occurs when its radius is close to the buckling radius, a state that naturally occurs with dissolution of gas, or that can be accelerated by repeated pulses. High-frequency image recordings with lipid coated microbubbles reveal the existence of

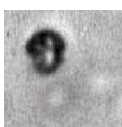

such asymmetric oscillations, and validate the model. The break-up of the shell is modeled by a third parameter, a finite tension of the bubble shell above which bare interfaces are created, with a corresponding change in bubble dynamics.

Possible applications of the model include: the characterization of coated microbubbles, the description of acoustic echoes and their use in non-linear or pulse-inversion imaging, and the prediction of the effect of repeated pulses or of long-term experiments.

Acknowledgements We would like to thank Joris Timmermans for his help in computations. We appreciated fruitful discussions with François Graner and Wouter den Otter.

3.5 Appendix: Comparison with the elasticity of a solid shell layer

Like monolayer coatings, the elasticity of a thin solid shell of thickness $\epsilon \ll R$ is characterized by a two-dimensional compression modulus $\chi = A\frac{d\sigma}{dA}$, where σ is the isotropic in-plane tension (shear of the surface does not occur with a radial expansion, and bending is neglected assuming an initial curvature close to the spontaneous curvature). Additionally, the solid shell has two interfaces, with a surface tension σ_1 for the inner interface and σ_2 for the outer interface. The mechanical equilibrium balance for any small change in bubble area around the tensionless shell area A_0 reads $\delta W = \chi(A/A_0 - 1)dA + \sigma_1 dA + \sigma_2 dA - (P_g - P_l)dV = 0$, from which we obtain the pressure jump at the liquid-gas interface $P_g - P_l = 2(\sigma_1 + \sigma_2 + \chi(A/A_0 - 1))/R$. The effective surface tension of the shell thus reads:

$$\sigma = \sigma_1 + \sigma_2 + \chi\left(\frac{R^2}{R_0^2} - 1\right), \tag{3.8}$$

it is a linear function of the bubble area, like in the lipid *monolayer* coated bubble model (Eq. (3.1) for the elastic state, with $\sigma(R_0) = \sigma_1 + \sigma_2$).

The model for a thick elastic shell by Church (1995) provides the same effective surface tension law when the shell thickness ϵ tends to be small compared to the radius. In this model the shell has a bulk shear modulus G_s and is incompressible in volume (the thickness thus varies around its equilibrium value during the oscillation). From the Church model at small thicknesses we find that the shell contribution can be expressed with an effective tension law as in Eq (3.8), using a 2D elastic modulus $\chi = 3G_s\epsilon$, which is a classical result of the elasticity of thin plates (**?**).

4

"Compression-only" behavior of phospholipid-coated contrast bubbles

Nico de Jong, Marcia Emmer, Chien Ting Chin, Ayache Bouakaz, Frits Mastik, Michel Versluis, and Detlef Lohse

Ultrasound in Medicine & Biology, 2007, 33(4):653-656

Abstract Ultrasound contrast agents oscillate approximately linearly up to a certain pressure range where nonlinearity sets in. Nonlinear microbubble oscillations are exploited in ultrasound pulse-echo imaging as this improves the contrast-to-tissue ratio. Here we report the observation of a highly nonlinear response of phospholipid-coated contrast agents at pressures as low as 50 kPa, termed "compression-only behavior", where the microbubbles only compress, yet hardly expand. Time-resolved bubble dynamics recorded through ultra high-speed imaging revealed that nearly 40% of the coated bubbles show compression-only behavior.

4.1 Introduction

Ultrasound contrast agents are small encapsulated microbubbles (mean diameter $\sim$3 μm) that are used to enhance the diagnostic quality of medical ultrasound images. Current imaging modalities for contrast agents, such as power modulation (Eckersley et al., 2005) and pulse inversion imaging (Burns et al., 2000), are based on nonlinear bubble responses. The nonlinear bubble response is used to discriminate between contrast agent and tissue. For small acoustic pressures, up to 20 kPa, the bubble response is predominantly linear (Hoff et al., 2000). At elevated pressures, nonlinear responses start to occur; the compression phase differs from the expansion phase. At acoustic pressures above $\sim$100 kPa, the nonlinearity increases, accompanied by changes in the bubble shape and dimension, resulting in bubble destruction in the extreme case.

The backscattered signal from a nonlinearly oscillating bubble contains not only the fundamental (transmitted) frequency, but also harmonic frequencies, at twice the fundamental frequency (second harmonic), or even higher multiples of the insonation frequency (third, fourth, etc.). This nonlinear scattering effect is not displayed by tissue and it therefore offers a possibility to separate the response of the bubble from that of surrounding tissue. Currently, mainly the second harmonic scattering of the bubbles is adopted in commercial diagnostic ultrasound machines. There are two main reasons for this. First, the second harmonic scattering from the bubbles is the most intense compared with higher harmonic scattering. Second, the frequency bandwidth of current imaging array transducers is in general limited to 70 to 80% of the center frequency and therefore does not allow operation of higher harmonic imaging (*e.g.*, at the third harmonic) without a substantial sacrifice of resolution and sensitivity. These factors have rendered the imaging of such higher harmonic frequencies alone almost inconceivable. Using higher harmonics, a new imaging technique termed "superharmonic imaging" has been proposed by Bouakaz et al. (2002), where selective imaging of higher harmonics showed improved image quality and contrast detection. Superharmonic imaging showed as much as 50 dB in contrast-to-tissue ratio.

The ultrasound imaging techniques proposed to date exploit nonlinear oscillations of contrast agent microbubbles as they promote the contrast-to-tissue ratio. Nonlinearity, however, sets in at relatively high acoustic pressures. Here, we report the observation of a highly nonlinear response of phospholipid-coated contrast agents at moderate acoustic pressure levels (as low as 50 kPa), termed "compression-only behavior", where the microbubbles only compress, yet hardly expand.

4.2 Materials and methods

SonoVue® (Bracco, Milan, Italy) or BR14 (Bracco Research SA, Geneva, Switzerland) contrast bubbles were prepared in the vial. Both types of bubbles present a phospholipid coating; SonoVue contains SF6 gas, while BR14 contains perfluorocarbon gas, which is even less soluble in water. The contrast bubbles were fed through a capillary fiber inside a small water-filled container (Fig 4.1). An Olympus microscope with a 60 high-

resolution water-immersed objective (NA = 0.9) and a 2× magnifier produced an image of the contrast bubbles. The image was then relayed to the high-speed framing camera Brandaris 128 (Chin et al., 2003). A focused broadband single-element transducer was mounted at 75 mm from the capillary. A Tektronix AWG 520 arbitrary waveform generator provided an ultrasound burst which was amplified by an ENI A-500 amplifier. The bubble response was investigated with an ultrasound burst of eight cycles at a frequency of 1, 1.8 or 4 MHz and pressures of 50, 100 or 200 kPa. The Brandaris camera was operated at a framing rate of 15 million frames per second, thereby resolving the insonified microbubble dynamics.

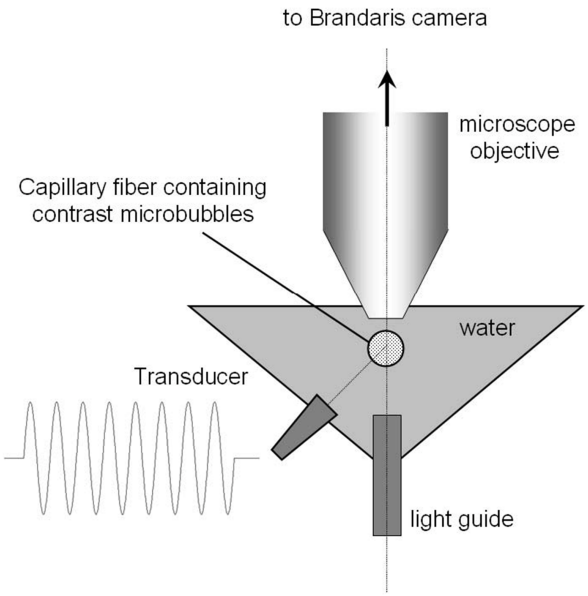

Figure 4.1: Schematic view of the experimental set-up.

A diameter-time curve is measured for each bubble using image analysis software developed in-house (van der Meer et al., 2007). The boundary detection algorithm for the diameter determination is based on a minimum-cost analysis (MCA) using the gray-scale slope along the radial direction as the cost function. The diameter of the bubble is defined as the diameter of a circle with an area equal to the area enclosed by the detected boundary. The diameter is then plotted against time to produce a diameter-time curve. From the diameter-time curve, the relative expansion E and the relative compression C of the bubble was deduced. E is defined as the absolute expansion (maximum diameter minus initial diameter) divided by the initial diameter. C is defined as the absolute compression (initial diameter minus minimum diameter) divided by the initial diameter.

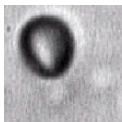

4.3 Results

A total of 101 observations of oscillating bubbles were recorded at an acoustic pressure covering the range of linear behavior (50 kPa), moderately nonlinear behavior (100 kPa) and for 200 kPa the start of bubble destruction. Figure 4.2 shows a typical example of a regular bubble (top panel) and a bubble showing compression-only behavior (bottom panel) insonified at a frequency of 1.8 MHz. The regular bubble has an initial diameter of 3.5 μm and shows a relative expansion amplitude E, which is equal to the relative compression amplitude C. The Fourier transform of the diameter-time curve shows a dominant peak at the insonifying frequency, while higher harmonics are below the noise level. In the bottom panel of Fig 4.2, the diameter-time curve is displayed for a 2.0 μm diameter bubble showing compression-only behavior. While the bubble is subjected to a symmetric sinusoidal ultrasound wave, it only compresses and hardly expands beyond its initial diameter. Furthermore, the shape of the diameter-time curve in the compression phase of the ultrasound shows sharp edges, very different from the regular bubble response, which is shown in the upper part of the figure. Accordingly, the Fourier transform of the diameter-time curves shows high second and even third harmonics, which are only 10 dB below the fundamental component.

From the relative expansion and compression of the bubble, E and C, respectively, the ratio E/C was calculated. Figure 4.3 shows the scatter plot for E/C as a function of the diameter for the three acoustic pressures (50, 100 and 200 kPa) and for the three frequencies (1, 1.8 and 4 MHz). This results in nine subplots containing the 101 observed bubbles. The value of E/C for bubbles vibrating symmetrically will be close to unity. For bubbles displaying compression-only behavior, the value of E/C will be close to zero. In the scatter plot, the data points with an $E/C < 0.5$ are labeled compression-only bubbles and are indicated with filled circles. The open circles are used for bubbles with an $E/C > 0.5$. Although the data set is sparse for some cases, *e.g.*, only two bubbles in Fig 4.3d, it can be concluded that compression-only behavior can be observed for pressures as low as 50 kPa. Furthermore, all bubbles in our data set with a diameter smaller than 4 μm show compression-only behavior at 1 MHz driving frequency. Of the total set of 101 bubbles, $\sim$40% showed compression-only behavior.

We also include a numerical simulation of E/C as a function of the bubble diameter. The bubbles were subjected to the same burst as in the experiment with the same frequencies and acoustic pressures. E and C were determined from the synthetic diameter-time curves, which were calculated from the elastic shell model of de Jong et al. (1994). The shell parameters for this model were taken from the available experimental data on bulk SonoVue as presented by Gorce et al. (2000), assuming a surface tension σ of 0.07 N/m, a shell stiffness of S_p = 1.1 N/m and a shell friction of $S_f = 0.27 \times 10^{-6}$ kg/s. By comparing the experimental data with the simulations, it follows that compression-only behavior must be explained by a more sophisticated shell model, possibly including shell buckling and rupture (Marmottant et al., 2005).

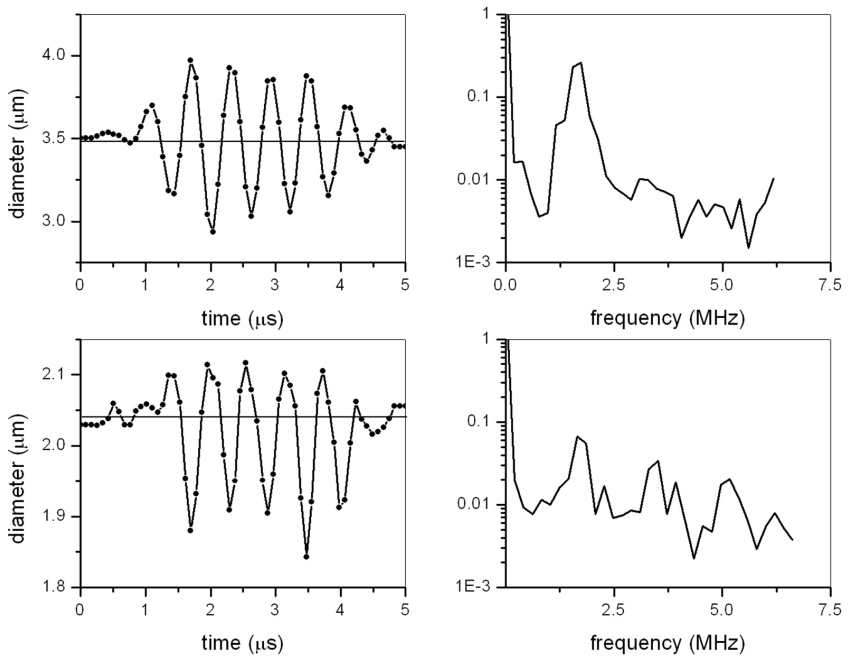

Figure 4.2: Top: regular oscillation behavior of a coated microbubble of 3.5 μm in diameter. The bubble was insonified with a gated six-cycle sine-wave burst at 1.8 MHz center frequency at a pressure of 100 kPa. Left panel: the diameter-time curve produced from optical high-speed imaging data. Right panel: the power spectrum of the diameter-time curve. Bottom: compression-only behavior of a coated microbubble of 2.0 μm. The bubble was insonified with a gated six-cycle sine-wave burst at 1.8 MHz center frequency at a pressure of 100 kPa. Left panel: diameter-time curve produced from optical high-speed imaging data. Right panel: the power spectrum of the diameter-time curve.

4.4 Discussion and conclusion

The compression-only behavior of phospholipid-coated bubbles was discovered in the course of an optical ultra high-speed contrast imaging study on individual SonoVue and BR14 bubbles and was analyzed retrospectively. Acoustically, such a bubble behavior will prove difficult to detect. First, acoustic studies on the behavior of single microbubbles are difficult to perform. Moreover, because the resolution of ultrasound is much lower than the bubble diameter, multiple bubbles will be sampled simultaneously and acoustically it will be very difficult to discriminate the compression-only behavior from a nonlinear vibration. From the optical analysis, it was found that 40% of the bubbles showed compression-only behavior. It is to be expected that samples with a much higher

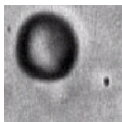

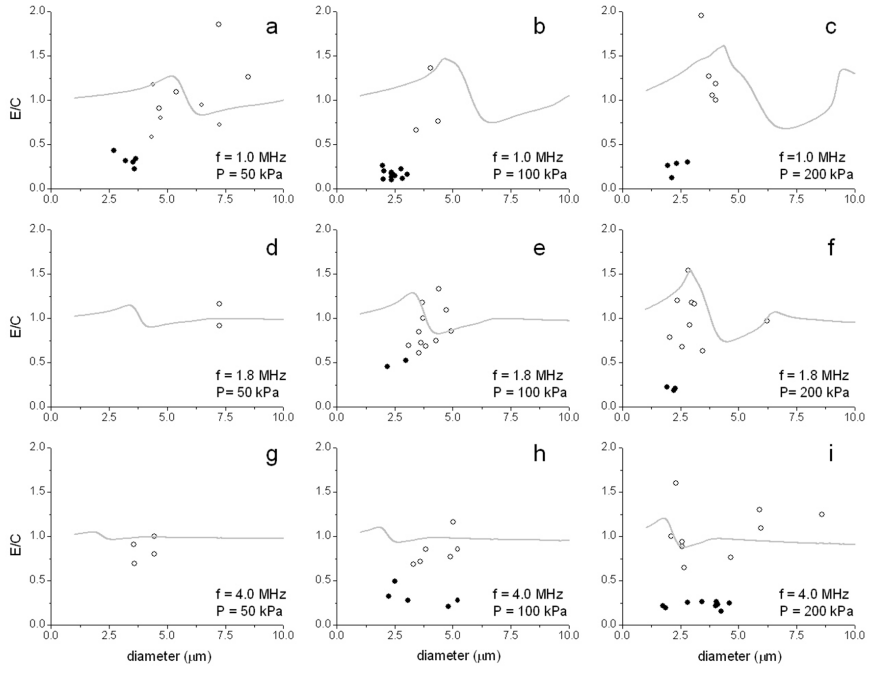

Figure 4.3: Expansion over compression, termed E/C, as a function of the bubble diameter for three frequencies (1, 1.8 and 4 MHz) and at three acoustic pressures (50, 100 or 200 kPa). Filled circles: bubbles showing compression-only behavior with $E/C < 0.5$. Open circles: bubbles with $E/C > 0.5$. Solid line: numerical calculation of E/C as a function of bubble diameter. The simulation was performed using the elastic shell model by de Jong et al. (1994). The shell parameters were derived from bulk SonoVue bubbles as characterized by Gorce et al. (2000).

fraction of compression-only bubbles can be achieved, if well-defined preparation conditions are met. For example, it is speculated that a small shrinkage of the bubble after preparation will induce compression-only behavior. One of the possible explanations for the bubble's behavior is the buckling of the phospholipid shell (Marmottant et al., 2005). Shell buckling will prevail if gas diffuses from the core into the liquid, thereby suppressing bubble expansion in the rarefaction phase. Therefore, in addition to the parameters controlled in this study, *i.e.*, frequency and acoustic pressure, the time elapsed after preparation of the agent, which was typically between a few minutes or as long as one day (in a clinical setting, the contrast agent should be administered within 6 h after preparation), may contribute significantly to an enhanced compression-only effect.

The compression-only behavior is highly nonlinear and has been observed at acoustic pressures as low as 50 kPa. Current methods for contrast imaging are all based on the

nonlinear behavior of the bubbles, as it results in the optimal contrast-to-tissue ratio. Future research should reveal the increase in sensitivity using coated bubbles displaying the compression-only behavior and detection methods such as pulse inversion (Burns et al., 2000) and radial modulation imaging (Bouakaz et al., 2007).

Acknowledgements We thank Peter Frinking and Marcel Arditi of Bracco Research Geneva for supplying SonoVue and BR14 vials and for their helpful comments and suggestions. We also thank Sander van der Meer and Benjamin Dollet for supplying additional experimental data and for performing numerical simulations. We appreciate the skillful technical assistance of Leo Bekkering, Cees Pakvis, Wim van Alphen and Gert-Wim Bruggert.

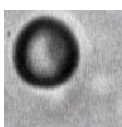

5

The onset of microbubble vibration

Marcia Emmer, Annemieke van Wamel, David E. Goertz, and Nico de Jong

Ultrasound in Medicine & Biology, 2007, 33(6):941-949

Abstract A linear relationship between the relative expansion of an off-resonance ultrasound contrast microbubble and low acoustic pressures is expected. In this study, high-speed optical recordings of individual phospholipid-coated microbubbles were used to investigate this relationship for microbubbles ranging from 2 to 11 μm and for acoustic pressures ranging from 20 to 250 kPa at a driving frequency of 1.7 MHz. For microbubbles larger than 5 μm, the relative expansion ($\Delta D/D_0$) increased linearly with applied acoustic pressure, starting at the origin. The response of smaller microbubbles (< 5 μm) also increased linearly with the applied acoustic pressure. However, linearity started at an acoustic pressure threshold value of 30 to 120 kPa for the different individual microbubbles. Below these pressure values, little or no oscillation was observed. The results may be explained by size-dependent mechanical properties of the phospholipid shells. An imaging technique such as power modulation imaging could profit from the presence of an acoustic pressure threshold in the microbubble response.

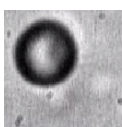

5.1 Introduction

Ultrasound (US) contrast agents consist of small (1-10 μm diameter) encapsulated gas-filled microbubbles. In an ultrasound field, microbubbles oscillate due to the compressibility of their gas core. This oscillating behavior is the primary source of the high scattering strength of these agents, which make them well suited to provide contrast enhancement in diagnostic US imaging.

Models like the RPNNP equation (Leighton, 1994) are well established for gas microbubbles. However, although a number of models have been developed for encapsulated microbubbles, their ability to predict acoustic behavior has only been shown to be valid under limited circumstances. Further, the shell parameters required as input for these models have generally been achieved with bulk acoustic property measurements. In Gorce et al. (2000), for example, the shell is characterized by two parameters, the stiffness and the viscosity, using attenuation and scattering measurements from suspensions of microbubbles. As a result, such measurements may not be valid for predicting the behavior of each individual microbubble with its specific size and thickness, composition and packing of the phospholipid layer. Optical measurements also have been used to estimate shell properties, but under high amplitude (acoustic peak negative pressure $>$100 kPa) transmit conditions (Morgan et al., 2000).

Contemporary contrast imaging methods are based on exploiting differences between tissue echoes and the unique acoustical signatures of microbubbles (de Jong et al., 2002). For hard-shelled microbubbles, the principle of gas-release detection is used. The destruction mechanism of a hard-shelled polymer/albumin microbubble filled with nitrogen gas has been revealed by high-speed optical recordings (Bouakaz et al., 2005). When the applied acoustic pressure is higher than the threshold, the gas escapes from the shell and forms free gas bubbles. These gas bubbles produce distinct echo signals, which can be used to detect the contrast agent (Bouakaz et al., 2005; Frinking et al., 2001; Sboros et al., 2002).

Other microbubble imaging methods are typically used for soft-shelled contrast agents, which are more elastic than hard-shelled contrast agents. Soft-shelled microbubbles also fragment at high acoustic pressures (Chomas et al., 2001; Postema et al., 2004), but, unlike hard-shelled microbubbles, they are already strong US scatterers at lower acoustic pressures. Multipulse detection methods at low mechanical index (Deng and Lizzi, 2002; Eckersley et al., 2005) use the difference between the signatures of tissue and these microbubbles by preferentially detecting the nonlinear microbubble echoes and by canceling the background tissue signals.

Although encapsulated microbubbles are believed to respond differently under different driving-pressure amplitudes, few studies have been performed to study the pressure-dependence of their response in detail. Studies on the acoustic response have demonstrated that the pressure amplitude of the first harmonic is proportional to the incident peak pressure, whereas the second harmonic and third harmonic amplitudes are shown to be proportional to the square and cube of the incident peak pressure, respectively (Church, 1995; Shi et al., 1999). Furthermore, the attenuation by encapsulated microbub-

bles in US propagation appeared to be dependent on the acoustic pressure (Chen et al., 2002; Tang et al., 2005). Optical studies have found that maximal bubble expansion increases for larger microbubbles (Postema et al., 2003).

In this study, we investigated the onset of phospholipid-coated microbubble vibration. For encapsulated microbubbles, the well-known Blake model does not apply (Leighton, 1994). It is generally believed that in the small oscillation amplitude limit, an encapsulated microbubble behaves as a forced linear oscillator. This hypothesis implies that any input acoustic pressure on a resting microbubble results in a vibration, which increases proportional to an increasing acoustic pressure. However, this has never been investigated. High-speed optical recordings of individual microbubbles for specific resting microbubble sizes revealed a nonlinear relationship between radial excursion and low acoustic driving pressure. In this study, the results were compared with the outcome of theoretical descriptions and discussed in detail.

5.2 Materials and methods

5.2.1 Theory

The onset of microbubble vibration was investigated using the model by Church (1995) for encapsulated microbubbles. It concerns air microbubbles enclosed in a solid, incompressible viscoelastic shell, described by a shear modulus G_s and a shear viscosity μ_s. It is assumed that the shell reduces the surface tension both at the shell-liquid and the shell-gas interfaces. As a result, the surface tension can be neglected. The shells of the investigated microbubbles consist of a lipid monolayer, which has a thickness of approximately 3 nm (Kim et al., 2003). We therefore assume a thin shell (Hoff et al., 2000), which results in the following equation of motion,

$$\begin{aligned}\rho_l(R\ddot{R}+\frac{3}{2}\dot{R}^2) &= p_0(\frac{R_0}{R})^{3\kappa}-\frac{4\mu_l\dot{R}}{R}-p_0-P_{ac}(t)\\ &\quad -12\mu_s\frac{d_{s,0}R_0^2}{R^3}\frac{\dot{R}}{R}-12G_s\frac{d_{s,0}R_0^2}{R^3}(1-\frac{R_0}{R})\end{aligned} \tag{5.1}$$

where R is the microbubble radius, ρ_l is the density of the surrounding liquid, *i.e.* water, R_0 is the radius at equilibrium, p_0 is the hydrostatic liquid pressure outside the microbubble, $P_{ac}(t)$ is the acoustic pressure, $d_{s,0}$ is the shell thickness, and the dots denote differentiation with respect to time. For the shell parameters, $G_s = 60$ MPa and for $\mu_s = 1.2$ Pa s were taken, values compatible with those estimated experimentally for SonoVue® in Gorce et al. (2000). Solving Eq (5.1) results in the radius or diameter of the microbubble as a function of time as a response on the applied acoustic pressure.

To study the microbubble excursion as a function of acoustic pressure, the diameter-time curves (DT curves) of an encapsulated microbubble 3.0 μm in diameter were calculated. For comparison, the DT curves of a free gas microbubble 3.0 μm in diameter also were calculated using the RPNNP equation (Leighton, 1994). Bursts of 50 cycles

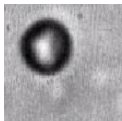

with a peak pressure ranging from 0.1 to 100 kPa were applied at a center frequency of 1.7 MHz. After the transient response, D_{max}-D_{min} (ΔD) normalized to the resting diameter (D_0) was determined as a function of the applied driving pressure $P_{ac}(t)$.

The equations of motion are highly nonlinear, as one would expect from a system where expansion cannot be symmetric with compression except at low driving pressures. Therefore ΔD was chosen to express microbubble excursion instead of D_{max} or D_{min}. To compare the linearity of the DT curves between theoretical predictions and experimental results, the same parameters used in the previous calculation were applied to calculate the responses of 1- to 9 μm in diameter encapsulated microbubbles on 50 cycle-bursts with a frequency of 1.7 MHz and a peak pressure of 220 kPa. From the resulting DT curves, the ratio between microbubble expansion E and compression C was determined, which was expressed by $E/C = |(D_{max} - D_0)/(D_{min} - D_0)|$.

5.2.2 Experiment

The experimental phospholipid-coated contrast agent used was BR14 (Bracco Research SA, Geneva, Switzerland). The microbubbles were injected into a cellulose Cuprophan® capillary tube (Akzo Nobel Faser AG, Germany) 160 μm in inner diameter and 200 μm in outer diameter, which is smaller than the acoustic wavelength. Hydrophone measurements were performed to verify its acoustic transparency.

The capillary tube was placed in a water tank in the focal area of the transducer at 7.5 cm. The water tank was positioned under a customized BXFM microscope (Olympus Nederland B.V., Zoeterwoude, the Netherlands) with 2× U-CA magnification and a LUMPlanFl 100× water immersion objective lens (Olympus). No reflections from the objective were observed. Under the capillary tube, an optic fiber (Olympus) was mounted and was connected with the illumination source, which was an MVS-7010 Fiber Optic Strobe (PerkinElmer Optoelectronics, Salem, MA). Images of individual microbubbles were recorded with the Brandaris 128 fast-framing camera system (Chin et al., 2003).

A v397-SU 2.25-MHz single element transducer (Panametrics Inc., Waltham, MA, USA) was mounted in the water tank at an angle of 45° relative to the top of the tank. Its aperture was 35 mm and the -6 dB beam diameter at focus was 5 mm. The transducer was connected to an arbitrary waveform generator (Tabor Electronics Ltd., Tel Hanan, Israel) and a 60 dB linear power amplifier (AR Worldwide, Souderton, PA, USA). The amplitude was adjusted with two variable attenuators (Agilent Technologies, Inc., Palo Alto, CA, USA).

The pressure values were calibrated using a 0.2 mm PVDF probe hydrophone (Precision Acoustics Ltd., Dorchester, UK). For the transducer, previous studies have verified that the acoustic pressure was constant over a 200 μm distance in both axial and transversal direction, which corresponded with the diameter of the capillary tube (Bouakaz et al., 2005).

Individual microbubbles were recorded in 12 sequences of 64 image frames at a speed of 13 million frames per second, corresponding to 12×5 μs optical scanning duration. The time between the sequences was 50 ms. In each sequence, a single microbubble was

insonified with a gated six-cycle-sine wave burst at 1.7 MHz center frequency, giving a US exposure time of 3.5 μs. The remaining 1.5 μs was used to record the microbubbles before US exposure, so that the resting microbubble size could be determined. The peak negative pressure was increased in subsequent sequences from 20 to 250 kPa. In a second experiment, we insonified single microbubbles with a Gaussian apodised burst with FWHM duration of 3.0 μs, a peak pressure of 250 kPa and a center frequency of 1.7 MHz.

Single microbubbles that were in focus of the microscope (Postema et al., 2003) were selected. The diameters of the individual microbubbles were measured in each image frame with a semiautomatic procedure using a minimal cost algorithm in custom software, written in a Matlab environment (Mathworks Inc, Natick, MA, USA) resulting in the microbubble diameter response as a function of time. To increase the accuracy of the determination of the minima and maxima, the DT data was interpolated at 20 times the original frame rate and filtered with a lowpass finite impulse response (FIR) filter. As a measure of the microbubble response, the difference between the maximum and the minimum diameter, D_{max} - D_{min} (ΔD) normalized to the resting diameter (D_0), was taken.

The relationship between $\Delta D/D_0$ and the acoustic driving pressure, $P_{ac}(t)$, was investigated. For this purpose, the linearity of the $\Delta D/D_0$ vs. P_{ac} curves was established by fitting least-squares trend lines through the linear portions of $\Delta D/D_0 - P_{ac}$ and determining the intercepts with the pressure axis. The significance of the linear regression was investigated by calculating the square of the correlation coefficient (R^2) for $\Delta D/D_0$ vs. P_{ac} and subsequently testing the hypothesis that the slope of the trend line is zero. Only ΔD larger than the resolution limit of our system and responses smaller than 30 % of the initial size ($\Delta D/D_0 < 0.3$) were used, so that we could assume that the response was linear. The trend lines were based on at least three sample points.

To compare the experimentally obtained DT curves with the outcome of the simulations, also from the measured DT responses, the E/C values were determined at an acoustic driving pressure of 220 kPa. The application of a Gaussian apodised burst was used to illustrate the shape of the DT curve at the onset of microbubble oscillation.

Chin et al. (2003) have shown that at 120$\times$ magnification, the Brandaris 128 high-speed camera system resolves lines with 0.4 μm spacing. For this study, the stochastic error in the microbubble diameter measurements had to be established, because it determined the resolution limit of microbubble vibration. The stochastic error depends on a combination of the point-spread function of the optical system including the CCD grid, the CCD electronics and the minimum cost algorithm that was used to measure the microbubble area. For our system, the stochastic error was established by determining the maximum diameter variation, ΔD, for each microbubble in the first sequence of image frames, *i.e.* when no US was applied. Subsequently, the maximum ΔD for the whole population was determined and this value was taken as the resolution limit of microbubble vibration.

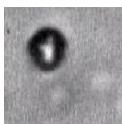

5.3 Results

5.3.1 Theory

Both the free gas microbubble and the encapsulated microbubble of 3.0 μm diameter were driven at 1.7 MHz. This is below resonance for both cases, because the linear resonance diameter for a free gas microbubble is 3.7 μm in diameter and an encapsulated is 6.2 μm in diameter. At low driving pressures, Fig 5.1 shows that for both the free and the encapsulated microbubble, the amplitudes of oscillation increase linearly with the applied acoustic pressure. Figure 5.1 also makes clear that this linear relationship starts at the origin.

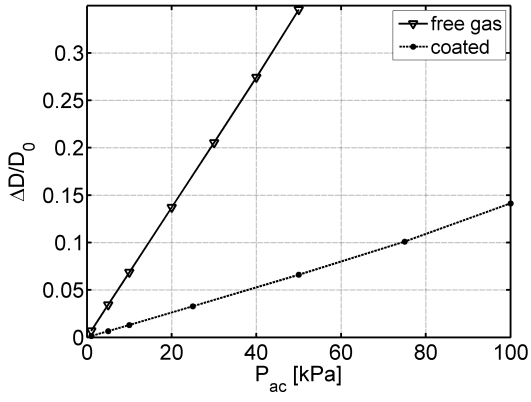

Figure 5.1: Simulations of the responses of a gas microbubble and an encapsulated microbubble, both 3.0 μm in diameter, to different US driving pressures.

The numerical solutions gave highly nonlinear free microbubble oscillation motions above 50 kPa. For higher pressures, ΔD was demonstrated to not be a good measure of free microbubble oscillation. Also, for the encapsulated microbubble, acoustic pressures above 100 kPa resulted in a nonlinear response. As an example, Fig 5.2a shows the DT curve of an encapsulated microbubble 3.0 μm in diameter at a driving pressure of 220 kPa. The expansion amplitude ($D_{max} - D_0 = 1.0$ μm) is higher than the compression amplitude ($D_0 - D_{min} = 0.56$ μm), resulting in an E/C value of 1.8. Figure 5.2b shows the E/C values of encapsulated microbubbles ranging from 1- to 9 μm in diameter. The E/C values vary with microbubble size from 1.1 to 2.3, which shows that the expansion phases dominated the compression phases.

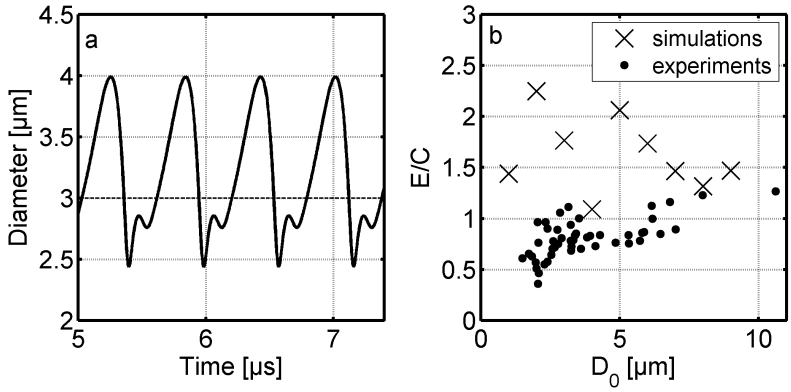

Figure 5.2: a) Simulated DT response of a 3.0 μm encapsulated microbubble, b) E/C values as a function of microbubble resting diameter of simulated encapsulated microbubble responses, and measured encapsulated microbubble responses, with $E/C = |(D_{max} - D_0)/(Dmin - D_0)|$.

5.3.2 Experiment

To investigate the onset of microbubble oscillation, the results of 48 single microbubbles were analyzed. The smallest microbubble was 1.3 μm in diameter and the largest microbubble was 10.6 μm in diameter. The majority of the microbubbles (73%) was smaller than 4.0 μm in diameter.

First, the resolution limit of microbubble vibration was determined. For all measurements, the diameter variation when no US was applied was in the range of 66 to 150 nm with a mean of 100 nm and a standard deviation of 23 nm. One pixel in the image frame is 100 nm, and so the variation is approximately one pixel. The worst case of 150 nm diameter variation was taken as the resolution limit of microbubble vibration.

Fig 5.3a shows image frames of a 4.2 μm-diameter microbubble, which was insonified with an acoustic pressure of 250 kPa. The resulting DT curve is shown in Fig 5.3b. In the first 13 frames the microbubble is at rest. Starting at frame 14, the microbubble is first compressed, and then reaches its maximum and minimum diameter of 5.4 and 2.6 μm, respectively, within six cycles.

The DT curves for the complete range of applied acoustic pressures are shown in Fig 5.4, which also includes the responses of three additional microbubbles of different sizes. The DT curves demonstrate a relationship between resting diameter and the response. Larger microbubbles expand and compress more than smaller microbubbles, as was also demonstrated by Postema et al. (2003).

We noticed that the acoustic pressure at which the first microbubble vibration could be observed, decreased with resting diameter. Furthermore, it was interesting to compare the responses of the two largest microbubbles. The maximal difference between maximal

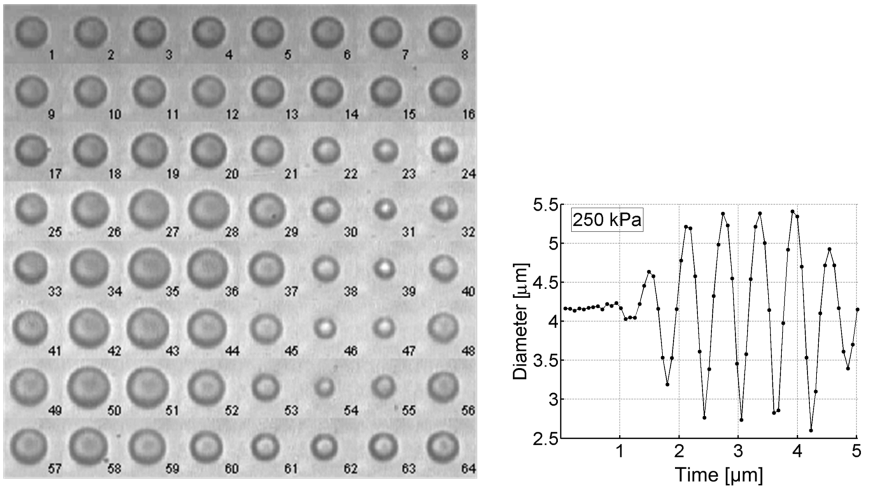

Figure 5.3: a) Sequence of 64 image frames of a 4.2 μm diameter microbubble, driven by a 6-cycle-US burst with a peak negative pressure of 250 kPa; b) Diameter-time response.

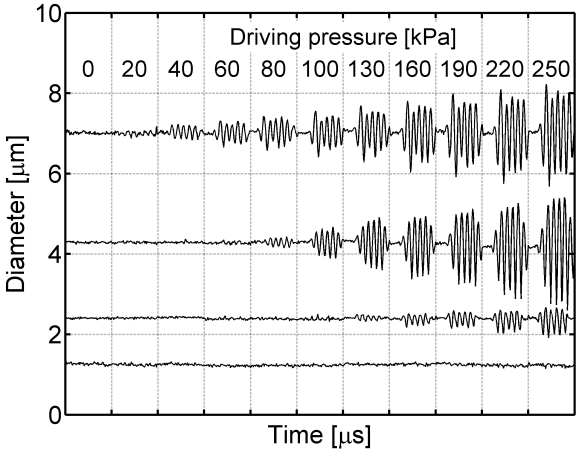

Figure 5.4: Diameter-time responses of four microbubbles with a resting diameter of 1.3, 2.4, 4.2 and 7.0 μm. Vertical grid lines separate the sequences, and the applied driving pressure is indicated.

and minimal diameter (ΔD) for the microbubble 7.0 μm in diameter was 2.6 μm, which results in $\Delta D/D_0 \approx 0.4$. This is less than $\Delta D/D_0 \approx 0.7$ for the 4.2 μm diameter microbubble. However, the first oscillations of the 7.0 μm microbubble were observed when the driving pressure was at its lowest value of 20 kPa, which differed from the observed response of the smaller microbubble. In that case, oscillations were not detected until the driving pressure was increased up to 60 kPa. Although the microbubble 4.2 μm in diameter showed a stronger response, a higher acoustic driving pressure was needed to initiate oscillations.

The microbubble excursion ($\Delta D/D_0$) as a function of the driving pressure $P_{ac}(t)$ was investigated for the complete dataset of 48 microbubbles (Fig 5.5). The microbubbles were categorized according to their resting diameters. Two microbubbles with diameters of 1.3 and 2.0 μm had no detectable oscillations. The responses showed a relationship between microbubble excursion and the applied acoustic driving pressure. In most cases, a higher acoustic pressure resulted in an increased excursion. For some microbubble sizes however, this did not hold for the lowest applied acoustic pressures. For microbubbles smaller than 5 μm diameter, the $\Delta D/D_0$ vs. P_{ac} curves did not start to rise at the origin, but at higher acoustic pressures.

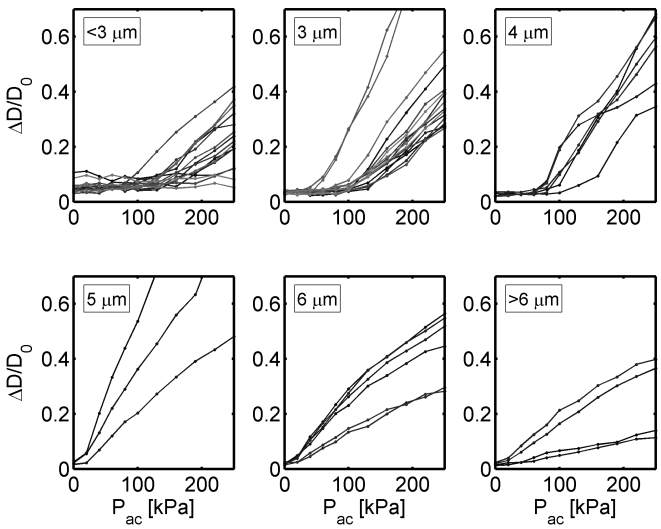

Figure 5.5: Microbubble excursions as a function of acoustic pressure. The responses of the different microbubbles have been categorized according to their sizes, as indicated.

The $\Delta D/D_0$ vs. P_{ac} curves of 38 microbubbles answered to the conditions posed for trend line fitting. Eleven lines were based on three measurements of $\Delta D/D_0$ vs. P_{ac}, 14 were based on four measurements and 13 on more than four measurements. The

average of the R^2 values of these trend lines was 0.98 with a standard deviation of 0.025. Testing the significance of the trend line slopes resulted in an average p-value of 0.03 with a standard deviation of 0.05, 80% of these p-values was lower than 0.025.

From these trend lines the pressure-axis intercepts were determined (Fig. 5.6). Microbubbles ranging from 2.0 to 4.0 μm had a pressure-axis intercept between 30 and 120 kPa. Microbubbles larger than 5.0 μm had a pressure-axis intercept approximating 0 kPa, ranging from -7 kPa to 7 kPa. In addition, the linearity of the DT curves was measured at an acoustic pressure of 220 kPa. Figure 5.2b shows that the E/C values of the measurements were between 0.4 and 1.25.

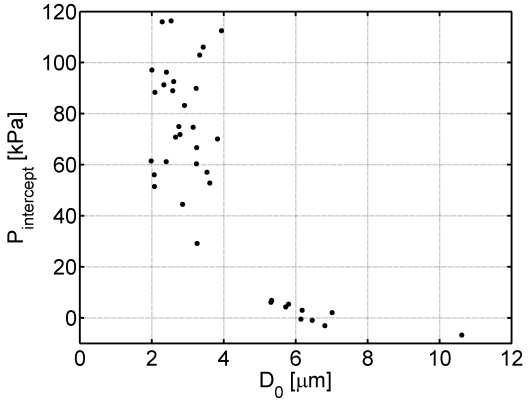

Figure 5.6: The intercepts with the pressure axis of the linear part of the microbubble responses as a function of resting diameter.

The onset of microbubble vibration was illustrated by the application of a Gaussian apodised burst. The DT curves of three microbubbles that were 1.5, 2.1 and 7.7 μm in diameter, respectively, are shown in Fig 5.7. After a transient time of approximately one cycle, the microbubble 7.7 μm in diameter responded with a phase shift of approximately half a cycle, which indicated that it was excited above resonance. The smaller microbubbles responded in phase with the applied US field, but they required a higher acoustic driving pressure before their oscillations became apparent, an observation consistent with the observations demonstrated in Figs 5.4 and 5.5. The shape of these DT curves was also notable. The response of the 7.7-μm microbubble had a nearly symmetrical shape: expansion approximated compression, E/C = 0.8. The microbubble that was 2.1 μm in diameter had an E/C of 0.7. However, the DT curve of the 1.5-μm microbubble was highly nonlinear. Approximately six frames cover the expansion phase of the microbubble and only three frames cover the compression phase of the microbubble. At a frame rate of 13 million frames per second, the expansion phase was 0.46 μs and the compression phase 0.23 μs. In less time, the negative amplitude ($D_0 - D_{min}$) was maximal 0.3 μm and the postive amplitude ($D_{max} - D_0$) was maximal 0.15 μm, which

resulted in an E/C value of 0.5. This microbubble was more compressed than expanded. Furthermore, the shape of the compression phase was much sharper than is generally expected in sinusoidal responses.

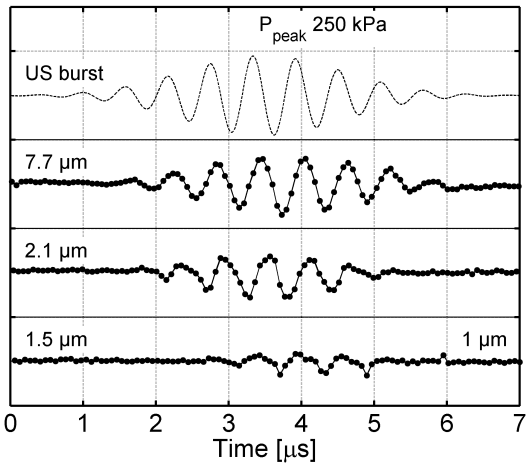

Figure 5.7: DT curves of microbubbles with a resting diameter of 1.5, 2.1, and 7.7 μm. The horizontal grid lines represent 1 μm. The dashed line (US burst) shows the applied Gaussian apodised US burst with a peak pressure of 250 kPa.

5.4 Discussion and conclusions

The theory predicted for both a free and encapsulated microbubble that were 3.0 μm in diameter, a linear response for acoustic pressures below 50 and 100 kPa, respectively (Fig 5.1). However, measured responses of microbubbles that were 3.0 μm in diameter showed clearly different behavior (Fig 5.5). The acoustic pressure needed to increase above a threshold value before the microbubble responses increased linearly with the applied acoustic pressure. Trend lines were fitted through the linear portions of the $\Delta D/D_0$ vs. P_{ac} curves. Although statistics on these trend lines was limited by the low number of available sample points for each fit, we concluded that the lines could be used to determine the pressure axis intercepts and so obtain estimations of the threshold values of the onset of linear oscillation as a function of acoustic pressure. From Figs 5.5 and 5.6, it appears that microbubbles with a resting diameter smaller than 5 μm show threshold behavior, and larger microbubbles do not show this behavior.

Because the observation of the microbubble response was limited by the system resolution of 150 nm, it is not known if the microbubbles oscillated at acoustic pressures below the acoustic pressure threshold. Furthermore, microbubbles larger than 5 μm may

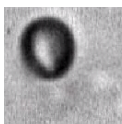

also have an acoustic pressure threshold lower than 20 kPa, but this was not investigated. We noticed that in Fig 5.6 the threshold values did not have a clear relationship with resting diameter. This might be due to differences in composition of the encapsulated microbubbles, or, in some cases, to the low number of sample points. However, we have shown for encapsulated microbubbles with a size smaller than 5 μm diameter that at the onset of microbubble vibration, the response as a function of acoustic pressure was non-linear. This is not predicted by theoretical descriptions of encapsulated bubble behavior. The encapsulated microbubble response increased proportional to the acoustic pressure applied above an acoustic pressure threshold.

In addition to the observed threshold behavior, we found a second indication that current models do not fully describe encapsulated microbubble behavior, which is the difference in the shape of the microbubble response itself. Figure 5.2b illustrates that at an acoustic pressure of 220 kPa, measured E/C values differed greatly from predicted values. When simulations predicted dominant expansion, $E/C > 1$, measured values showed more compression up to symmetrical shapes, $E/C < 1$.

The pressure threshold for microbubble oscillation is a new observation, and the precise mechanism is currently not known. One explanation is that a force threshold must be overcome before substantial oscillations can occur. For simplicity, it has been assumed that microbubble oscillation contains an expansion phase. The microbubble is considered to be a sphere comprised of two hemispheres that need to separate at the equator, see Fig 5.8. We then assume that the microbubble can only expand in the negative phase of insonation when the shell breaks along the interface between the two hemispheres. The force required to overcome the tensile strength (σ) of the phospholipid shell is $\sigma \cdot 2\pi R \cdot h$. The force made available by the insonating field to overcome this force is $p(t) \cdot \pi R^2$. Therefore, an estimate of the acoustic pressure required to split the two hemispheres is $p = \sigma \cdot 2\pi R \cdot h / \pi R^2 = 2\sigma h / R$. From this relation, it appears that the acoustic pressure threshold is inversely proportional to the microbubble radius, and so relatively more force is necessary for the vibration of small microbubbles.

The value of the tensile strength of the phospholipid monolayer is not known. We therefore assume a value of 10 MPa, which is the tensile strength of polyethylene (Nakamura et al., 2005). For a microbubble of 1.0 μm diameter and a shell thickness of 3 nm, we found that the acoustic pressure threshold $p(t)$ for the onset of microbubble vibration is 60 kPa. This is in the same order of magnitude as the experimentally obtained threshold values.

In reality, it is unlikely that the microbubble cracks into two perfect hemispheres, as it is unlikely that the coatings are completely homogeneous. Borden et al. (2004) have found that microbubbles may form domains that are in the condensed phase separated by boundaries, which are in the expanded phase. The size and distribution of the domains depend on the types of lipids used and the processing conditions and influence microstructure and mechanical properties of the microbubbles (Kim et al., 2003). Also shrinkage may lead to differences between the mechanical properties of shells. Any finite interfacial tension leads to a Laplace pressure that drives gas out of the microbubble even in saturated solution (Duncan and Needham, 2004). As the gas leaves, compression of

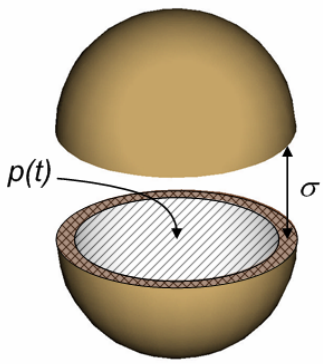

Figure 5.8: In a simplified perception of microbubble expansion, the microbubble is a globe with two hemispheres that need to separate at the equator. The acoustic pressure p(t) acts on the cross-section of the microbubble πR^2, as the tensile strength acts on the shell area $2\pi Rh$.

the monolayer shell leads to tight packing of the condensed phase (Kim et al., 2003). As a consequence of the described influences, smaller microbubbles may have a higher tensile strength than larger microbubbles, which increases their acoustic pressure threshold for the onset of microbubble vibration.

Another indication for the influence of the phospholipid packing on microbubble behavior is the observation of asymmetric diameter response curves, which has earlier been described as "compression-only" behavior (Marmottant et al., 2005) and is defined as $E/C < 0.5$ (de Jong et al., 2007). The high Van der Waals forces in the tightly packed monolayer inhibit both expansion and compression of the microbubble. However, when the pressure is increased enough, the monolayer can fracture and break, lose material or buckle and fold (Lipp et al., 1998). In the latter case, the microbubble is more easily compressed, which explains the dominant negative radial excursions. We observed "compression-only" behavior in the responses obtained after applying the Gaussian apodised burst (Fig 5.7), but it was also noticed when the US bursts with constant amplitude were used (Fig 5.2b). Figure 5.2b demonstrates that "compression-only" behavior, like threshold behavior, may be related to resting microbubble size. Moreover, it was especially noticed at the onset of microbubble vibration. Therefore in addition, the DT curve shapes were determined during the first microbubble vibrations observed. The E/C values were classified as $E/C < 0.5$ ("compression-only") or $E/C > 0.5$ ("symmetrical") (see Table 5.1). Table 5.1 shows that "compression-only" behavior may be dependent on size; only microbubbles smaller than 4 μm show this typical asymmetric radial shape, whereas microbubbles larger than 4 μm started oscillating in a (more) symmetrical form.

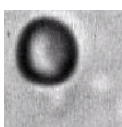

Table 5.1: Shape of the DT curve at the onset of microbubble vibration, classified as $E/C \leq 0.5$ ("compression-only") or $E/C > 0.5$ ("symmetrical").

Microbubble size (μm)	1-1.9	2-2.9	3-3.9	4-4.9	5-5.9	6-6.9	>7
Compression-only							
number(% of total)	2(100)	10(59)	3(25)	0(0)	0(0)	0(0)	0(0)
Total observed, number	2	17	12	2	6	4	3

Another influence on microbubble behavior may be the capillary tube in which the microbubbles were inserted. Buoyancy drives the microbubbles towards the tube wall. Previous studies have for example shown a constrained microbubble activity in a tube 12 μm in diameter (Caskey et al., 2005), and asymmetric oscillations of a targeted microbubble (Zhao et al., 2005). The influence of the presence of a rigid wall on the onset of microbubble vibration, however, has yet to be established.

The presence of an acoustic pressure threshold will have implications for the acoustic microbubble responses. For a linear system, the attenuation by the microbubbles in US propagation is independent of the insonifying acoustic pressure. However, previous studies (Tang et al., 2005) have shown a linear relationship between the attenuation of phospholipid microbubbles and the insonating acoustic pressure for acoustic pressures down to 20 kPa. The presence of an acoustic pressure threshold may explain these results. Below this threshold, only the largest microbubbles oscillate significantly and contribute to the attenuation. As the acoustic pressure is increased, the smaller microbubbles also will contribute and increase the attenuation.

The results in our study reveal the complex nature of the onset of phospholipid contrast agent vibration. For microbubbles smaller than 5 μm in diameter, the acoustic pressure needed to increase above 30 to 120 kPa before their responses increased linearly with the applied acoustic pressure. Possible explanations are size-dependent mechanical properties of the phospholipid shells. More research will lead to a better understanding of microbubble oscillation, which could be exploited to enhance the contrast between tissue and microbubbles in imaging techniques. A technique such as power modulation imaging (Deng and Lizzi, 2002) could especially profit from the presence of such a pressure offset in the microbubble response. However, further research is needed to fully use these specific characteristics of microbubble behavior.

Acknowledgements We thank Alexander Klibanov (University of Virginia) and Marcel Böhmer (Philips Research) for their interest and fruitful discussions. This work is part of the research programme of the 'Stichting voor Fundamenteel Onderzoek der Materie (FOM)', which is financially supported by the 'Nederlandse Organisatie voor Wetenschappelijk Onderzoek (NWO)'. We acknowledge Bracco Research, Geneva for supplying the contrast agent BR14.

6

Pressure-dependent attenuation and scattering of phospholipid-coated microbubbles at low acoustic pressures

Marcia Emmer, Hendrik J. Vos, David E. Goertz, Annemieke van Wamel,
Michel Versluis, and Nico de Jong

Ultrasound in Medicine & Biology, 2008, In Press

Abstract Previous optical studies have shown threshold behavior of single contrast agent microbubbles. Below the acoustic pressure threshold, phospholipid-coated microbubbles with sizes < 5.0 μm in diameter oscillate significantly less than above the threshold pressure. Previous studies also revealed an acoustic pressure-dependent attenuation of ultrasound by microbubble contrast agents. In this study, we investigated whether pressure-dependent acoustic behavior may be explained by threshold behavior. For this purpose, pressure-dependent attenuation and scattering of a phospholipid-coated contrast agent were measured. Transmit frequencies between 1.5 and 6.0 MHz and acoustic pressures between 5 and 200 kPa were applied. Unlike the galactose-based contrast agent Levovist, the phospholipid-coated contrast agent BR14 showed a pressure-dependent attenuation. In addition, it was found that filtered suspensions with only microbubbles < 3.0

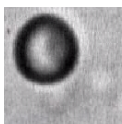

μm in diameter show more pressure-dependent attenuation behavior than native suspensions of phospholipid-coated microbubbles. For the scattering measurements conducted at 3.0 MHz, the native suspension did not show any pressure-dependent behavior. However, the filtered suspension responded highly nonlinearly. Between 30 and 150 kPa, 16 dB additional scattered power was obtained. We concluded that threshold behavior of phospholipid-coated microbubbles results in pressure-dependent attenuation and scattering.

6.1 Introduction

Ultrasound contrast agents consist of a suspension of encapsulated gas-filled microbubbles with sizes ranging from 1-10 μm in diameter. The large difference in acoustic impedance between the gas in the microbubble and the surrounding tissue *in vivo* makes microbubbles highly reflective, which is useful to enhance the acoustic backscattering from blood. In addition, they can act as harmonic oscillators, which greatly increases backscattered energy. Moreover, depending on the acoustic pressure applied, the backscattered energy contains higher harmonics, which is useful to discriminate the microbubbles from tissue that scatters in an approximately linear manner.

An example of an imaging technique sensitive to nonlinear responses is power modulation imaging (Brock-Fisher et al., 1996). This technique operates by sending two pulses into the body, equal in shape, but with different amplitude, *e.g.* full and half amplitude. On receive, based on the scaling property of linearity, echoes from the half-amplitude-transmitted pulse are adjusted in amplitude and subsequently subtracted from the full-amplitude echoes. This procedure removes most of the linear responses at the fundamental frequency, and the remaining echoes contain mainly nonlinear signals from the microbubbles. This imaging technique is particularly developed for the second harmonic responses of the microbubbles. Studies of the microbubble response to ultrasound have demonstrated that the pressure amplitude of the scattered fundamental is proportional to the incident peak pressure, whereas the second harmonic amplitude is proportional to the square of the incident peak pressure (Church, 1995; Shi and Forsberg, 2000). These findings were obtained in the weak nonlinear regime and may not be valid at strong nonlinearities such as microbubble destruction. Recent studies by de Jong et al. (2007) and Emmer et al. (2007a,b,c) have shown that also in the weak nonlinear regime, strong nonlinear microbubble responses can be observed, which offers new opportunities for imaging.

In addition to the scattering behavior of the encapsulated microbubbles, their acoustical behavior is also characterized by the acoustic energy that they absorb. The scattered and absorbed energy in combination determine the attenuation by the microbubbles of the incident ultrasound wave. Ultrasound traveling through tissue is attenuated proportional to its incident intensity and propagation distance (Duck, 1990). For low acoustic pressures, the attenuation by tissue is independent of the incident intensity. For encapsulated microbubbles, however, recent studies have shown acoustic pressure-dependent attenuation (Casciaro et al., 2007; Chatterjee et al., 2005; Chen et al., 2002; Tang et al.,

2005; Tang and Eckersley, 2007). The general explanation is, as expressed by Chen et al. (2002), that at high pressure amplitudes, a greater proportion of energy of the fundamental is lost because of harmonic generation, damping or even microbubble destruction.

In our previous paper, the onset of oscillation of insonified individual phospholipid-coated microbubbles was studied (Emmer et al., 2007b). At a transmission frequency of 1.7 MHz, high-speed optical recordings revealed a threshold in the response of microbubbles < 5.0 μm in diameter, which is not predicted by current theoretical descriptions of microbubble behavior. At low acoustic pressures and off-resonance, theory predicts an approximately linear relationship between the microbubble vibration amplitude and the incident acoustic pressure. However, it was observed that the microbubbles oscillated significantly less below an acoustic pressure threshold, which ranged from 30 up to 120 kPa for individual microbubbles. Above this threshold, their response was proportional to the acoustic pressure applied. Although a good correlation was not found, threshold behavior seems inversely related to microbubble size. These observations may be explained by size-dependent mechanical properties of the phospholipid shells, such as differences in the phospholipid packing and the occurrence of condensed phase domains (Emmer et al., 2007b). It may also be a consequence of the mechanical properties of phospholipid-coatings, resulting in a dynamic surface tension (Marmottant et al., 2005) and/or rheological thinning behavior (van der Meer et al., 2007).

The optically observed threshold behavior of phospholipid-coated microbubbles implies that their acoustic response should also exhibit a threshold behavior. We hypothesize that such threshold behavior will contribute to both pressure-dependent attenuation and scattering. In the present study, the pressure-dependence of the attenuation of a phospholipid-coated contrast agent was investigated and compared to that of a galactose-based contrast agent. Second, the influence of microbubble size on the pressure-dependence of both attenuation and scattering was investigated. The responses of filtered suspensions with only microbubble sizes smaller than 3.0 μm in diameter were compared to that of unfiltered (native) phospholipid-coated contrast agent suspensions. Since a microbubble size of 3.0 μm is well below the maximal diameter at which threshold behavior was optically observed (5.0 μm), threshold behavior is expected to be more pronounced, resulting in relatively more pressure-dependent attenuation and scattering.

6.2 Materials and methods

6.2.1 Attenuation measurements

The attenuation as a function of acoustic pressure was measured in a transmission setup (Fig 6.1a). In this setup, two pairs of unfocused single-element transducers were used. The first pair had center frequencies of 2.25 MHz and an aperture diameter of 13 mm (transmit: V306, receive: A306, Panametrics-NDT, Olympus NDT Inc., Waltham, MA, USA). The second pair had center frequencies of 5.0 MHz, transmit aperture diameter 7 mm (V310, Panametrics-NDT) and receiving aperture diameter 13 mm (V309, Panametrics-NDT). Pulses were produced with a programmable waveform generator

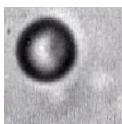

(8026, Tabor Electronics Ltd., Tel Hanan, Israel). The amplitude was adjusted and amplified by a pair of variable attenuators (355C/D VHF, Agilent Technologies, Inc., Palo Alto, CA, USA) and a 60 dB linear power amplifier (A-500, ENI, Rochester, NY, USA). The transducers were mounted in a water bath in which a smaller microbubble container filled with Isoton II (Beckman Coulter, Inc., Fullerton, CA, USA) was placed. One night before the experiments were performed, the water bath and beakers were filled with water and Isoton II respectively, to obtain air saturated liquids at room temperature. The microbubble container was made of Perspex with windows on three sides, which were covered with acoustically transparent Mylar. Its length was 5 cm. The Mylar membrane facing the transmitting transducer was oriented at 80 degrees with respect to the beam axis. In the microbubble container, a magnetic stirrer kept the suspension uniform. Received signals were low-pass filtered (10.7 MHz, Mini-Circuits, Brooklyn, NY, USA) and recorded on a digital oscilloscope (9400, LeCroy, Chestnut Ridge, NY, USA). For further analysis, the recorded data was transferred to a personal computer.

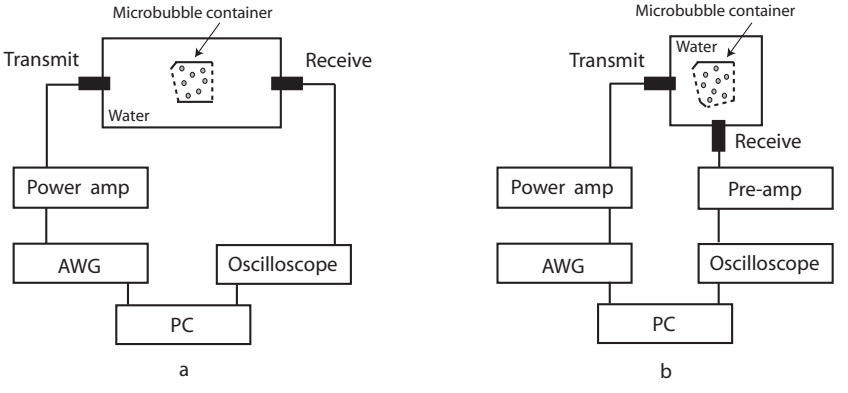

Figure 6.1: Schemes of the experimental setups used; a) attenuation measurements, b) scattering measurements. The arbitrary waveform generator (AWG) connected to the power amplifier (Power amp) generated the transmit-pulses, which were received, (amplified in set-up b) and recorded by the oscilloscope and PC.

To measure the attenuation as a function of the acoustic pressure, cosine-tapered 8-cycle bursts with peak negative pressures from 5 to 200 kPa were applied. The acoustic pressure was increased and subsequently decreased to verify the influence of preceding bursts. A repetition rate of 2 Hz for the consecutive bursts ensured that the microbubbles were mixed well after insonation and that the preceding burst did not affect the next measurement.

The transmission set-up was used for two experiments. First, at a transmit frequency of 3.0 MHz, the attenuation as a function of the acoustic pressure of BR14 was compared to that of Levovist (Schering AG, Berlin, Germany). BR14 is a phospholipid-coated

microbubble filled with decafluorobutane (Bracco Research SA, Geneva, Switzerland). It was prepared by adding 5 ml 0.9% NaCl (Baxter S.A., Lessines, Belgium) to the vial and shaking it for 30 sec. Levovist consists of galactose particles, with a trace amount of palmitic acid as a stabilizer. It was prepared by adding 8 ml sterile water to 4 g of granules and shaking for 10 sec. At room temperature, BR14 was directly injected into the microbubble container at a concentration of 130 μl/l and Levovist at a concentration of 4.4 ml/l. For each contrast agent, three samples were tested, giving a total of six measurements at each acoustic pressure.

Second, the attenuation as a function of the acoustic pressure of a native BR14 suspension (concentration of 130 μl/l) was compared to that of a filtered BR14 suspension. Filtering was done by diluting 500 μl of BR14 in 400 ml Isoton II and mechanically filtering by gravity drainage through a porous polycarbonate membrane with 3.0 μm pore size (GE Osmonics Inc., Minnetonka, MN, USA). To measure also for the filtered suspensions a significant attenuation, the concentration of the filtered suspensions was a factor of 7.9 higher than the concentration of the native suspension. From previous studies, it is known that attenuation is linearly dependent on concentration (de Jong et al., 1992) and although the size distributions are not identical, we assume that the measured attenuation values can be corrected for this concentration difference (*i.e.* filtered attenuation values are divided by 7.9).

The 2.25 MHz transducers were used at frequencies from 1.5-3.0 MHz (step size of 0.25 MHz) and the 5.0 MHz transducers at 3.0 to 6.0 MHz (step size of 0.5 MHz). The series of frequencies was repeated on three different samples, which resulted in six measurements for each acoustic pressure at each frequency. Measurements started and ended at 3.0 MHz to verify that the suspension did not change while stepping through the different frequencies. For each sample of microbubbles, a series of measurements took 4 minutes. Attenuation as a function of acoustic pressure was determined at the transmit frequency by subtracting the average measured spectrum prior to injection of the agent from the spectrum obtained after injection. The six measurements per frequency and acoustic pressure were averaged and the standard deviations were determined.

The contrast agent size distributions were measured with a Multisizer III (Beckman Coulter, Inc.) using a 20-μm aperture. With this aperture size, microbubble sizes between 0.45 and 12 μm diameter could be measured. To test the effect of mechanical filtering, native BR14 at a concentration of 5 ml/l was counted before and after filtering. Before filtration, the concentration of the vial before dilution was 8.4×10^8 microbubbles per ml. 96% of the microbubbles had a diameter < 3.0 μm. The number weighted mean microbubble diameter was 1.0 μm. After filtration, 21% of the microbubbles was removed, including all microbubbles larger than 3.0 μm in diameter. This resulted in a number weighted mean diameter of 0.81 μm. As has also been demonstrated for other contrast agents like Definity (Goertz et al., 2007) and Albunex (de Jong and Hoff, 1993), the mechanical filtration of BR14 appeared to be effective.

In an additional experiment, the occurrence of microbubble destruction during the attenuation measurements was investigated. At a transmit frequency of 3.0 MHz and a repetition rate of 10 kHz, the attenuation experiment was repeated. This repetition rate

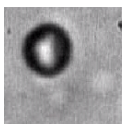

and switching off the magnetic stirrer during the measurements prevented the entrance of fresh microbubbles in the region of insonification. For each acoustic pressure, 2000 traces were recorded with a digitizer (DP235, Acqiris, Agilent Technologies SA, Geneva, Switzerland).

To verify the frequency-dependence of the attenuation, we measured this independently from the previous measurements in a pulse-echo setup. Four transducers were mounted on one side of the water tank. All transducers had a focal distance of 75 mm and were focused on the back wall of the microbubble container, which was used as a reflector. The transducers had center frequencies of 1.0 (V302), 2.25 (V305), 5.0 (V308) and 10.0 MHz (V311) (Panametrics-NDT) and were driven by an arbitrary waveform generator (33250A, Agilent Technologies, Inc., Palo Alto, CA, USA) and 60-dB power amplifier (A-500, ENI, Rochester, NY, USA). Single-cycle sine waves with the center frequency of each transducer and an acoustic pressure of 50 kPa were transmitted. The attenuation was determined for the -10 dB frequency band of each transducer, which was 0.52-1.25 MHz, 0.85-2.96 MHz, 2.14-6.53 MHz, and 4.21-12.4 MHz, for the 1.0, 2.25, 5.0, and 10.0 MHz transducer, respectively.

6.2.2 Scattering measurements

Scattering from both native and filtered BR14 suspensions as a function of acoustic pressure was measured. To verify the influence of the acoustic pressure, scattering from the contrast agents were compared to that of solid particles. These particles were assumed to have linear scattering characteristics. Figure 6.1b shows the setup used. A 2.25-MHz single-element transducer focused at 75 mm with an aperture of 35 mm diameter (V397, Panametrics-NDT) was used as a transmitter. At 3.0 MHz, the -6 dB beam width was 1.9 mm. The transmitting transducer was positioned at a right angle to the receiving transducer (745A1002, Vermon S.A. Tours, France), which was focused at 50 mm, had an aperture diameter of 25 mm, and a -6 dB beam width of 1.4 mm at 3.0 MHz. At a center frequency of 2.25 MHz, the -6 dB bandwidth of the Vermon transducer was 100%. Both transducers were focused on the middle of the microbubble container. Received signals were low-pass filtered (10.7 MHz, Mini-Circuits), 6 dB attenuated (Mini-Circuits) (not used with the linear scatterers) and amplified by a 58-dB amplifier (AU-3A-0110, Miteq Inc., Hauppage, NY, USA).

To measure the pressure-dependent scattering, cosine-gated 16-cycle bursts at a transmit frequency of 3.0 MHz were applied. Six samples were measured for each type of suspension. The peak negative pressure was alternately increased from 5-150 kPa and decreased from 150-5 kPa to verify the influence of preceding bursts. This resulted in a total of 12 measurements for each sample at each acoustic pressure. For each measurement, 30 sequences of scattered signals were recorded at a repetition rate of 2 Hz. Averaged spectra of these 30 data sequences were calculated within a 2 μs window around the acoustic focus, after the application of a Hanning window. Noise-only acquisitions were made with the transmit transducer covered. The microbubble scattering was calculated as the average power in a 0.1-MHz band centered around the transmit frequency. The

acoustic pressure was calibrated using a 0.2-mm PVDF needle hydrophone (Precision Acoustics Ltd., Dorchester, UK).

The concentration of the native BR14 suspension was 9 μl/l. The filtered suspension was prepared as described for the attenuation measurements, but at a concentration of 40 μl BR14 diluted in 400 ml of Isoton II. The solid particle suspension was prepared following a procedure similar to that described in Ramnarine et al. (1998). It was made of 5 μm-diameter Orgasol polyamide particles (2001USNAT1, Orgasol^{TM}, Elf Autochem, Paris, France) at a concentration of 1% by weight.

6.3 Results

6.3.1 Attenuation measurements

Figure 6.2 shows the results from the pulse-echo measurements, in which the frequency dependence of the attenuation by BR14 was measured. A maximum attenuation of 1.6 dB/cm at a frequency of 1.6 MHz was measured. This frequency is an indication of the resonance frequency of native BR14 suspensions.

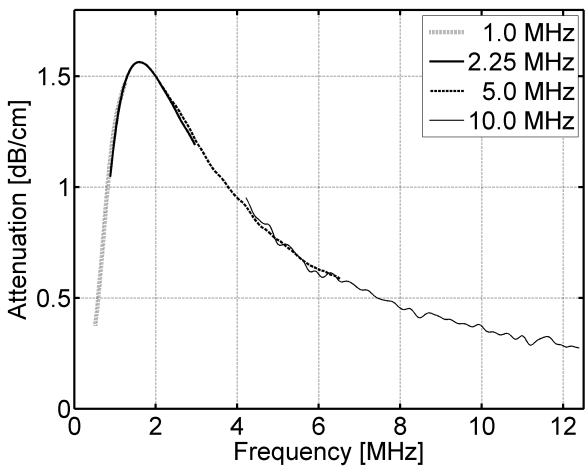

Figure 6.2: The attenuation of a native BR14 suspension as a function of the transmitted frequency, measured in a pulse-echo set-up. Four transmitting transducers were used (center frequencies indicated).

Figure 6.3 shows the attenuation as a function of the acoustic pressure of BR14 and Levovist at a transmit frequency of 3.0 MHz. The average attenuation over six measurements is depicted. The attenuation of Levovist was approximately constant and had a value of 0.46 dB/cm, which was unlike the attenuation of the BR14 suspension. For

acoustic pressures between 10 and 120 kPa, the attenuation of BR14 increased from 0.70 dB/cm to 1.0 dB/cm. Above 120 kPa, it was approximately constant. For comparison, the attenuation of soft tissue is shown, which is approximately 1.5 dB/cm at a transmit frequency of 3.0 MHz (Duck, 1990).

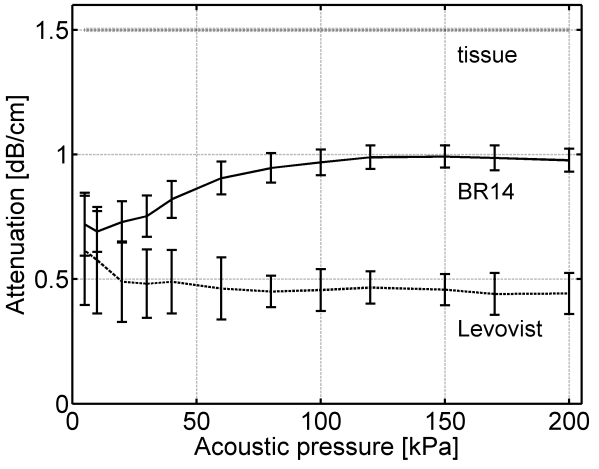

Figure 6.3: At a transmit frequency of 3.0 MHz, the average attenuation of BR14 and Levovist as a function of acoustic pressure. The bars indicate the standard deviations over six measurements. The attenuation of soft tissue is indicated (Duck, 1990).

Figure 6.4 shows the attenuation of a filtered BR14 suspension compared to that of a native BR14 suspension. The attenuation was measured at transmit frequencies between 1.5 and 6.0 MHz. Four examples at 1.5, 3.0, 4.5, and 6.0 MHz are shown. For the filtered suspensions, least attenuation was observed at 1.5 MHz, namely 0.02 dB/cm. Increasing the transmit frequency resulted in more attenuation. At 6.0 MHz and 200 kPa, the attenuation was 0.26 dB/cm. More important is the observation of pressure-dependent attenuation. At all transmit frequencies, except 1.5 MHz, the attenuation was not constant for the acoustic pressures used. For example at 3.0 MHz from 5-200 kPa, the attenuation increased by a factor of 3.3 from 0.04 to 0.13 dB/cm and also at 6.0 MHz, an increase by a factor of 3.3 was observed from 0.08 to 0.26 dB/cm. For the native suspension, most attenuation was observed at a transmit frequency of 1.5 MHz, which agrees well with Fig 2 (the next transmit frequency was 1.75 MHz, which is further from the maximum measured at 1.6 MHz in Fig 2). Whereas most pressure-dependent attenuation was observed near 6.0 MHz for the filtered suspension, most pressure-dependence for the native suspension was observed near 1.5 MHz. From 5 to 200 kPa, the attenuation increased by factors of 1.7, 1.4, and 1.3 at transmit frequencies of 1.5, 3.0, and 6.0 MHz, respectively.

The increase of attenuation with acoustic pressure is subject of further investigation.

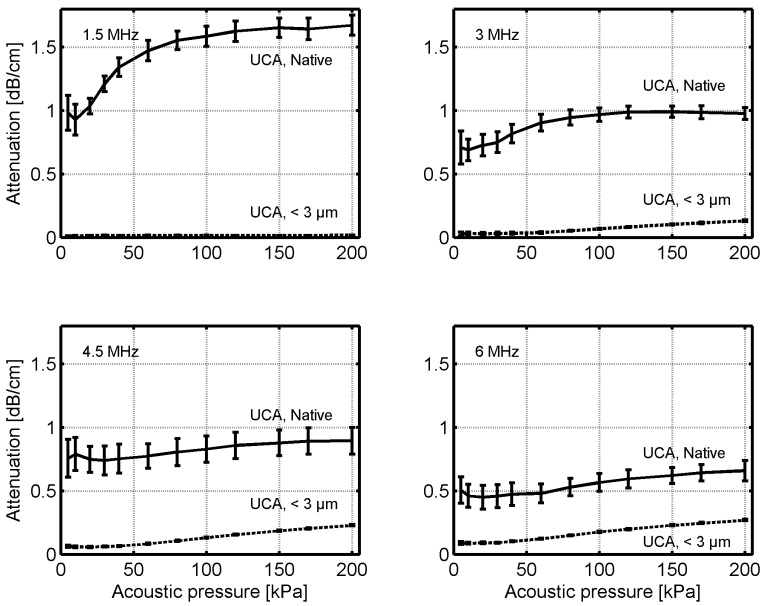

Figure 6.4: Four examples of the average attenuation of a native BR14 suspension (UCA, Native) and a filtered suspension (UCA, < 3 μm) as a function of the acoustic pressure. The bars indicate the standard deviations.

Figure 6.5 shows the ratio of attenuations (ROA) measured at 20 and 150 kPa as a function of the frequency transmitted. The attenuation measured at 20 kPa was divided by the attenuation measured at 150 kPa and subsequently multiplied with 100%. Thus a ROA of 100% means that there was no increase in attenuation when the acoustic pressure was increased from 20 to 150 kPa. For the native suspension, below 3.0 MHz, the ROA was approximately 60%. At 4.0 MHz, the ROA was the highest: 90%. For the filtered suspension, the ROA values below 3.0 MHz were less relevant, because at these transmit frequencies the attenuation was very low. Above 3.0 MHz, however, ROA values of approximately 30% were observed.

In an additional experiment, possible microbubble destruction was investigated. At 3.0 MHz, 2000 traces at a repetition rate of 10 kHz were recorded. Using a least squares fit, the trend line over the 2000 traces was calculated. From this trend line, the percentage reduction from the first to the last value was calculated, which is an indication for the percentage of microbubbles that were destroyed during the 2000 insonifications. Figure 6.6 shows that for both suspensions, the percentage of destroyed microbubbles is small. Maximum destruction was measured for the native suspension. At an acoustic pressure

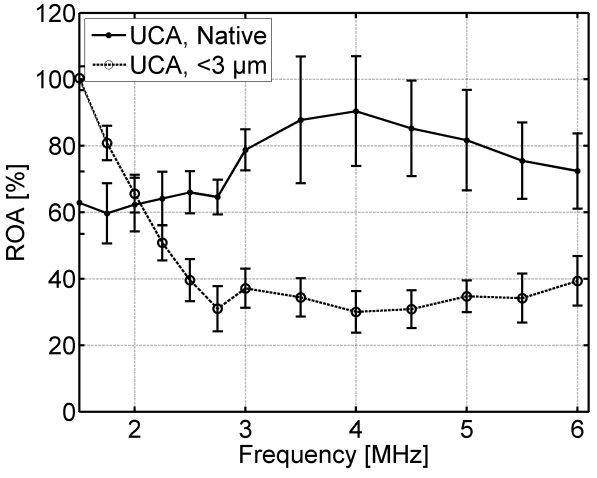

Figure 6.5: Ratio of attenuations (ROA) measured at 20 and 150 kPa for the native BR14 suspensions (UCA, Native) and the filtered suspensions (UCA, < 3 μm) as a function of transmit frequency.

of 200 kPa, the attenuation of the ultrasound beam was decreased by 3.4% after 2000 insonifications.

6.3.2 Scattering measurements

The scattered powers of native and filtered BR14 and solid particles suspensions as a function of the acoustic pressure were measured at a 3.0 MHz transmit frequency. At three acoustic pressures, Fig 6.7 shows examples of received radiofrequency (RF) signals and the accompanying power spectra. The top panels of Fig 6.7 show at 5 kPa and the fundamental scattered frequency, for the linear scatterers a signal-to-noise ratio (SNR) of 8.6 dB. An increase of 30 dB transmitted power (from 5 to 150 kPa) resulted in an increase of 30 dB scattered power at the fundamental frequency. From this we concluded that the linear scatterers indeed showed linear scattering behavior. For the native suspension, we also observed a linear response at the fundamental frequency. For an increase of 30 dB transmitted power, the SNR increased 29 dB from 23-52 dB. For the filtered suspension, however, different behavior was observed. In this case, the SNR at the fundamental frequency increased more than 30 dB. From 5-150 kPa, the SNR increased 42 dB from 9.5-51 dB.

For each measurement, the scattered power at the fundamental frequency was normalized to the transmitted power (the acoustic pressure squared). For a linear relationship between scattered power and transmitted power, a constant value is expected. Subsequently, the measurements were averaged for each transmitted power and standard de-

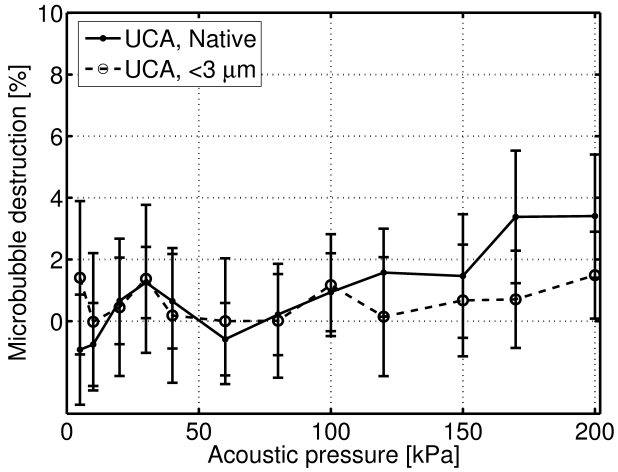

Figure 6.6: Microbubble destruction of the native BR14 suspension (UCA, Native) and the filtered suspension (UCA, < 3 μm) as a function of the acoustic pressure.

viations were calculated. Figure 6.8 shows the results. As a reference value (0 dB), the normalized scattered powers measured at 20 kPa were taken. The responses of the linear scatterers and native contrast agent do not deviate much from 0 dB, indicating that their responses were proportional to the acoustic pressure. Up to an acoustic pressure of 30 kPa, the normalized scattered power of the filtered suspension does also not deviate from 0 dB. Between 30 and 150 kPa however, the response increased 16 dB. At these acoustic pressures, the scattered power of the filtered microbubbles increased more than the acoustic pressure was increased.

6.4 Discussion and Conclusions

Attenuation from the galactose-based contrast agent Levovist was compared to that of the phospholipid-coated contrast agent BR14. For Levovist compared with BR14, no pressure-dependent behavior was observed (Fig 6.3). The attenuation of BR14 increased until the acoustic pressure was 120 kPa, indicating that below 120 kPa, the microbubbles were not fully active. Below 120 kPa, it is possible that only a subpopulation of the microbubbles oscillated and absorbed acoustic energy. Another possibility is that the microbubbles oscillated significantly less than at higher acoustic pressures or a combination of both. It is however shown that the dissipation of acoustic energy by the microbubbles was not proportional to the acoustic pressure transmitted.

Second, the influence of microbubble size on the pressure-dependence of the attenu-

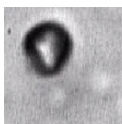

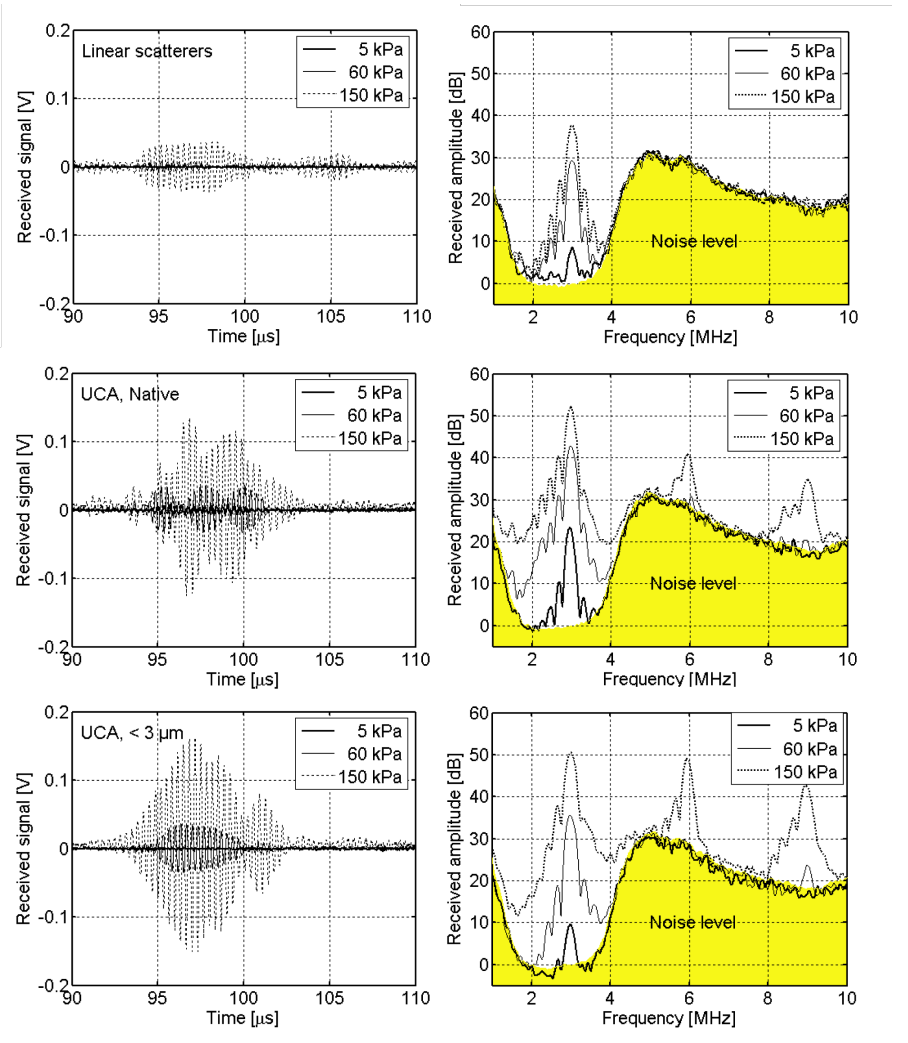

Figure 6.7: At a transmit frequency of 3.0 MHz, the scattering of a linear scatterers suspension (top), a native contrast agent suspension (middle) and a filtered contrast agent suspension (bottom). Examples of received signals at 5, 60 and 150 kPa are shown. The left column shows the radiofrequency data and the right column shows the corresponding power spectra.

ation was investigated (see Figs 6.4 and 6.5). A small ROA value shows a large increase of attenuation from 20-150 kPa, hence a large increase in microbubble activity. For the filtered microbubbles at 20 kPa, only 30% activity of the microbubbles was measured compared to the measurement at 150 kPa. For the native suspension, this was 60%. This

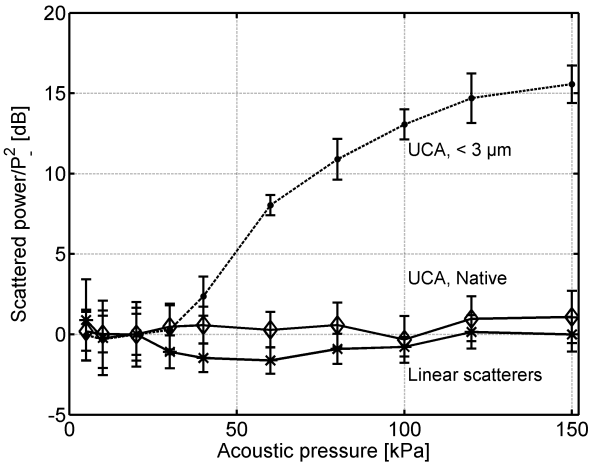

Figure 6.8: Normalized scattered powers as a function of the acoustic pressure (P_) of a native contrast agent suspension (UCA, Native), a filtered contrast agent suspension (UCA, < 3 μm) and a suspension with linear scatterers at a transmit frequency of 3 MHz. The standard deviations are indicated. The scattered power measured at 20 kPa was taken as the reference value.

difference between the native and filtered suspensions must be attributed to the microbubbles > 3.0 μm in diameter. From the Coulter Counter measurements, it appeared that the native suspension contained 21% more microbubbles including 4% microbubbles larger than 3.0 μm in diameter. These microbubbles obviously dominate in the dissipation of energy and show less threshold behavior than smaller microbubbles as was also observed in the optical studies (Emmer et al., 2007b). Removing these larger microbubbles enhanced the influence of threshold behavior.

For the native suspension, Fig 6.2 shows a maximum attenuation at 1.6 MHz, which is an indication for the resonance frequency of this population. Regarding Figs 6.4 and 6.5, a clear relationship between the pressure-dependence of the attenuation and the transmitted frequency was not found. For the native suspension, pressure-dependent attenuation was however more apparent at frequencies near 1.5 MHz, and for the filtered microbubbles at higher frequencies, indicating that the pressure-dependency is higher near resonance. This was also found by Tang and Eckersley (2007) for the contrast agent SonoVue, which resembles BR14, but has a gas core of sulphur hexafluoride.

In addition to the attenuation measurements, the influence of microbubble size on pressure-dependent scattering was investigated. A suspension of solid particles was applied to verify the influence of the acoustic pressure. As was expected, Fig 6.8 shows that these particles scattered linearly. For the native suspension at the fundamental frequency, the scattered power also increased proportionally to the acoustic pressure, which

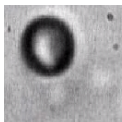

is supported by the findings of Tang and Eckersley (2007). The response of the filtered suspension is very different and showed highly nonlinear behavior at the fundamental frequency. From 30-150 kPa, the normalized scattered power increased 16 dB. In the scattering measurements, the influence of microbubble size was even larger than for the attenuation measurements. For larger microbubbles (insonified well above resonance), the scattering cross section approaches the physical scattering cross section, which outweighs the scattering by smaller microbubbles (below resonance). The measured scattered powers were dominated by the scattering of microbubbles with sizes > 3.0 μm diameter, which show less threshold behavior at the acoustic pressures applied. Removing these microbubbles revealed the scattering behavior of the smaller microbubbles, which was highly pressure dependent. This could be the result of threshold behavior and is in agreement with the attenuation results. The onset at 30 kPa is notable, and it is also consistent with the attenuation results shown in Fig 6.4. It may point out that for the filtered suspensions of microbubbles the threshold values of the individual microbubbles are above 30 kPa.

Regarding Fig 6.7, in addition to the fundamental scattering behavior, the second harmonic response is also notable. For the native suspension at 150 kPa, the difference between first and second harmonic was 11 dB, whereas for the filtered suspension this was 2 dB. Unfortunately, the receiving transducer was not very sensitive above 4 MHz, but at the higher acoustic pressures, the difference in second harmonic behavior between the two contrast agent suspensions is apparent. The enhanced second harmonic behavior of the filtered microbubbles may indicate that these microbubbles show more "compression-only" behavior. This highly nonlinear behavior occurs when the microbubble compresses more than it expands (de Jong et al., 2007), which is likely to result in more harmonics in the scattered echo. We believe that compression-only behavior may be related to threshold behavior. The possible influence of the phospholipid packing on microbubble behavior has been described in Marmottant et al. (2005) and Emmer et al. (2007a). One hypothesis is that gas diffuses from the microbubbles, resulting in smaller microbubbles with denser phospholipid-coatings. Tight phospholipid packing and thus high Van der Waals forces between the molecules may inhibit both compression and expansion of the microbubble (threshold behavior). When the acoustic pressure is increased the phospholipid monolayer may buckle (compression-only behavior), lose material (shrinkage of the microbubble) or rupture (behavior like a free microbubble).

Two other explanations for pressure-dependent attenuation are the nonlinear behavior of microbubbles and microbubble destruction (Casciaro et al., 2007; Chen et al., 2002). The first explanation implies that due to harmonic generation and additional damping, energy is lost. These effects are certainly present, but comparing Levovist to BR14, distinct attenuation results were observed. Both agents contain microbubbles, which vibrate and generate harmonics at low acoustic pressures (*e.g.* for Levovist see Schrope et al. (1992)). Pressure-dependent behavior was only observed, however, for BR14. The shells of these contrast agents differ, which could explain the influence of threshold behavior. Moreover, the scattering results cannot be explained from the generation of harmonics. For the filtered microbubbles, a nonlinear increase of the fundamental was observed. The

harmonics also increased, so a total increase of scattered energy was observed, which indicates an enhanced activity of the microbubbles. To determine the possible influence of microbubble destruction, it is important to consider what definition of microbubble destruction is relevant. In the optical study of Emmer et al. (2007b) at the acoustic pressures applied, fragmentation was not observed. The destruction mechanism of a phospholipid-coated microbubble is also different from a hard-shelled polymer/albumin contrast agent, which includes breakage and gas release (Bouakaz et al., 2005). Threshold behavior describes the onset of microbubble vibration. Forcing the microbubble into oscillation requires overcoming the acoustic pressure threshold. For some microbubbles, this will result in compression-only oscillations or a sort of rupture of the phospholipid coating leads to larger (more symmetrical) amplitudes of microbubble excursion (Marmottant et al., 2005). For the attenuation measurements, Fig 6.6 shows that the percentage of destroyed microbubbles was very low, from which it is concluded that in the results presented, microbubble destruction (breakage and gas release) had little influence.

This study was performed *in vitro*, in a controlled environment, which is different from the environment in the human body. The influence of the blood circulation to the pressure-dependence of both scattering and attenuation by the phospholipid-coated microbubbles was not investigated. We do, however, believe that the observed phenomena have implications for clinically applied imaging techniques such as power modulation imaging. This imaging technique is particularly developed to use the second harmonic responses of the microbubbles (Brock-Fisher et al., 1996), but the presence of pressure-dependent scattering behavior could be exploited to apply the power modulation technique at the fundamental frequency. For example our results show that using microbubbles with sizes < 3.0 μm diameter, at a transmit frequency of 3.0 MHz and acoustic pressures of 50 and 100 kPa would result in a power modulation signal of 8.0 dB. This has practical advantages such as the possibility to use a simple narrow-band transducer. The application of pressure-dependent scattering in a power modulation imaging technique has been demonstrated in two separate papers (Emmer et al., 2007a,c).

Acknowledgements We acknowledge Bracco Research (Geneva, Switzerland) for supplying the contrast agent BR14. This work is part of the research programme of the Stichting voor Fundamenteel Onderzoek der Materie (FOM), which is financially supported by the Nederlandse Organisatie voor Wetenschappelijk Onderzoek (NWO).

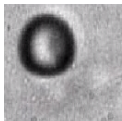

7

Clinical relevance of pressure-dependent scattering at low acoustic pressures

Marcia Emmer, Hendrik J. Vos, Annemieke van Wamel, David E. Goertz,
Michel Versluis, and Nico de Jong

Ultrasonics, 2007, 47:74-77

Abstract Recent optical and acoustical studies have shown a threshold behaviour in the response of phospholipid-coated contrast agents, for a certain range of sizes. Below the acoustic pressure threshold, the microbubbles' scattering efficacy is significantly reduced compared to that above the threshold. Here we investigate the clinical relevance of the observed threshold behaviour. A cardiac ultrasound scanner system was used to analyse the pressure-dependence of the scatter intensity. The scattering of a native suspension of a phospholipid-coated contrast agent was compared to that of a suspension in which microbubbles with a size larger than 3.0 μm in diameter were extracted. A power modulation scheme at the fundamental frequency was applied. After linearly scaling and subtracting the B-mode images recorded at 70 and 200 kPa, the contrast-to-tissue ratio (CTR) of the native suspension was 3.2 dB, whereas the CTR of the filtered suspension was 20 dB. The 17 dB difference is attributed to the threshold behaviour. Well-established ultrasound imaging techniques such as fundamental power modulation imaging could benefit from the pressure-dependent scattering properties of this type of contrast microbubbles.

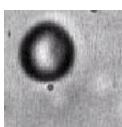

7.1 Introduction

Ultrasound (US) contrast agent imaging at low mechanical index (MI) is increasingly employed in a clinical setting and increasingly subject of research (Becher and Burns, 2000). US contrast agents consist of small (1-10 μm diameter) encapsulated gas-filled microbubbles. In an ultrasound field, the microbubbles oscillate due to the compressibility of their gas core. This oscillating behaviour is the primary source of the high scattering strength of these agents, which make them highly suited to provide contrast enhancement in diagnostic US imaging.

At low acoustic pressures and away from resonance, current descriptions of microbubble behaviour predict a linear relationship between encapsulated microbubble expansion and acoustic pressure. Using high-speed optical recordings, at 1.7 MHz transmission frequency, the onset of individual phospholipid-coated microbubble vibration was investigated, revealing a threshold in the response of microbubbles smaller than 5.0 μm in diameter (Emmer et al., 2007b). These individual microbubbles were observed to oscillate significantly less below the acoustic pressure threshold, ranging from 30 up to 120 kPa for the individual microbubbles. Above the threshold, their response was proportional to the acoustic pressure applied. These observations may be explained by size-dependent mechanical properties of the phospholipid shells, such as differences in the phospholipid packing and the occurrence of condensed phase domains (Emmer et al., 2007b).

The effects of this so-called "threshold behaviour" were also observed acoustically for a population of microbubbles. Ultrasound travelling through tissue is attenuated proportionally to its incident intensity and travelled distance (Duck, 1990). For phospholipid-coated microbubbles, recent studies showed an increasing attenuation when the acoustic pressure was increased (Chen et al., 2003; Tang et al., 2005; Tang and Eckersley, 2007; Emmer et al., 2006). For Levovist, which may be considered as a "free" microbubble, an increased attenuation was not observed (Emmer et al., 2006), which supports the hypothesis that pressure-dependent attenuation may be explained by the threshold behaviour. At low acoustic pressures, only a selection of microbubbles oscillates significantly and absorbs acoustic energy. When the acoustic pressure is increased, the pressure threshold of more microbubbles is exceeded leading to an increased attenuation.

Recently, the pressure-dependence of microbubble scattering was measured acoustically (Tang and Eckersley, 2007; Emmer et al., 2007c). We compared the scattering of a native phospholipid-coated microbubble suspension to that of a filtered suspension of microbubbles with a size smaller than 3.0 μm in diameter. At a transmission frequency of 3.0 MHz, two single-element transducers at right angles, were used to measure microbubble scattering at acoustic pressures between 5 and 150 kPa. Increasing the acoustic pressure from 50 to 100 kPa, (almost) no pressure-dependence was measured for the native suspension (see also (Tang and Eckersley, 2007)), but for the filtered suspension, an increase in scatter power of 8 dB (on top of the linearly gained 6 dB) was found.

The occurrence of threshold behaviour may be beneficial for an imaging technique such as power modulation imaging. This technique operates by sending two pulses into

the body, equal in shape, but with different amplitude. Based on the scaling property of linearity, the linear responses of tissue and bubbles can be cancelled to preferentially obtain the harmonic echoes of the bubbles alone. When only small bubbles are used, the presence of a threshold could be exploited to enhance the contrast in fundamental power modulation images.

In this study, a cardiac ultrasound scanner system was used to measure the pressure-dependence of the scatter intensity and to test the feasibility of using this for power modulation imaging at the fundamental frequency. A native suspension of phospholipid-coated contrast agent was compared to a suspension in which microbubbles with a size larger than 3.0 μm diameter were removed. Both resulting scatter intensities were compared to tissue, which is known to have a linear scatter relation with acoustic pressure (Duck, 1990). For this purpose, a tissue mimicking phantom (TMP) was used.

7.2 Materials and methods

A water tank was filled with saline (Isoton II, Coulter, Miami, FL) (Fig 7.1). At the bottom of the tank an acoustic absorbing pad was placed to reduce the influence of reflections. On this pad the TMP was placed, which was prepared as described in (**?**). A ring stand and clamp held the 2.5 MHz phased array transducer, which was connected to an ultrasound system (GE/VingMed System 5, Horton, Norway).

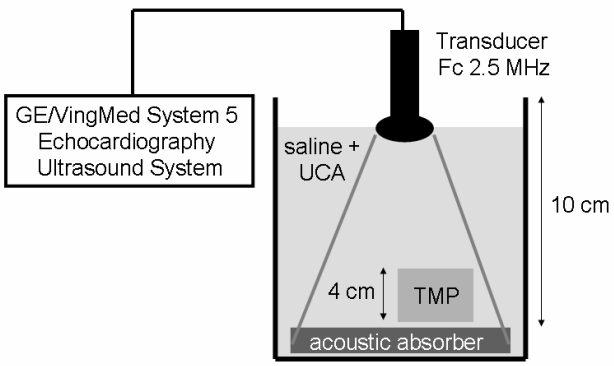

Figure 7.1: Schematic experimental set-up for the imaging experiments. A cardiac ultrasound scanner system insonified a tissue mimicking phantom (TMP) and an ultrasound contrast agent suspension (UCA).

The experimental phospholipid-coated contrast agent BR14 (Bracco Research SA, Geneva, Switzerland) was prepared in the vial by adding 5 ml of saline and shaking for 30 seconds. The scattering of two suspensions was measured. For the native BR14 suspension, 50 μl of contrast agent was added to 2.5 l saline in the water tank. For the

filtered suspension, 600 μl BR14 was diluted in 500 ml saline and mechanically filtered by gravity drainage through a porous polycarbonate membrane with 3.0 μm pore size (GE Osmonics Inc., Minnetonka, MN). The 500 ml were added to 2.0 l saline in the water tank.

After gently stirring the suspension, in ten seconds, a sequence of ten B-mode images was recorded in which the power was increased from -30 to -9 dB. The centre frequency of the transmitted pulses was 2.5 MHz, and the pulse duration was 1.1 μs. A 0.2 mm PVDF needle hydrophone (Precision Acoustics Ltd., Dorchester, UK) verified that the applied powers corresponded to peak negative pressures ranging from 30 to 320 kPa.

The B-mode images were recorded 8-bit log-compressed. Equation 7.1 shows how the pixel intensity power was calculated.

$$I^2 = (\frac{hp^2}{1-2hp})((\frac{1-hp}{hp})^{\frac{y}{127.5}} - 1) \tag{7.1}$$

where y is the log-compressed pixel value and hp is the precompression factor, which was 0.2 for the native suspension and 0.1 for the filtered suspension. To determine the average scatter intensities, in each image, at the same height, a region of interest (ROI) was selected in both the TMP and the contrast suspensions. By averaging the pixel intensity powers and taking the square root, the mean pixel intensity (I_{mean}) was determined.

Table 7.1: Mean pixel intensities and standard deviations of the ROI in the TMP and contrast agent suspension

	Native suspension		Filtered suspension	
	I_{mean}	SD	I_{mean}	SD
TMP	1.0×10^{-2}	0.5×10^{-2}	1.2×10^{-2}	0.7×10^{-2}
Contrast agent	1.5×10^{-2}	0.6×10^{-2}	0.9×10^{-2}	0.8×10^{-2}

7.3 Results

The recorded B-mode images consisted of 322x71 pixels, which corresponded after conversion to a sector scan to a field of view of 10x11 cm (height x width) (Fig 7.2). At the lower end of the scan, the lighter region indicates the acoustic absorbing pad. The TMP is located to the right of the scan and to the left, the speckle pattern of either the native contrast agent suspension (left panel) or that of the filtered suspension (right panel) is seen. A ROI of 90x30 pixels was selected in the TMP and contrast agent suspensions. The mean pixel intensities and standard deviations (SD) are presented in Table 7.1.

For all acoustic pressures, Fig 7.3 shows the normalised (I_{mean}), which was divided by the acoustic pressure and rescaled (all intensities were multiplied by the same constant, $C = 100kPa/I_{tissue}(100kPa)$). Linear scattering results in a straight line, which

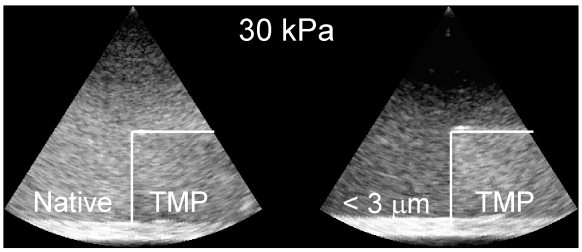

Figure 7.2: B-mode images recorded at a peak negative pressure of 30 kPa. Tissue mimicking phantoms (TMP) and ultrasound contrast agent suspensions (UCA) are depicted. Left panel: native suspension. Right panel: filtered suspension (pore size 3 μm).

was observed for the TMP. The normalised scatter intensity of the native suspension has a faint slope. The normalised scatter intensity of the filtered suspension however shows a striking different pattern. It increases up to 200 kPa and then appears to stabilise at a value twice of the mean intensity at 30 kPa.

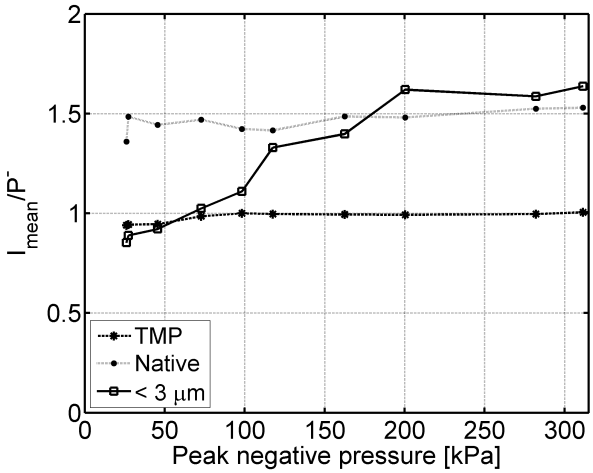

Figure 7.3: Normalised mean pixel intensity of the tissue mimicking phantom (TMP), native suspension (UCA, native) and filtered suspension (UCA, < 3 μm), recorded as a function of the acoustic pressure.

Using this distinct behaviour of the smaller microbubbles in a power modulation imaging technique, we can enhance the contrast in B-mode images. As an example, the

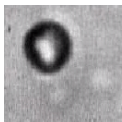

B-mode images recorded at 70 and 200 kPa were selected and the pixel intensity powers were calculated according to Eq (7.1). After linearly scaling the image recorded at 70 kPa (*i.e.* multiplying by 200/70), it was subtracted from the image recorded at 200 kPa. Figure 7.4 shows the resulting images after conversion to a sector scan, including a logarithmic scale with 64 grey values, a dynamic range of 45 dB and a gain of 35 dB. The dark square shows that the linear response of the TMP has been cancelled, while the responses of the contrast agent suspensions are still seen. For the native suspension, the resulting contrast-to-tissue ratio (CTR) was 3.2 dB and for the filtered suspension 20 dB. Thus the filtered suspension leads to an increase of the CTR by 17 dB compared to the native suspension.

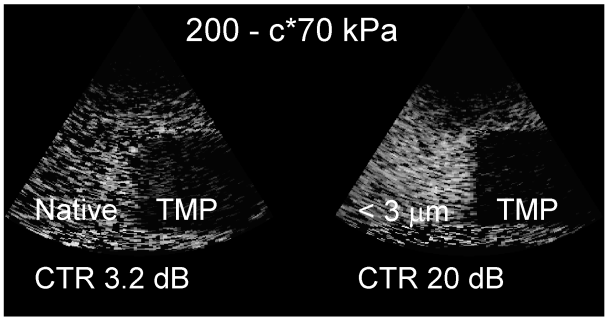

Figure 7.4: Example of power modulation. The linearly scaled B-mode image (c = 200/70), recorded at 70 kPa, is subtracted from B-mode image recorded at 200 kPa. Left panel: native suspension (UCA, native). Right panel: filtered suspension (UCA, < 3 μm).

7.4 Discussion

In previous studies (Emmer et al., 2007a,b,c), it was observed that the microbubble vibrations are suppressed at low driving pressures and for a certain range of size. From current theoretical models describing microbubble dynamics behaviour, it is expected that at the onset of their vibration, microbubbles respond proportional to the applied acoustic pressure, however this was not observed until the acoustic pressure exceeded a threshold value.

At 30 kPa, the scatter power of the native suspension was higher than the scatter power of the filtered suspension (Fig 7.2). When the acoustic pressure was increased, the normalised scatter intensity of the filtered microbubbles increased to a value higher than that of the native suspension (Fig 7.3). We attribute this effect as a result of the previously reported threshold behaviour. The microbubbles in the suspension with sizes smaller than 3.0 μm were not fully activated at a pressure of 30 kPa. For these microbubbles,

a doubling in the acoustic pressure resulted in an increase of the average pixel intensity by a factor 2.3. Such a pressure-dependent scattering of microbubbles smaller than 3.0 μm has been observed before (Emmer et al., 2007c). The normalised scattering power of the TMP remained constant with pressure, which is expected for a linear scatterer (Duck, 1990). The normalised scattering intensity of the native suspension depended much less on the acoustic pressure, compared to that of the filtered suspension. It is dominated by the (geometrical) scattering of microbubbles larger than 3.0 μm, which show less threshold behaviour at the acoustic pressures applied, see also Emmer et al. (2007b).

Power modulation imaging in conventional operation utilises the strong nonlinear behaviour of microbubbles to distinguish them from tissue. Linearly scaling and subtraction leaves mainly the harmonic components of the microbubbles. Figure 7.4 shows that also at the fundamental frequency, power modulation imaging can be employed using the nonlinear threshold behaviour. Threshold behaviour allowed for a contrast enhancement of 17 dB. This does not imply that threshold behaviour has not been used already. It is conceivable that current imaging techniques already profited from this additional nonlinear behaviour of the phospholipid-coated microbubbles.

In conclusion, the pressure-dependence of phospholipid-coated microbubble scattering has been measured with a cardiac ultrasound scanner system. At low acoustic pressures, it is expected that the normalised scatter intensity is pressure-independent, which was mainly the case for a native suspension of contrast microbubbles. For a suspension of microbubbles with a size smaller than 3.0 μm in diameter however, a pressure-dependent scattering was observed up to a pressure of 200 kPa. Microbubble threshold behaviour may explain the observed pressure-dependent scattering, which is highly beneficial for an imaging technique such as power modulation imaging at the fundamental frequency.

Acknowledgements This work is part of the research programme of the Foundation for Fundamental Research of Matter (Stichting FOM), which is financially supported by the Dutch Association for Scientific Research (NWO). We acknowledge Bracco Research, Geneva for kindly supplying the contrast agent BR14.

8

Improved ultrasound contrast agent detection in a clinical setting

Marcia Emmer, Guillaume Matte, Paul van Neer, Annemieke van Wamel, and Nico de Jong

IEEE Ultrasonics Symposium, 2007, 2235-2238

Abstract Optical studies have shown threshold behaviour of phospholipid-coated contrast agent microbubbles. Below the acoustic pressure threshold, phospholipid-coated microbubbles oscillate significantly less than above the threshold. For microbubbles smaller than 3.0 μm diameter, pressure-dependent scattering was measured, which is believed to be the result of threshold behaviour. The aim of this study is to investigate if threshold behaviour is useful to enhance the contrast in power modulation images. For levovist and BR14 suspensions (filtered and native), a programmable ultrasound system recorded power modulation images at 2 MHz and acoustic pressures between 25 and 250 kPa. Results were compared to intensities recorded with a commercial ultrasound system. An inverse relationship between the pressure-dependency of the scattering and microbubble size was observed. Threshold behaviour enhances the contrast in power modulation images. Using a suspension with microbubbles smaller than 2.0 μm, at 2 MHz transmit frequency and an acoustic pressure of 250 kPa, the CTR value was 33 dB, which is 13 dB higher compared to a native BR14 suspension.

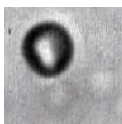

8.1 Introduction

High-speed optical recordings of individual microbubbles revealed threshold behaviour for phospholipid-coated microbubbles with sizes smaller than 5.0 μm in diameter (Emmer et al., 2007b). In these recordings, the onset of microbubble vibration was investigated. Although, current descriptions of microbubble behaviour predict a linear relationship between relative expansion of off-resonance encapsulated microbubbles and low acoustic pressures, this was not found for microbubbles smaller than 5.0 μm diameter. For these microbubbles, acoustic pressure had to increase above threshold values ranging from 30 to 120 kPa for the individual microbubbles before their response was proportional to the acoustic pressure applied. These observations may be explained by size-dependent mechanical properties of the phospholipid shells.

The effects of threshold behaviour are also observed acoustically (Emmer et al., 2006, 2007c). In contrast to the "free" microbubble Levovist, phospholipid-coated microbubbles show pressure-dependent attenuation. It is believed that threshold behaviour is typical for phospholipid-coated contrast agents and that it explains the pressure-dependency of the contrast agents attenuation. At low acoustic pressures, only a selection of microbubbles oscillates significantly and absorbs acoustic energy. When the acoustic pressure is increased, the pressure threshold of more microbubbles is exceeded leading to an increased attenuation.

Threshold behaviour is related to size. The scattering as a function of acoustic pressure of mechanically filtered microbubble suspensions has been studied (Emmer et al., 2007c,d). Suspensions without microbubbles larger than 3.0 μm diameter showed pressure-dependent scattering, which is different from the pressure-independent scattering of a native suspension. For filters with other pore sizes, this has not been investigated yet.

The occurrence of threshold behaviour is useful for an imaging technique such as power modulation imaging. This technique operates by sending two pulses into the body, which are equal in shape, but have different amplitudes. Based on the scaling property of linearity, the linear responses of tissue and bubbles can be cancelled to obtain the harmonic echoes of the bubbles alone. When only small bubbles are used, the presence of threshold behaviour could be exploited to enhance the contrast between tissue and bubbles.

The aim of this study is to investigate if threshold behaviour enhances the contrast in power modulation images. Secondly, the influence of microbubble size on the pressure-dependency of scattering was studied. For this purpose, a programmable ultrasound system was used. Recorded intensities are compared to intensities recorded with a commercial ultrasound system.

8.2 Materials and methods

A water tank was filled with degassed water (Fig 8.1). At the bottom of the tank an acoustic absorbing pad was placed to reduce the influence of reflections. On this pad

a tissue-mimicking phantom was placed. The phantom was prepared by adding 5 g of agar powder (Boom, Meppel, The Netherlands) and 0.5 g of scatterers (Carborundum No. 600, Cats, Hoogvliet, The Netherlands) to 250 ml deionised water. A ring stand and clamp held the 2.5 MHz phased array transducer, which was connected to a commercial ultrasound system (GE/VingMed System 5, Horton, Norway) or a 128 channels programmable ultrasound system (OPEN system, Lecoeur Electronique, Chuelles, France). The focal distance was 5.0 cm.

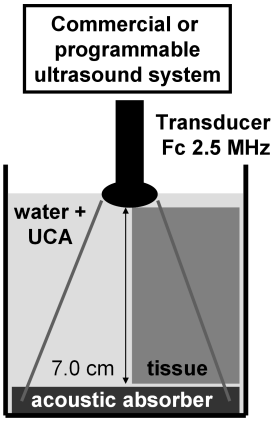

Figure 8.1: Experimental setup to record the scattering of contrast agent suspensions (UCA) and a tissue mimicking phantom.

Different suspensions of contrast agent were added to the water tank. The phospholipid-coated contrast agent BR14 (Bracco Research SA, Geneva, Switzerland) was compared to the "free" contrast agent Levovist® (Schering AG, Berlin, Germany). BR14 was applied unmodified (native) and mechanically filtered by gravity drainage through a porous polycarbonate membrane with 2.0, 3.0 or 5.0 μm pore size (GE Osmonics Inc., Minnetonka, MN). Concentrations of the suspensions are given in Table 8.1.

On each contrast agent suspension, a series of recordings with both ultrasound systems was performed. A magnetic stirrer refreshed the microbubbles in the scanning plane between frames. The commercial ultrasound system was set at a frequency of 2.0 MHz and recorded subsequent B-mode images at powers from -30 to -10 dB at a repetition rate of approximately 1 s. The programmable ultrasound system transmitted pulses composed by unipolar square wave transmitters. Voltages from 5 to 20 V were applied. The system was programmed to operate in a power modulation mode at 2.0 MHz. The first pulse was fired at full power and the second pulse at half power. The time between two pulses was 1.4 ms. For each pulse, RF data was recorded. After subtraction of the scaled half power RF lines from the full power RF lines, the power modulation images resulted. They could be imaged real-time at a frame rate of 5 Hz. A 0.2 mm PVDF needle hydrophone (Precision Acoustics Ltd., Dorchester, UK) verified that the applied powers

corresponded to peak negative pressures ranging from 25 to 250 kPa.

To determine the scatter intensity as a function of acoustic pressure, a region of interest in both the tissue mimicking phantom and the contrast agent suspension was defined. The recorded B-mode images consisted of 258x59 pixels, which corresponded after conversion to a sector scan to a field of view of 8x8 cm. The ROI size was 70x15 pixels. For the programmable ultrasound system, RF data resulted from the recordings, 62 lines divided into 2100 sample points, also corresponding to an image of 8x8 cm. The average amplitude of an ROI of 264x11 sample points was determined.

Table 8.1: Concentrations of the contrast agent suspensions

		BR14			Levovist
	Native	$< 2\ \mu$m	$< 3\ \mu$m	$< 5\ \mu$m	
Concentration [μl/l]	25	250	250	100	250

8.3 Results

For the programmable ultrasound system, the repeatability of the pulses was tested. At the same angle, 4 RF lines were acquired, alternately at half and full power. Figure 8.2 shows RF lines recorded at 250 kPa (full power) and 125 kPa (half power) for the native BR14 suspension. No significant differences between the RF lines recorded at low power, neither between the RF lines recorded at high power are observed. It is however observed that between low and high power the shape of the RF lines changes, which also appears from the frequency domain.

The scales of the scatter intensities recorded by the commercial and programmable ultrasound systems are not the same (Fig 8.3 and 8.4). The commercial ultrasound system recorded the B-mode images 8-bit log-compressed. When transferring this into a linear scale, relatively more weight is given to the brighter intensities, see also Emmer et al. (2007d). For the programmable ultrasound system, the RF data was recorded in a 12-bit linear scale.

Comparing Fig 8.3 and 8.4, similar results are however observed. The scattering of both the tissue mimicking phantom and Levovist was pressure-independent, which is different from the BR14 suspensions. The native suspension increased 50% from 25 to 250 kPa, but this becomes strikingly more when the average microbubble size of the suspension applied decreases. The suspension with only microbubble sizes smaller than 2.0 μm in diameter increased the most, 560% from 25 to 250 kPa. For this suspension below 90 kPa, the intensities were however below noise level, so for a higher concentration, this difference will be even higher.

To investigate the intensities of the power modulation images, it must be accounted for that the scatter intensity largely depends on microbubble size. For a good compari-

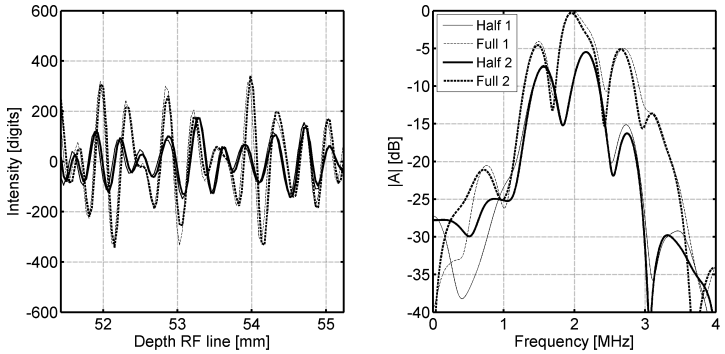

Figure 8.2: RF lines recorded at 250 kPa (full power) and 125 kPa (half power) for the native BR14 suspension. At the same angle, four RF lines were acquired, alternately at half and full power.

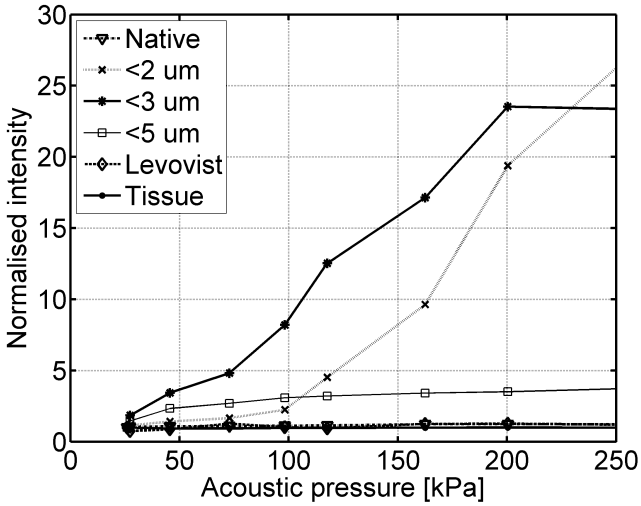

Figure 8.3: Normalised average pixel intensity as a function of acoustic pressure recorded with the commercial ultrasound system.

son, the intensities were compensated for concentration differences by normalising the intensities to the native BR14 intensity recorded at 90 kPa. The normalisation factor was determined by dividing the intensity of the contrast agent suspension at 90 kPa by the intensity of the native BR14 suspension at 90 kPa (Table 8.2). This acoustic pressure

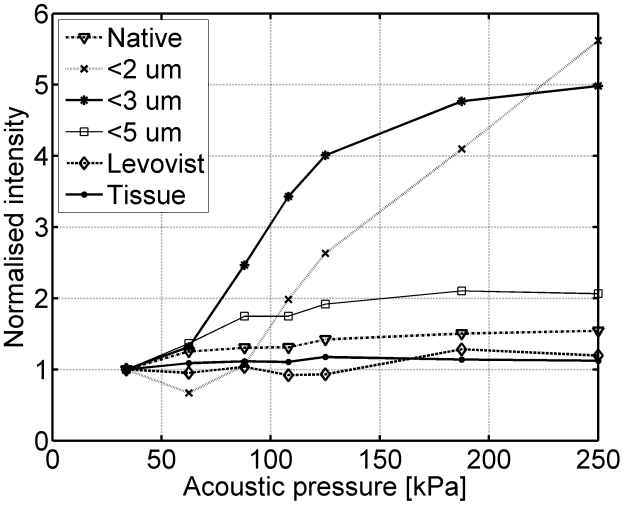

Figure 8.4: Normalised average amplitude intensity of the RF data as a function of acoustic pressure recorded with the programmable ultrasound system.

Table 8.2: Normalisation factor for each suspension

		BR14			Levovist
	Native	$< 2\ \mu$m	$< 3\ \mu$m	$< 5\ \mu$m	
Factor	1	4.5	1.8	1	3

was chosen, because it was the first acoustic pressure where all contrast agent intensities were above the noise level (20 digits).

In the power modulation images recorded by the programmable ultrasound system, the signal from the tissue mimicking phantom was cancelled well (Fig 8.5). A CTR of 20 dB resulted from a power modulation image of native BR14 suspension at 250 kPa. For the filtered suspensions, including the factors of Table 8.2, higher CTR values were observed. For the suspension with microbubble sizes smaller than 2.0 μm in diameter the CTR was 33 dB.

Figure 8.6 shows the intensities of the power modulation images at all acoustic pressures applied (including the factors of Table 8.2). The intensity of the tissue mimicking phantom is at least a factor 2 lower than the intensities of the contrast agent suspensions. Moreover the intensity of tissue in the power modulation image was not pressure-dependent, which is in great contrast to the contrast agent suspensions. The intensities of all contrast agent suspensions were pressure-dependent, but also in the intensities of the

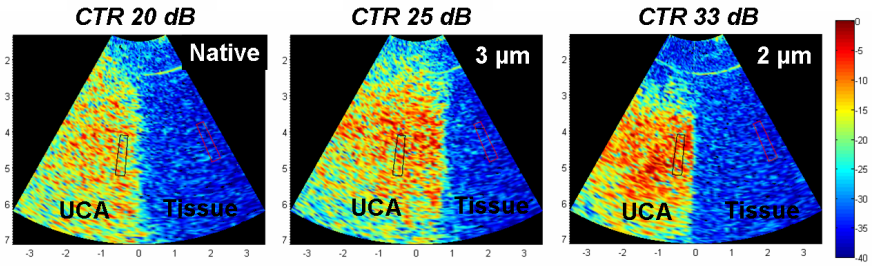

Figure 8.5: Power modulation images of phospholipid-coated contrast agent suspensions (native and filtered, pore size 2.0 and 3.0 μm).

power modulation images it is observed that the filtered suspensions were most pressure-dependent.

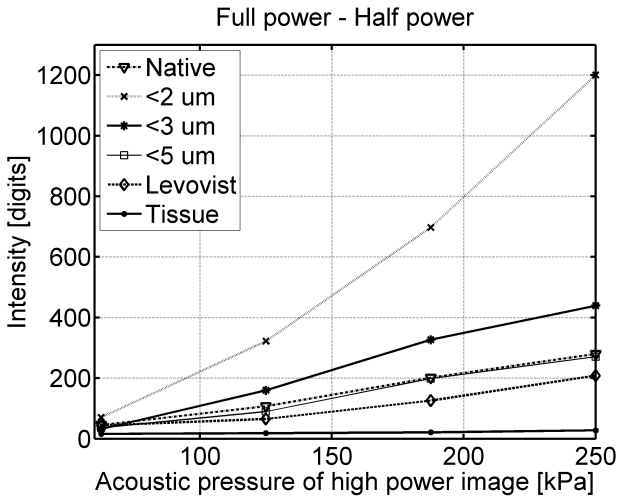

Figure 8.6: Average intensity of the power modulation images. For the power modulation image, the scaled half power RF lines were subtracted from the full power RF lines.

8.4 Discussion

For a phospholipid-coated microbubble suspension with microbubble sizes smaller than 3.0 μm, previous studies (Emmer et al., 2007c) showed strong pressure-dependent scattering. In this study, also filter pore sizes of 2.0 and 5.0 were applied, which showed

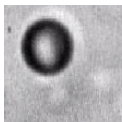

that there is an inverse relationship between microbubble size and the slope of the scattering response as a function of acoustic pressure (Fig 8.3 and 8.4). It is hypothesised that pressure-dependent scattering is explained by threshold behaviour. At low acoustic pressures, only a selection of microbubbles oscillates significantly and scatters acoustic energy. When the acoustic pressure is increased, the pressure threshold of more microbubbles is exceeded leading to an increased scattering. Threshold behaviour is typical for phospholipid-coated contrast agents, accordingly no pressure-dependent scattering was found for the "free" contrast agent Levovist.

Figure 8.3 and 8.4 show the effects of threshold behaviour on the scatter intensity as a function of the acoustic pressure. In a power modulation image, not only the amplitude of the signals is important, also the phase of the signals. Amplitude and phase changes between signals may have various causes. In Fig 8.2, no significant differences for RF lines acquired at the same power were observed, which means that the microbubbles did not move and were not significantly destroyed. Between two powers, the signals did however differ. Part of these differences may be explained by threshold behaviour, but in Fig 8.6, also for the native BR14 and Levovist suspensions some pressure-dependent intensity differences are observed. These are likely the result of nonlinear oscillations of the microbubbles and the scattering of energy at the harmonic frequencies. From Fig 8.6, it is however concluded that the effect of threshold behaviour is dominant. Figure 8.5 shows that 13 dB more CTR is obtained using only microbubbles smaller than 2.0 μm instead of a native suspension.

8.5 Conclusions

An inverse relationship between the pressure-dependency of the scattering and microbubble size was measured, which is believed to be an effect of threshold behaviour. This behaviour of smaller phospholipid-coated microbubbles is useful to enhance the contrast in power modulation images. Using a suspension with microbubbles smaller than 2.0 μm, at 2 MHz transmit frequency and an acoustic pressure of 250 kPa, the CTR value was 33 dB, which is 13 dB higher compared to a native BR14 suspension.

9

Radial modulation of single microbubbles

Marcia Emmer, Hendrik J. Vos, and Nico de Jong

Submitted to IEEE Transactions on Ultrasonics, Ferroelectrics, and Frequency Control

Abstract Radial modulation imaging is a new promising technique to improve contrast-enhanced ultrasound images. The method is based on dual-frequency insonation of contrast agent microbubbles. A low frequency (LF) pulse is used to modulate the responses of the microbubbles to a high frequency (HF) imaging pulse. Inverting the LF pulse induces amplitude and phase differences in the HF response of contrast agent microbubbles, which can be detected using Doppler techniques. Although the technique has been successfully implemented, no consensus persists on parameter choice and resulting effects. In a separate study 'compression-only behavior' of coated microbubbles was observed. Compression-only behavior could be beneficial for radial modulation imaging. We investigated this by studying the behavior of coated microbubbles in a dual-frequency ultrasound field using high-speed camera recordings and simulations. We recorded the vibrations of 78 single microbubbles. The results show that the LF pulse induced significant compression-only behavior, which for microbubble sizes below and at HF resonance resulted in high radial amplitude modulation. It however also appeared that for radial modulation imaging, microbubble size is more important than resonance and compression-only effects.

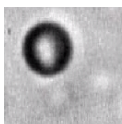

9.1 Introduction

Ultrasound imaging is widely used in various clinical radiology and cardiology applications. The intravenous injection of coated gas microbubbles as a contrast agent significantly enhances the acoustic backscattering from blood and thus the ability to detect blood flow in soft tissue. The microbubbles are effective scatterers owing to the large compressibility difference between the surrounding fluid and the coated gas. Under the influence of an ultrasound field, the microbubbles may vibrate linearly and nonlinearly. Nonlinear vibrations result in a backscattered signal containing higher harmonics of the incident frequency. Current contrast agent detection techniques exploit these harmonic signals, e.g. harmonic imaging (Schrope and Newhouse, 1993), pulse inversion (Hope Simpson et al., 1999), power modulation (Brock-Fisher et al., 1996), and combinations of these methods. However, tissue also generates harmonics due to nonlinear propagation (Duck, 2002), with the result that the detection of contrast microbubble harmonics competes with the detection of tissue harmonics.

New strategies are investigated to further improve the detection of contrast agents. An example of such a strategy is radial modulation imaging, which is based on dual-frequency insonation. A combination of two pulses is transmitted, a low frequency (LF) pulse, which acts as a modulator signal and a high frequency (HF) pulse, which is used for imaging. This combination of pulses is transmitted repeatedly with alternating positive and negative modulator signals. The contrast microbubbles can be extracted from tissue using techniques analogous to pulsed-wave Doppler techniques (Chérin et al., 2008; Måsøy et al., 2008).

In 1984, Newhouse and Mohana Shankar (1984) already measured bubble sizes using double-frequency insonation. Due to the resonance behavior of the microbubbles, the echo will contain sidebands at HF $\pm$ LF, as well as higher order terms, unique for each microbubble size (Newhouse and Mohana Shankar, 1984). Since, many studies have proposed to use dual-frequency insonation to enhance the detection of microbubble scattering, e.g. Wyczalkowski and Szeri (2003) combined 1 and 3 MHz in such a way to maximize the acoustic radiation of a bubble at 2 MHz. Roy et al. (1990) applied 10 μs-long combined LF and HF bursts to detect transient cavitation. Deng et al. (2000) were the first to suggest the use of a short HF pulse combined with a long LF pulse. They placed the HF pulse on a LF minimum or maximum to probe various aspects of LF effects. Introduced as a dual-frequency strategy to study microbubble behavior, this strategy expanded when it was introduced as an imaging technique, called radial modulation imaging (Chérin et al., 2008; Måsøy et al., 2008; Shariff et al., 2006a). An advantage of the method mentioned is that the contrast agent detection frequency is decoupled from the resonance frequency of the microbubbles, allowing detection at clinically-high frequencies for a high-resolution detection of the contrast agent (Chérin et al., 2008; Måsøy et al., 2008; Shariff et al., 2006a).

Radial modulation imaging is based on detecting decorrelation of the HF imaging signals induced by the LF modulation. This modulation may affect the amplitude and/or phase of the HF response, which depends on the choice of LF and HF with respect to the

resonant frequency of the microbubble. Literature delivers different messages. Whereas the first papers (Deng et al., 2000; Shariff et al., 2006a; Hansen et al., 2005; Shariff et al., 2006b) suggest that the LF should be chosen near the resonant frequency of the microbubbles, Bouakaz et al. (2007) propose to adjust the HF to the resonant frequency of the microbubbles. More recent studies based on numerical simulations indicate that best results are obtained when the HF approaches the microbubble resonant frequency from above (Angelsen and Hansen, 2007) or that the LF should be below the resonant frequency of the microbubbles in the population (Chérin et al., 2008).

With a high-speed camera we can investigate the response of the microbubbles in a dual-frequency ultrasound field and study the modulation of the HF response by the LF pulse. Moreover, it will appear if other effects will influence the dual-frequency response. For example, in previous single-frequency studies, we have observed 'compression-only behavior' by the microbubbles (de Jong et al., 2007). These microbubbles showed asymmetrical radial responses with a compression amplitude that was at least two times greater than the expansion amplitude. Compression-only behavior could be beneficial for the radial modulation of microbubbles.

The aim of this study is to investigate the behavior of single phospholipid-coated microbubbles in a dual-frequency ultrasound field. Gained knowledge is useful for the fundamental understanding of coated bubble behavior, but it also is useful for the implementation of the radial modulation imaging technique, which should account for the influence of microbubble size and transmit frequencies. We used high-speed optical recordings and simulations. To investigate which type of bubble model predicts observed dual-frequency behavior best, the outcome of three different models was qualitatively compared to the high-speed recordings. One of these models is the model for large amplitude oscillations by Marmottant et al. (2005). We applied low intensity ultrasound bursts at frequencies useful for precordial examination.

9.2 Materials and methods

9.2.1 Simulations

Responses of (1) free gas microbubbles, (2) elastic-coated microbubbles and (3) buckling-coated microbubbles in a dual-frequency ultrasound field were simulated based on the model for large amplitude bubble dynamics by Marmottant et al. (2005).

1) The free gas microbubble was modeled using the modified Rayleigh-Plesset equation (Keller and Miksis, 1980)

$$\rho_l\left(R\ddot{R}+\frac{3}{2}\dot{R}^2\right) = \left(P_0+\frac{2\sigma(R_0)}{R_0}\right)\left(\frac{R}{R_0}\right)^{-3\kappa}\left(1-\frac{3\kappa}{c}\dot{R}\right) - \frac{2\sigma(R)}{R}-\frac{4\mu\dot{R}}{R}-\frac{4\kappa_s\dot{R}}{R^2}-p_0-P_{ac}(t) \qquad (9.1)$$

where R, $\dot{R}$ and $\ddot{R}$ represent the radius, velocity and acceleration of the microbubble wall,

R_0 is the resting radius of the microbubble, $\rho_l = 10^3$ kg/m^3 is the density of water, σ is the surface tension, κ is the polytropic exponent, $c = 1.5 \times 10^3$ m/s is the speed of sound in water, $\mu = 10^{-3}$ Pa s is the dynamic viscosity of water, and $P_{ac}(t)$ is the driving acoustic pressure. The influence of thermal damping was expected to be small (Stride and Saffari, 2004; van der Meer et al., 2007) and for the sake of simplicity ignored. The gas core consisted of SF_6. The polytropic exponent was assumed to equal the ratio of specific heats, which results for SEF_6 in κ = 1.095. In the case of free gas microbubbles, the surface tension $(\sigma(R))$ was a constant and had a value of $\sigma_w = 7.2 \times 10^{-2} N/m$.

2) The coating of the elastic-coated microbubbles was modeled using two parameters, the viscosity parameter κ_s and the elasticity modulus χ. We define the coating viscosity term as in Marmottant et al. (2005), except that in our case κ_s depends on the initial microbubble radius R_0. This relationship between (κ_s) and R_0 has been shown by van der Meer et al. (2007) and we use Fig 8 from their paper, to determine the relationship, resulting in the following expressions,

$$-\frac{4\kappa_s \dot{R}}{R^2} \quad \text{where} \quad \kappa_s(R_0) = 10^{-9.0+0.37*R_0}\text{kg/s} \tag{9.2}$$

This viscosity term was added to Eq (9.1). A coating surrounding the gas core affects the surface tension $(\sigma(R))$ of the microbubble. First, we assume that the coating behaves as a linear elastic solid and we extend the surface tension of Eq (9.1) with the influence of the coating elasticity χ (Eq 9.3).

$$\sigma(R) = \sigma_w - 2\chi(\frac{R}{R_0} - 1) \tag{9.3}$$

We included in Eq (9.1) the influence of a linear elastic coating. The model that we have obtained is except for the variable coating viscosity, the model by de Jong et al. (1994).

3) The model by de Jong et al. (1994) can be extended such that we obtain the model by Marmottant et al. (2005). We used the latter model to predict the behavior of the buckling-coated microbubbles. The model by Marmottant et al. (2005) aims at a more realistic modeling of the physical properties of the lipid monolayer coating and predicts observed nonlinear behavior such as compression-only behavior (de Jong et al., 2007). The core of the model is a dynamic surface tension, which can be in three regimes depending on the microbubble radius,

$$\sigma(R) = \begin{cases} 0 & \text{if } R \leq R_{\text{buckling}} \\ \chi\left(\frac{R^2}{R^2_{\text{buckling}}} - 1\right) & \text{if } R_{\text{buckling}} \leq R \leq R_{\text{break-up}} \\ \sigma_{\text{water}} & \text{if } R > R_{ruptured} \end{cases} \tag{9.4}$$

For radii below $R_{buckling}$, the coating of the microbubble buckles and the surface tension vanishes. To assure compression-only behavior, $R_{buckling}$ was taken equal to R_0. For radii between $R_{buckling}$ and $R_{break-up}$, the coating is assumed to be elastic, which is expressed by the elastic modulus χ = 1.0 N/m. When $R > R_{ruptured}$, the coating ruptures and the surface tension becomes equal to that of the gas-liquid interface of a

free gas microbubble σ_w. The buckling-coated microbubbles are modeled similar to the elastic-coated microbubbles except that the dynamic surface tension of Eq (9.4) replaces Eq (9.3).

Simulations were carried out for microbubble sizes from 0.5-6.0 μm in diameter. The input was the acoustic pressure signal applied in the high-speed recordings. This signal was measured using a hydrophone and consisted of a LF pulse and a HF pulse. The LF pulse was a gated four-cycle-sine wave burst at 0.5 MHz center frequency and had a peak negative pressure of 30 kPa. The HF pulse was a gated 33-cycle-sine wave burst at 3.75 MHz centre frequency (HF) and had a peak negative pressure of 80 kPa. We calculated the diameter of each microbubble as a function of time, $D(t)$, in response to a single HF pulse and in response to a combination of the LF and HF pulses. In the latter case, two responses were calculated whereby the LF pulse was inverted.

For the radial modulation imaging technique, the scattered sound pressure by the bubble is more important than the radial response. We therefore calculate from the radial responses, the radiated sound pressures using the derivation by Hilgenfeldt et al. (1998),

$$P_s = \rho_l \frac{R}{r}(2\dot{R}^2 + R\ddot{R}) \tag{9.5}$$

where r is the distance from the microbubble, which was taken equal to the focal distance of the transducers (r = 75 mm) that were used in the experiments. Amplitude values of the radial and acoustic responses were determined using the envelope of these responses, which was calculated applying IQ-demodulation.

9.2.2 Experiments

High-speed recordings were performed using the setup shown in Fig 9.1. A Perspex water tank filled with air-saturated water contained two single element transducers. The first transducer used for the LF pulses had a center frequency of 0.5 MHz and an aperture diameter of 38 mm (V389, Panametrics-NDT, Olympus NDT, Waltham, MA, USA). The other transducer had a center frequency of 3.5 MHz and an aperture diameter of 25 mm (V380, Olympus NDT). They were focused at the same region-of-interest in a cellulose Cuprophan® capillary tube (inner diameter 160 μm and outer diameter 200 μm, Akzo Nobel Faser AG, Wuppertal, Germany). The transducers were controlled by a two-channel waveform generator (8026, Tabor Electronics Ltd., Tel Hanan, Israel) and two power amplifiers (LF: 150A100B, AR, Souderton, PA, USA and HF: A-500, ENI, Rochester, NY, USA). The objective of a BX-FM microscope (Olympus Nederland BV, Zoeterwoude, The Netherlands) was positioned above the capillary tube and projected the microbubbles with 240x magnification (LUMPlan 60x water immersion objective and 2x2 magnifiers) onto a customly-built high-speed camera system, the Brandaris 128 (Chin et al., 2003). This system is capable of digitally acquiring 128 frames with a maximum frame rate of 25 million frames-per-second. The illumination source was a xenon flash lamp (MVS-7010, Perkin-Elmer Optoelectronics, Salem, MA, USA) connected to an optic fiber (Olympus) mounted below the capillary tube and microscope objective.

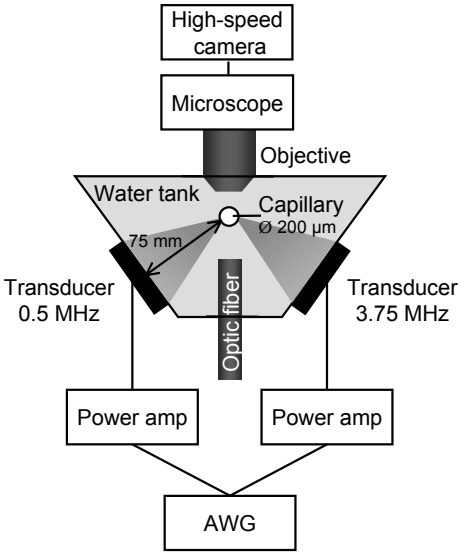

Figure 9.1: Scheme of the experimental setup for the optical recording of single microbubbles.

SonoVue microbubbles were prepared as prescribed by the manufacturer (Bracco SpA, Milan, Italy) and diluted such that after injection in the capillary tube, one to four microbubbles were present in the image frame of 31x42 μm. The microbubbles were recorded in six sequences of 128 image frames at a frame rate of 12 million frames per second. The time between the sequences was 80 ms. In the first sequence, no ultrasound was applied to determine the resting size of the microbubbles. In the second and fifth sequence, the microbubbles were insonified with a gated four-cycle-sine wave burst at 0.5 MHz center frequency and a peak negative pressure of 30 kPa. In the third and sixth sequence, the microbubbles were insonified with a gated 33-cycle-sine wave burst at 3.75 MHz centre frequency and a peak negative pressure of 80 kPa. Both transducers insonified the microbubbles in the fourth sequence. In a separate experiment, a calibrated 0.2-mm PVDF hydrophone (Precision Acoustics Ltd., Dorchester, UK) was used to verify the acoustic pressures.

From the recordings, we obtain the microbubble diameter as a function of time, $D(t)$, by measuring the diameter in each image frame with a semiautomatic procedure using a minimal cost algorithm (van der Meer et al., 2007). In the simulations, we subsequently calculated from these radial responses, the radiated sound pressures. This is however difficult for the experimental results as the limited sampling rate is limited and stochastic errors in the microbubble diameter measurements occurred (Emmer et al., 2007b). We therefore estimated the scattered sound pressure using the following approach.

A simplified form of the radial response is $R = R_0 + Asin(\omega t)$, whereby $A << R_0$

and $\omega = 2\pi \cdot 3.75 \cdot 10^6$ rad/s. The second derivative with respect to time is $\ddot{R} = -A\omega^2 sin(\omega t)$. For low amplitudes, the velocity contribution of the microbubble wall in Eq (9.5) is small compared to the contribution of the acceleration and was therefore neglected. Combining the simplified radial responses with the simplified form of Eq (9.5) leads to

$$P_s = -\frac{\rho_l \omega^2 R_0^2 A sin(\omega t)}{r} \tag{9.6}$$

9.3 Results

9.3.1 Simulations

The responses of three types of microbubbles in an ultrasound field were simulated, which were free gas, elastic-coated and buckling-coated microbubbles. First, the results are compared when the microbubbles have only been insonified with 3.75 MHz (HF) (Fig 9.2). The elastic-coated microbubbles gave highest radial excursions for a microbubble size of 4.2 μm diameter (Fig 9.2a). This maximum indicates the resonant size at a transmit frequency of 3.75 MHz. The resonant size of the elastic-coated microbubbles was greater than that of the free gas microbubbles (2.0 μm) and in between these sizes, the resonant size of the buckling-coated microbubbles was found (2.6 μm).

Figure 9.2b shows the sound pressures that these microbubbles scattered. Microbubble sizes below the resonant size are in the Rayleigh regime of microbubble scattering. Well above resonance, scattering is dominated by the microbubble's physical cross-section and the backscattered sound intensity increases with the radius. Scattered sound pressures were elevated at resonance. Compared to the other microbubble types, the resonance peak of the buckling-coated microbubbles was leveled off and its maximum value was at a size greater than the size of the radial maximum, the maximum was found at 3.0 μm diameter.

Subsequently, the microbubble responses were simulated in a dual-frequency ultrasound field (0.5 and 3.75 MHz). For each type of microbubble, a size below, at and above resonance was selected. These sizes are indicated in Fig 9.2a. The left column of Fig 9.3 shows the resulting $D(t)$-data of the free gas microbubbles and in the right column corresponding power spectra are given. The influence of the 0.5 MHz pulse on the 3.75 MHz response was investigated by comparing the acoustic pressure field (Fig 9.3a) to the radial responses (Fig 3b-d).

In Fig 9.3b, it is observed that in the negative phase of the 0.5 MHz pulse, the free gas microbubble size increased, which resulted in an increased 3.75 MHz response. The microbubble size decreased in the positive phase of the 0.5 MHz pulse and also the amplitude of the 3.75 MHz response was decreased. The microbubble with a size above HF resonance showed opposite effects, a decrease in size resulted in an increased HF response and vice versa (Fig 9.3d). The power spectra have been normalized with respect to the response to the insonation frequency of 3.75 MHz. Significant side bands were observed at 3.25 and 4.25 MHz, and to a lesser extent also at 2.75 and 4.75 MHz.

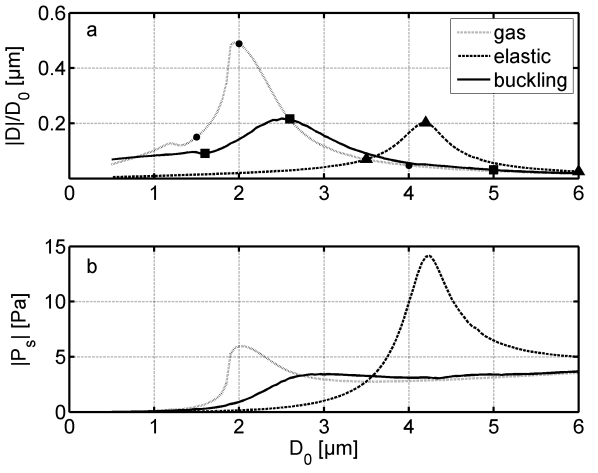

Figure 9.2: a) Simulated normalized radial responses, b) Scattered sound pressures as function of resting diameter using a single transmit frequency of 3.75 MHz. Dots (gas), triangles (elastic) and squares (buckling) indicate the selected microbubble sizes for the dual-frequency responses shown in Fig 9.3- 9.5.

These side bands result from nonlinear mixing of the LF and HF responses.

In Fig 9.4, the elastic-coated microbubbles showed similar responses compared to the free gas microbubbles albeit dampened because of the additional coating. The 0.5 MHz pulse pushes and pulls the microbubble size towards and away from the HF resonant size. Below the resonant size, a growth in size of the microbubble resulted in an increased HF response (Fig 9.4b) and above resonance, a growth in size resulted in a decreased HF response (Fig 9.4d).

The 0.5 MHz pulse had a modulating effect on the free gas and elastic-coated microbubbles that one would expect based on theory for a harmonic oscillator. However, the buckling-coated microbubbles showed opposite behavior (Fig 9.5). This was related to the compression-only behavior that was observed for these microbubbles. For all sizes in response to the 0.5 MHz pulse, the compression amplitude was larger compared to the expansion amplitude. The compression-only behavior influenced the radial modulation of the buckling-coated microbubbles. Below the HF resonant size, a negative phase of the 0.5 MHz did not result in an increase of microbubble size and did not result in an increased HF response (Fig 9.5b) as was observed for the free gas and elastic-coated microbubbles. On the contrary, highest HF responses occurred in the positive phase of the 0.5 MHz pulse when the microbubble was compressed. The HF response was smaller when the microbubble was expanded. For the microbubble insonified above resonance, the HF response seemed more equally distributed among expansion and compression

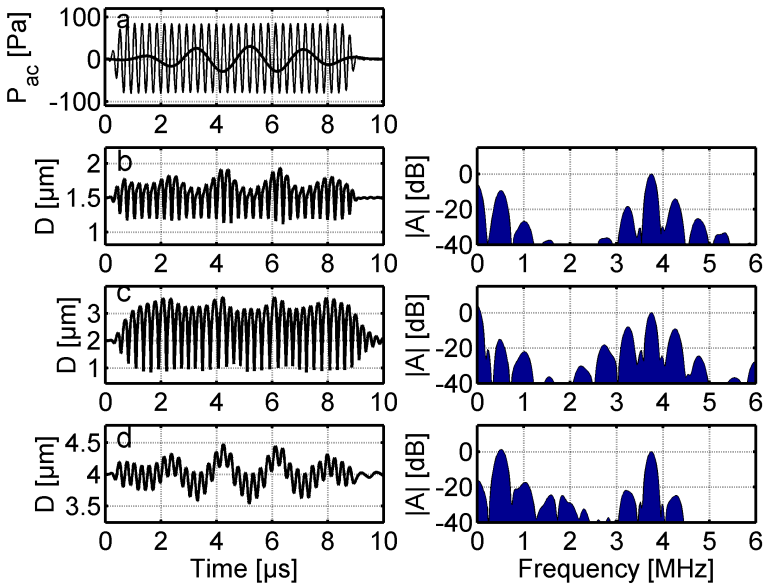

Figure 9.3: Simulated radial responses of free gas microbubbles with different resting sizes (left column b-d) and corresponding power spectra (right column b-d). a) acoustic pressure field, 0.5 MHz pulse (bold line) and 3.75 MHz pulse (thin line). b) D_0: 1.5 μm, c) D_0: 2.0 μm, d) D_0: 4.0 μm.

phase of the LF pulse (Fig 9.5d).

Subsequently, we calculated from the dual-frequency responses signals that could be detected in the radial modulation imaging technique. For each microbubble, two responses were calculated whereby the LF pulse was inverted. These two responses were high-pass filtered and subtracted to obtain the detection signals, see Fig 9.6. The free gas and elastic-coated microbubbles had maximum detection signals at their HF resonant sizes, which were 2.0 and 4.2 μm diameter at 3.75 MHz. The detection signal was also at a maximum at the HF resonant size for the buckling-coated microbubbles (3.0 μm diameter), but for these microbubbles also a significant detection signal was predicted above the HF resonant size. Detection signals of microbubble sizes above 5.0 μm diameter were larger compared to detection signals around resonance.

9.3.2 Experiments

The vibration of single phospholipid-coated microbubbles was recorded using a high-speed camera system. Figure 9.7 shows a scatter plot of the radial excursions and derived

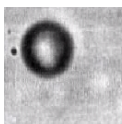

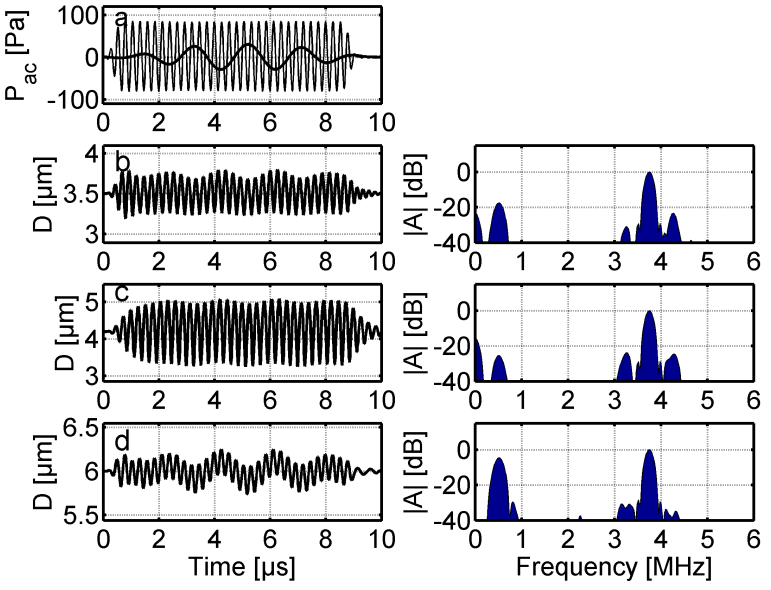

Figure 9.4: Simulated radial responses of elastic-coated microbubbles with different resting sizes (left column b-d) and corresponding power spectra (right column b-d). a) acoustic pressure field, 0.5 MHz pulse (bold line) and 3.75 MHz pulse (thin line). b) D_0: 3.5 μm, c) D_0: 4.2 μm, d) D_0: 6.0 μm.

scattered sound pressures of 78 microbubbles insonated with a single transmit frequency of 3.75 MHz. The responses of similarly sized coated microbubbles highly varied. Highest excursion amplitudes occurred for microbubbles with sizes between 2.0 and 3.0 μm diameter (Fig 9.7a). It was noticed that this agreed with the resonant size of the simulated buckling-coated microbubbles, which was 2.6 μm diameter. For a comparison, the results of the buckling-coated microbubbles have also been depicted in Fig 9.7.

Scattered sound pressures were calculated from the radial responses using Eq (9.6). Similar outcome is observed when the experimental results are compared to the simulated responses of the buckling-coated microbubbles. Highest scattered sound pressures occurred for microbubble sizes around 3.0 μm, which is greater than the radial maximum at 2.6 μm diameter and we observe also in the experimental results a leveled off maximum around 3.0 μm diameter.

Figure 9.8 shows the $D(t)$ responses and corresponding power spectra of four typical sizes. All microbubbles showed a response at the insonation frequency of 3.75 MHz. The smallest microbubbles of 1.7 and 2.2 μm diameter also responded at the second harmonic, which appeared at 4.6 MHz (instead of at 7.5 MHz), because of aliasing due

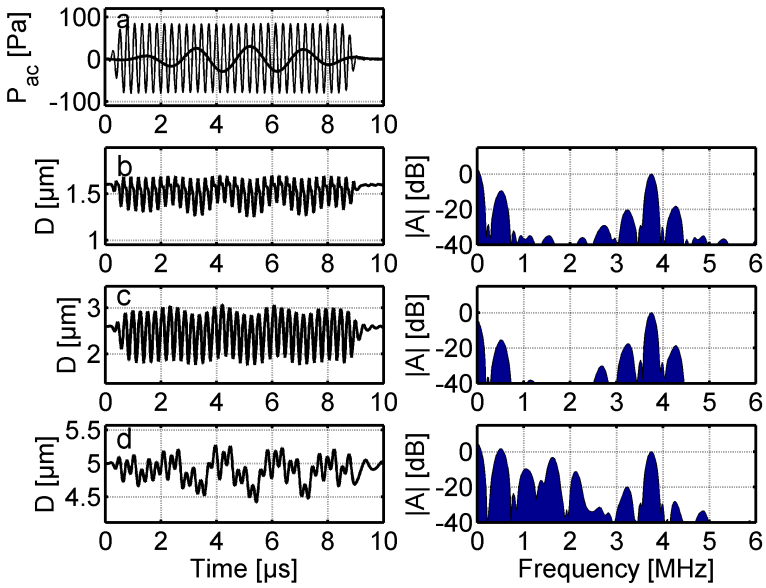

Figure 9.5: Simulated radial responses of buckling-coated microbubbles with different resting sizes (left column b-d) and corresponding power spectra (right column b-d). a) acoustic pressure field, 0.5 MHz pulse (bold line) and 3.75 MHz pulse (thin line). b) D_0: 1.6 μm, c) D_0: 2.6 μm, d) D_0: 5.0 μm.

to the sampling rate of 12.2 Mfps (Nyquist frequency of 6.1 MHz). The two largest microbubbles with sizes of 3.6 and 5.0 μm diameter generated a subharmonic response at 1.9 MHz.

Figure 9.9 shows the results of these microbubbles in a dual-frequency ultrasound field. First, we look into the response to the 0.5 MHz pulse. All microbubbles responded with a larger compression amplitude compared to the expansion amplitude. The two smallest microbubbles (1.7 and 2.2 μm diameter) did not show any expansion at all (Fig 9.9a and b), but also the two larger microbubbles (3.6 and 5.0 μm diameter) were more compressed than expanded (Fig 9.9c and d), *e.g.* for the 5.0 μm diameter microbubble the compression phase had an amplitude of 0.9 μm and the expansion phase 0.5 μm (Fig 9.9d).

In addition to the 0.5 MHz response, the microbubbles responded to the 3.75 MHz pulse. This HF response was highly modulated for the smallest microbubbles (1.7 and 2.2 μm diameter) and was fully located in the compression phase of the LF response. This effect of radial modulation was predicted by the simulated buckling-coated microbubble responses and this effect is opposite to the predictions by the more traditional approaches

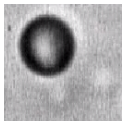

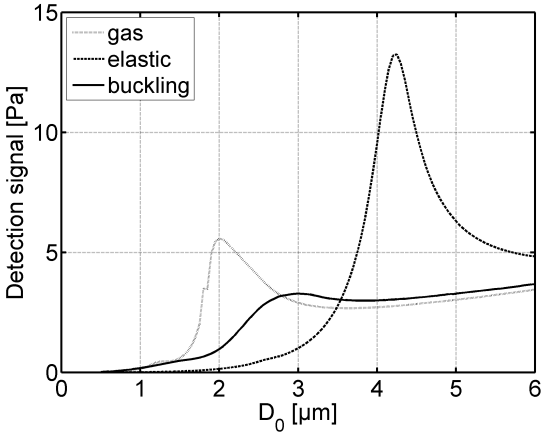

Figure 9.6: Simulations of the detection signal at 75 mm as function of resting diameter.

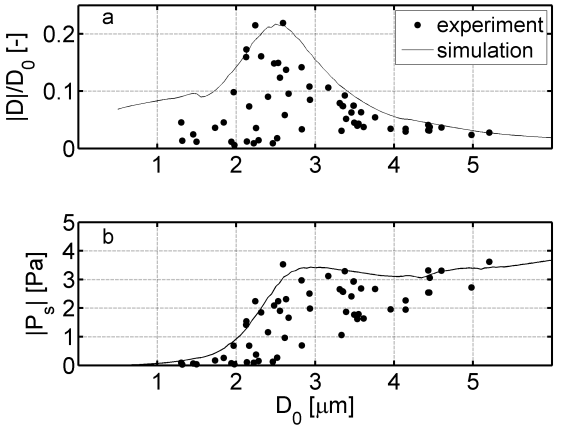

Figure 9.7: a) Normalized radial responses and b) scattered sound pressure at 75 mm as a function of resting diameter. Simulated results for buckling-coated microbubbles are included.

from the free gas and elastic-coated microbubbles. Corresponding power spectra show high sidebands at 3.75 $\pm$ n0.5 MHz ($n \leq 2$), indicating high nonlinear mixing between the 0.5 and 3.75 MHz responses. To a lesser extent, sidebands were observed for the 3.5 and 5.0 μm microbubbles.

It was also noticed that the smallest microbubble (1.7 μm diameter) had shrunk 13%

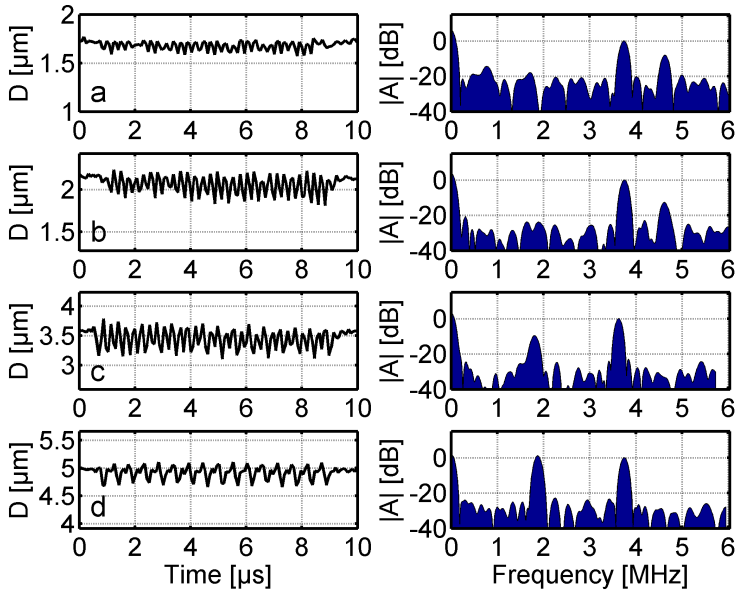

Figure 9.8: Phospholipid-coated microbubble responses at a single transmit frequency of 3.75 MHz, diameter-time curves (left column) and corresponding power spectra (right column) for microbubbles with different resting sizes: a) D0: 1.7 μm, b) D0: 2.2 μm, c) D0: 3.6 μm, and d) D0: 5.0 μm.

after two cycles of the LF pulse, subsequently the microbubble size stabilized and the microbubble stopped oscillating. The shrunken microbubbles are excluded from further study (21 microbubbles from a total of 78 microbubbles). Another observation concerned the subharmonic response of the 5.0 μm microbubble. Comparing Fig 8d with Fig 9d, it was observed that in the dual-frequency field, the subharmonic response had decreased 17 dB. The background of these observations is currently not understood.

Figure 9.10 shows the procedure to determine the amplitude modulation of the 3.75 MHz response by the 0.5 MHz pulse. As an example, the $D(t)$ curve of the microbubble with a size of 2.2 μm diameter was taken. The $D(t)$ curve was high-pass filtered to obtain the 3.75 MHz response only. Subsequently, the envelope was calculated using IQ demodulation. The modulation depth was determined using a subtraction of the maximum by the minimum value of the envelope, for this example resulting in an amplitude modulation depth of 0.36 μm.

In Fig 9.11 the amplitude modulation depths as a function of resting diameter are depicted for the whole population of recorded microbubbles. Microbubbles with sizes between 1.0 and 3.0 μm diameter were most affected by the LF pulse and showed highest

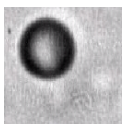

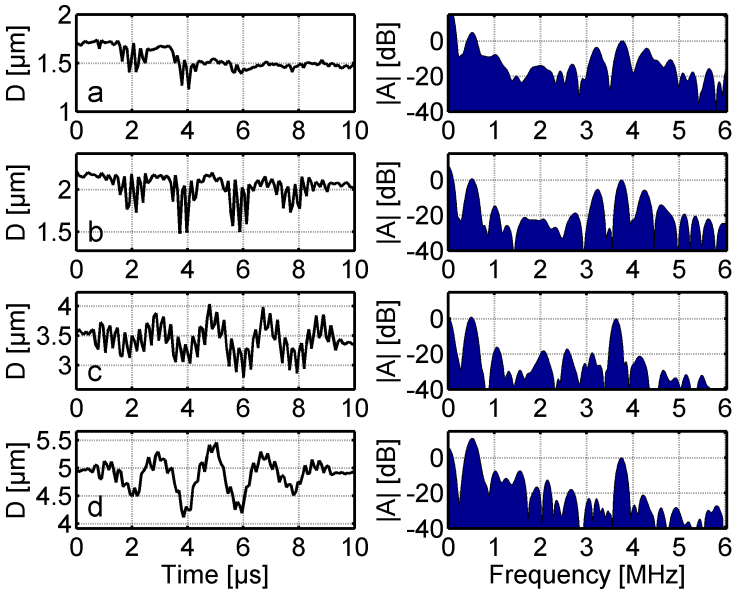

Figure 9.9: Phospholipid-coated microbubble responses in a dual-frequency ultrasound field (0.5 and 3.75 MHz), diameter-time curves (left column) and corresponding power spectra (right column) for microbubbles with different resting sizes: a) D0: 1.7 μm, b) D0: 2.2 μm, c) D0: 3.6 μm, and d) D0: 5.0 μm.

amplitude modulation values. The amplitude modulation depth decreased with size for microbubbles larger than 3.0 μm diameter. Microbubbles with a size of 5.0 μm hardly showed modulation effects.

The same procedure was followed to determine the amplitude modulation depths of the scattered sound pressures in the dual-frequency ultrasound field. Amplitude modulation had very different effects on the scattered sound pressures shown in Fig 9.12 compared to the radial responses shown in Fig 9.11. Whereas the amplitudes of the radial responses were most modulated for sizes between 1.0 and 3.0 μm diameter, we observed for the scattered sound pressure, highest amplitude modulation values for sizes greater than 3.0 μm diameter. It appeared that amplitude modulation of microbubble sizes larger than the resonant size resulted in higher scattered pressures compared to microbubbles at resonance.

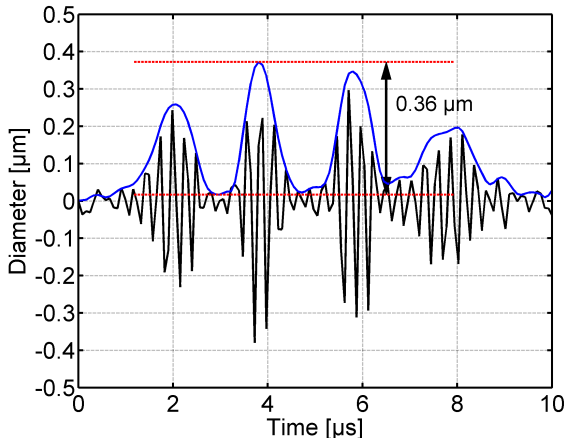

Figure 9.10: Illustration of procedure to determine amplitude modulation. The high-pass filtered radial (D) response of the 2.2 μm diameter from Fig 9.9 is shown.

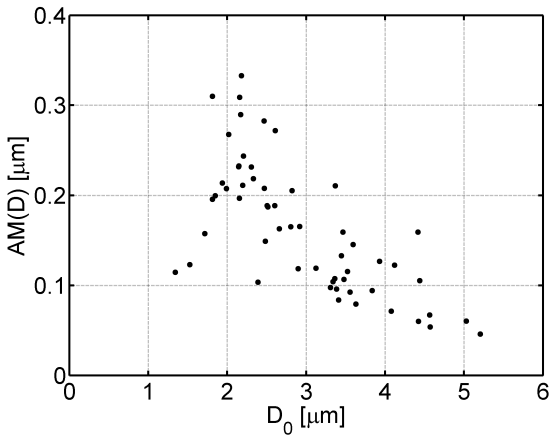

Figure 9.11: Amplitude modulation of diameter as a function of microbubble resting diameter.

9.4 Discussion and conclusions

The behavior of single microbubbles in a dual-frequency ultrasound field was studied using high-speed recordings and simulations. The two frequencies transmitted were 0.5 and 3.75 MHz. The 0.5 MHz pulse was used to modulate microbubble size, which resulted

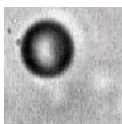

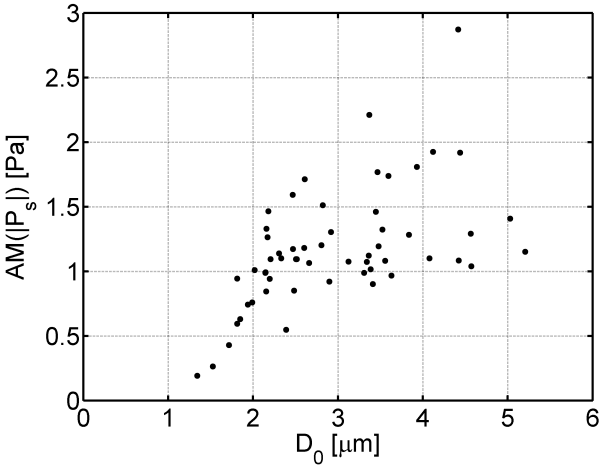

Figure 9.12: Amplitude modulation of scattered sound pressure at 75 mm as a function of microbubble resting diameter.

in an altered response to the 3.75 MHz pulse, compared to single 3.75 MHz frequency insonation. Obtained results are relevant for the background of the radial modulation imaging technique.

Previous studies on radial modulation imaging did not account for the influence of compression-only behavior on the radial modulation of coated microbubbles (Shariff et al., 2006a; Angelsen and Hansen, 2007; Bouakaz et al., 2007; Chérin et al., 2008; Måsøy et al., 2008). In this study, it appeared that the influence of the 0.5 MHz pulse depended on microbubble size and was strongly related to the occurrence of compression-only behavior. All microbubbles, independent of their size, showed an LF pulse response with a preference for compression compared to expansion. The smallest microbubbles with sizes between 1 and 3 μm showed strongest compression-only behavior and also highest amplitude modulation (see Figs 9.9 and 9.11). Moderate amplitude modulation was observed for microbubbles with sizes between 3 and 5 μm diameter and smallest modulation effects appeared for microbubbles of 5 μm diameter. We note that amplitude modulation of the radial responses should not be confused with the power modulation imaging technique, which is sometimes also referred to as amplitude modulation.

The influence of compression-only behavior was not observed in the optical recording shown by Bouakaz et al. (2007). The microbubble shown in this example had a size of 4 μm diameter and was according to our measurements insonified above resonance. Coating effects such as compression-only behavior are expected below resonance. Above resonance, inertia effects dominate (Sijl et al., 2008). In addition, the microbubble in Bouakaz et al. (2007) was insonified using higher acoustic pressures (120 and 180 kPa).

Following the paper by Marmottant et al. (2005), a large oscillation amplitude leads to rupture of the coating with the result that the microbubble behavior will resemble that of a free microbubble.

For the radial modulation imaging technique, the radiated pressure by the bubble is more important than the bubble's radial dynamics. Whereas in Fig 9.11 highest radial modulation is observed for microbubbles with sizes between 1 and 3 μm in diameter, it appears in Fig 9.12 that a high radial modulation does not necessarily result in a high detection signal. This is consistent with the simulated results for the buckling-coated microbubbles in Fig 9.6. In addition, a coated bubble at the HF resonant size does not produce best detectable signals in the radial modulation imaging technique (Fig 9.6 and 9.12). Highest detection signals for radial modulation imaging are obtained for microbubble sizes above the HF resonant size of 3.0 μm diameter.

This is explained by the influence of microbubble size on the scattered sound pressure. A large nonresonant microbubble can give a larger echo than a smaller microbubble at its resonant frequency, see also Newhouse and Mohana Shankar (1984). A low modulation of a high scattered sound pressure may overweigh a high modulation of a low scattered sound pressure. For example the radial amplitude modulation depth of the microbubble with a size of 2.2 μm diameter was 15% of its resting size and for the 5.0 μm diameter microbubble, this was only 1% of its resting size. Amplitude modulation depths of the scattered sound pressures were however 3.1 Pa for the 2.2 μm diameter microbubble and 8.2 Pa for the 5.0 μm diameter microbubble. It was therefore concluded that to obtain a high detectable signal, microbubble size is more effective than compression-only and resonance behavior.

Larger bubbles are more effective in a radial modulation imaging technique, but there is a trade-off between bubble size and the influence of the harmonic energy that the bubbles may generate. When the HF pulse is used for imaging and positioned as a short pulse in a longer LF signal, like in the methods suggested by Chérin et al. (2008); Måsøy et al. (2008); Shariff et al. (2006a), the HF pulse largely determines the image resolution, provided that the LF signals are filtered out. Chérin et al. (2008) explain that the resolution degrades when higher harmonic responses induced by the LF pulse are part of the detection signal. Higher harmonics induced by the LF pulse should therefore be avoided. Transmit frequencies, acoustic pressures and bubble sizes should be chosen such that significant modulation of the scattered sound pressures by the bubbles is generated without inducing LF resonant behavior by the bubbles.

We have seen that compression-only behavior promotes radial modulation, but compression-only behavior is not effective for the modulation of the scattered sound pressure. Instead of being an advantage for the radial modulation technique, compression-only behavior could negatively influence the image quality as it likely results in higher harmonic scattering. In our results, mixing between LF harmonics and HF responses could not be established. Possible complications should be investigated.

In this study, we have investigated radial amplitude modulation, but also the phase modulation of the HF responses could be investigated. We have tried to deduce phase information from the experimentally obtained D(t)-curves. However, the data appeared

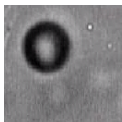

to be too noisy for a direct derivation of phase. We expect that microbubble size has similar effects on the phase modulation compared to the amplitude modulation of the microbubble radius and scattered pressure.

Previous studies concerning the radial modulation imaging technique based their conclusions on simulations using free gas or elastic-coated bubble models (Bouakaz et al., 2007; Angelsen and Hansen, 2007; Chérin et al., 2008). In this study, we have shown that observed dual-frequency behavior by phospholipid-coated microbubbles is best predicted using a model that includes compression-only behavior such as the full Marmottant model (Marmottant et al., 2005). We did not fit the outcome of the simulations by the Marmottant model to the experimental outcome in order to obtain coating parameters, because in this study we chose to investigate the radial modulation of coated microbubbles. Although the Marmottant model still has rather *ad hoc* regimes for the effective surface tension, the Marmottant model proved its functionality for this purpose.

10

Influence of phospholipid-coating composition on bubble vibration

Marcia Emmer, Alexander Klibanov, Annemieke van Wamel, and Nico de Jong

Abstract The nonlinear behavior of contrast agent microbubbles in an ultrasound field is exploited for medical imaging. This nonlinear behavior is generally expected at higher acoustic pressures, e.g. above 100 kPa. Previous studies have shown strong nonlinear behavior of phospholipid-coated microbubbles at low acoustic pressures. This were compression-only behavior whereby the compression amplitude of the radial response dominates the expansion amplitude and threshold behavior, which indicates that the microbubble does not show an onset to vibration with an oscillation amplitude that is linearly related to the acoustic pressure applied. Enhancing this nonlinear behavior is beneficial when using this behavior for imaging. We therefore investigated if coated microbubbles could be made such that these microbubbles showed increased compression-only and threshold behavior compared to that of a commercially available contrast agent. Different phospholipid-coating compositions were tested. The results showed no significant differences between the responses of the home-made phospholipid-coated microbubbles and the commercial contrast agent. The influence of resonant behavior and the occurrence of compression-only and threshold behavior were similar for all coating types. It is concluded that this similarity may be attributed to the PEG stearate that was present in all phospholipid-coatings. In future studies this should be further investigated.

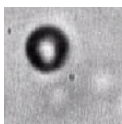

10.1 Introduction

Since the 1990s, commercial ultrasound contrast agents have been available to opacify the circulation in echographies of the human body (Goldberg et al., 2001). These agents consist of fluids with micrometer-sized gas-filled bubbles. The microbubbles are good ultrasound scatterers due to their large compressibility in comparison with the surrounding liquid. Under the influence of an ultrasound field, the microbubbles may vibrate linearly and nonlinearly. Nonlinear vibrations result in a backscattered signal containing higher harmonics of the incident frequency. Current contrast agent detection techniques typically exploit these harmonic signals.

A gas microbubble surrounded by liquid quickly dissolves due to excess pressure within the bubble, which is generated to balance the surface tension force. Even if a liquid is gas-saturated, the microbubble tends to dissolve (de Jong et al., 1991). To reduce this surface tension and thereby stabilizing the gas microbubble, current contrast agent microbubbles are coated. These coatings consist mainly of either an albumin, polymer or phospholipid (Bouakaz and de Jong, 2007).

It is well known that the coating has a large influence on the microbubble dynamics (Chatterjee and Sarkar, 2003; Church, 1995; de Jong and Hoff, 1993; Hoff et al., 2000; Khismatullin, 2004; Marmottant et al., 2005; van der Meer et al., 2007). Next to prolonging the existence of the microbubble, the coating increases the microbubble's stiffness and its damping, which results in a broader resonance peak at a higher frequency compared to the resonance peak of free gas microbubbles (Hoff et al., 2000; van der Meer et al., 2007). Other recently reported effects related to phospholipid-coatings are 'compression-only behavior' (de Jong et al., 2007) and 'threshold behavior' (Emmer et al., 2007b).

The term 'compression-only behavior' is used to describe the asymmetrical radial responses that were observed in high-speed recordings of single microbubbles (de Jong et al., 2007). The compression amplitude of these radial responses was more pronounced than the amplitude of the expansion phase. de Jong et al. (2007) employed a factor two difference between compression and expansion amplitude as a definition for compression-only behavior.

'Threshold behavior' refers to behavior observed at the onset of microbubble vibration (Emmer et al., 2007b). At low acoustic pressures, the bubble-liquid system is generally considered as a simple harmonic oscillator (Leighton, 1994). When an acoustic pressure is applied to such a linear system, this results in a response. In a previous study (Emmer et al., 2007b), it was observed that this does not hold for phospholipid-coated microbubbles. At a transmit frequency of 1.7 MHz, microbubbles with sizes smaller than 5.0 μm diameter did not show any oscillations before the acoustic pressure had exceeded a certain threshold value. These acoustic pressure threshold values ranged between 30 and 120 kPa (Emmer et al., 2007b) for the individual microbubbles.

Compression-only behavior as well as threshold behavior were explained by properties specific for phospholipid-coatings, such as the density of the phospholipids at the coating surface (Emmer et al., 2007b; Marmottant et al., 2005). A dense packing of the

phospholipid molecules leads to high intermolecular forces and a low surface tension. Microbubbles with such a tight packing are not easily expanded nor compressed, which explains threshold behavior. When sufficient acoustic pressure is applied, the coating buckles and the microbubble is compressed, which is observed as compression-only behavior.

Compression-only and threshold behavior are typically observed at low acoustic pressures. The nonlinear acoustic responses that result from this nonlinear behavior can be exploited to enhance the imaging of microbubbles at these low acoustic pressures (e.g. Emmer et al. (2007a,c)). Enhancing this nonlinear behavior could therefore be beneficial. An example of a coated microbubble that shows enhanced nonlinear behavior has been developed by Stride et al. (2008). They developed a microbubble that shows increased expansion by inhibiting the bubble compression with nanoparticles that are deposited on the bubble surface.

In this study, we investigate if compression-only or threshold behavior can be enhanced by manipulating the phospholipid composition of coated microbubbles. The responses of these microbubbles are compared to that of a commercially available contrast agent using high-speed camera recordings.

Phospholipids in the microbubble coating are usually from the class of phosphatidylcholines, which consist of a polar phosphocholine headgroup with two fatty acids, see Fig 10.1. Commercial contrast agents are mainly composed of fatty acids containing 16 or 18 carbon atoms (C16 and C18). We test the effect of increasing the chain length of the fatty acids. We expect that intermolecular forces between C22 phospholipids are higher compared to C16 phospholipids, and we hypothesize that coatings based on C22 have an increased stiffness compared to C16 based coatings.

In addition, the effect of additional hydrogen bonds is investigated. To obtain these extra hydrogen bonds, phosphatidylcholine is replaced by the phospholipid sphingomyelin. Like phosphatidylcholine, sphingomyelin also has a phosphocholine head group. This head group is, however, not connected to two fatty acids, but to a ceramide core. The ceramide core consists of sphingosine bonded to a fatty acid (Fig 10.1). It is expected that the additional amide group results in additional hydrogen bonds in the coating compared to phosphatidylcholine based coatings. Additional hydrogen bonds provide additional intermolecular forces and thus we also expect for sphingomyelin based coatings that these coatings are stiffer than coatings of a commercially available contrast agent bubble. Such an increased stiffness is expected to result in enhanced compression-only and threshold behavior, which is investigated in this study.

10.2 Materials and methods

The experimental contrast agents were prepared as is described briefly in Klibanov et al. (2004). We mixed saline with a phospholipid and PEG stearate (2 mg/ml PEG 6000 monostearate, Stepan Co., Northfield, Il, USA) and sonicated this mixture with a probe-type 20 kHz sonicator (XL2020, Misonix, Farmingdale, NY, USA). The coating was

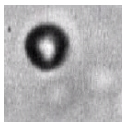

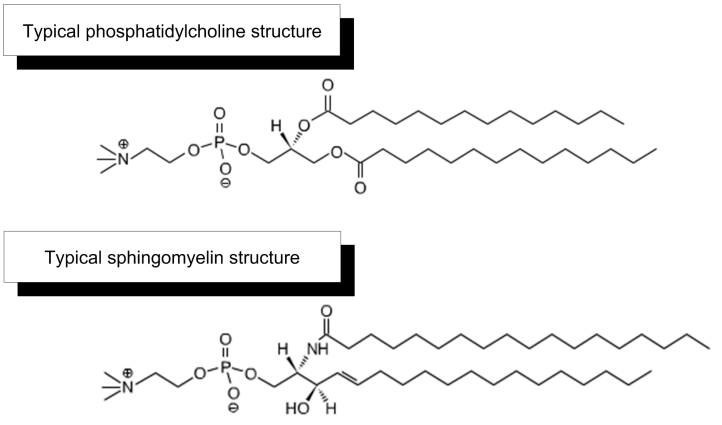

Figure 10.1: Molecular formulas of phospholipid structures.

composed of different phospholipids. We selected phosphatidylcholines with different carbon chain lengths (C16, C18, C20, and C22) and bovine brain sphingomyelin (SM) (Avanti Polar Phospholipids, Alabaster, AL, USA).

The gas core of the experimental contrast agents consisted of decafluorobutane gas. This was obtained by sparging decafluorobutane gas (Flura, Newport, AL, USA) through the phospholipid dispersion during sonication. Resulting microbubbles were dispensed in 2-ml vials with a decafluorobutane headspace, stored refrigerated and resuspended before use.

The responses of the experimental contrast agent microbubbles were compared with the responses of SonoVue®, which is a commercially available contrast agent that is approved for clinical use in Europe, China and South America. SonoVue contains sulphur hexafluoride microbubbles surrounded by a phospholipid coating (Schneider, 1999) (Bracco SpA, Milan, Italy). It was prepared as prescribed by the manufacturer.

The microbubbles were studied in an ultrasound field using a high-speed camera system (Fig 10.2). This high-speed camera system, the Brandaris 128, was built in house and is unique in the world (Chin et al., 2003). It is able to operate at 25 million frames per second (mfps). We used it at 13 mfps. The camera was connected to a microscope (Olympus Nederland BV, Zoeterwoude, The Netherlands), which magnified the microbubbles 240x (LUMPlan 60x water immersion objective and 2x2 magnifiers). The microbubbles were inserted in a cellulose Cuprophan® capillary tube (inner diameter 160 μm and outer diameter 200 μm, Akzo Nobel Faser AG, Wuppertal, Germany). The capillary tube was immersed in air saturated water in a water tank in which also the ultrasonic transducer was mounted. This transducer had a center frequency of 2.25 MHz, an aperture of 35 mm and was focused at the capillary tube (V397, Panametrics-NDTTM, Olympus NDT, Waltham, MA, USA). It was driven by an arbitrary waveform generator

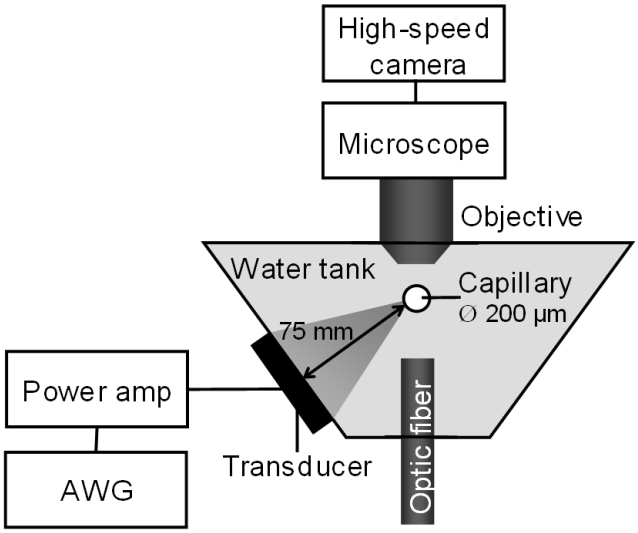

Figure 10.2: Scheme of the experimental setup for the optical recording of the microbubble vibrations. The ultrasound field is generated by the transducer connected to the power amplifier (Power amp) and arbitrary waveform generator (AWG).

(8026, Tabor Electronics Ltd., Tel Hanan, Israel) and power amplifier (150A100B, AR, Souderton, PA, USA).

The camera system recorded each microbubble in 12 sequences of 64 frames. Time between movies was 80 ms. Transmitted ultrasound consisted of cosine-gated six-cycle-sine waves with a center frequency of 1.7 MHz. In the first movie no US was applied. In the subsequent six sequences the acoustic pressure was increased from 10 to 80 kPa and in the last five sequences the acoustic pressure was decreased from 80 to 10 kPa. In this way, the effect of preceding ultrasound waves could be verified.

Diluted solutions of contrast agent microbubbles were inserted in the capillary tube such that only a few microbubbles were present in the image frame of 31x42 μm. For each microbubble, the diameter as a function of time was measured. Diameters were established using a minimal cost algorithm incorporated in custom written Matlab software (Mathworks Inc. Natick, MA, USA) as described by van der Meer et al. (2007).

To establish the acoustic pressure thresholds, which determine the threshold behavior of the microbubbles, we applied a method based on an earlier study (Emmer et al., 2007b). For this purpose, the response in the frequency domain was calculated and from this response the amplitude at the transmit frequency of 1.7 MHz was determined and plotted against each acoustic pressure applied. It was defined that microbubble oscillation could be assessed when the amplitude at 1.7 MHz was higher than twice the noise

level measured when no ultrasound was applied. Subsequently, we fitted a line through all oscillation amplitudes. The intercept of this line with the pressure-axis was determined. In case of a fully linear response, the intercept with the pressure-axis should be the origin. A positive value of the pressure-axis intercept indicates threshold behavior.

If microbubble oscillation could not be established for an acoustic pressure of 55 kPa or lower, the microbubble was excluded from this study, because it was decided that a line should be a fit through at least three amplitude values (11 microbubbles were excluded from a total of 209 microbubbles).

10.3 Results

The behavior of the optically recorded single microbubbles was characterized using three parameters: the microbubble oscillation amplitude, the ratio between microbubble expansion and compression (to determine 'compression-only behavior') and the pressure-axis intercept (to determine 'threshold behavior'). Recorded microbubbles were categorized according to their diameter and the results of each parameter were averaged for each category of microbubble size. The number of microbubbles in each category varied between 0 and 16 microbubbles.

To determine the oscillation amplitude of each radial response, the envelope of the diameter-time response was calculated using IQ-demodulation. The oscillation amplitude was the maximum value of this envelope. Fig 10.3 shows resulting oscillation amplitudes normalized to the resting diameter of each microbubble at an acoustic pressure of 80 kPa. Microbubble sizes of around 4.0 μm diameter responded with relatively highest oscillation amplitudes compared to other microbubble sizes, which indicates the resonant size of the microbubbles at an insonation frequency of 1.7 MHz. A resonant size of 4.0 μm diameter was observed for all types of phospholipid coatings.

Some microbubbles had a smaller size after ultrasound exposure compared to their initial size. Microbubbles that had shrunk over 15% in size were excluded from further study, which concerned 10 microbubbles from a total of 209 microbubbles.

Subsequently, the nature of the microbubble oscillations is regarded. For this purpose, the ratio between microbubble expansion (E) and compression (C) was determined, $E/C = |(D_{max} - D_0)/(D_{min} - D_0)|$. Figure 10.4 shows three typical examples of the radial responses of SonoVue microbubbles. The microbubble with a resting diameter of 2.0 μm shows typical compression-only behavior. The E/C ratio is 0.14. The microbubble with a resting size of 4.0 μm diameter had a more symmetrical radial response as is shown by the E/C ratio of 0.92. The E/C ratio of the radial response of the 6.0 μm-diameter microbubble was 0.41.

Figure 10.5 shows the average E/C ratio for each microbubble size for the whole population of measured microbubbles. For all types of phospholipid-coatings, lowest E/C ratios are found for the smallest microbubble size of 1.0 μm diameter. An E/C ratio below 0.5 fulfills the definition of 'compression-only behavior'. It is however observed that for all microbubble sizes the compression amplitude is larger than the ex-

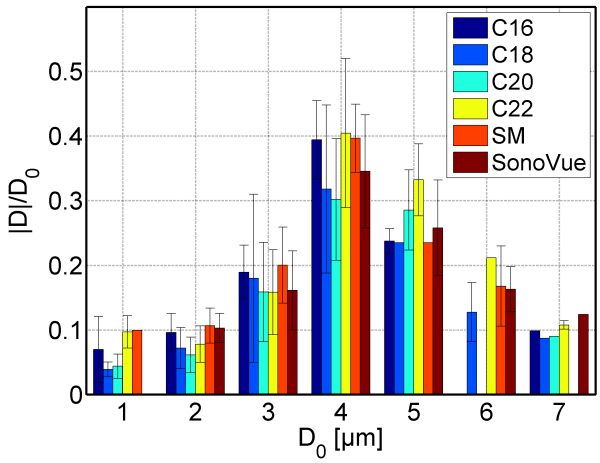

Figure 10.3: Normalized radial responses as function of microbubble resting diameter.

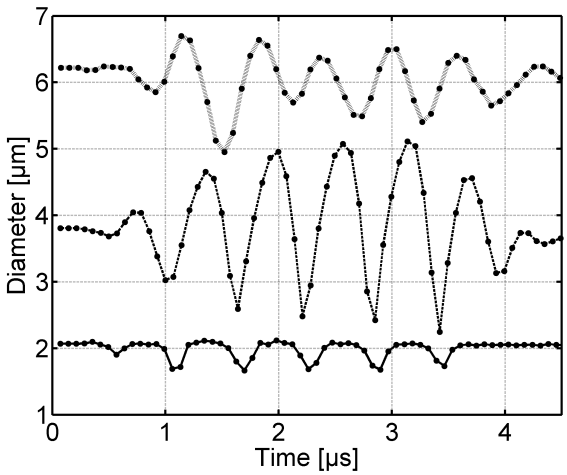

Figure 10.4: Radial responses of SonoVue microbubbles as function of time.

pansion amplitude, except for microbubbles of 5.0 μm diameter, which had an average E/C value of approximately 1.0, indicating a symmetrical diameter-time response. It appeared that the E/C ratio increased with bubble size for diameters between 1.0 and 5.0 μm and the E/C ratio decreased with bubble size for sizes above 5.0 μm diameter.

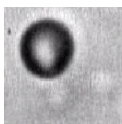

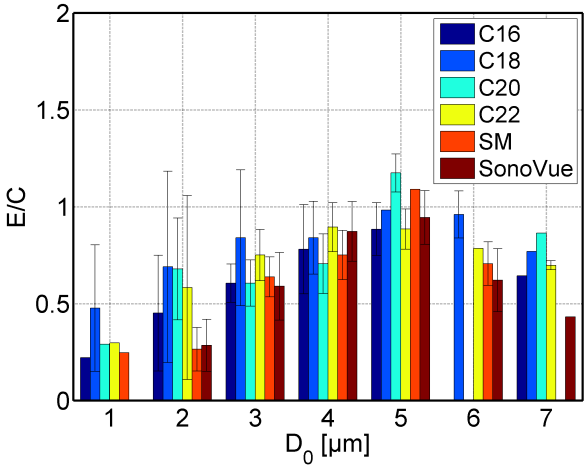

Figure 10.5: Ratio between expansion amplitude (E) and compression amplitude (C) as a function of microbubble resting diameter.

Furthermore, the onset of microbubble oscillation was investigated. The method to determine the acoustic pressure thresholds is explained in the methods section. Figure 10.6 shows the responses as a function of acoustic pressure from the SonoVue microbubbles that were also depicted in Fig 10.4. The intercepts with the pressure-axis of the linearly fitted oscillation amplitudes are indicated. These intercepts represent the acoustic pressure thresholds. The microbubbles with sizes of 2.0 and 4.0 μm diameter both show threshold behavior with intercept values of 18 and 22 kPa, respectively. The pressure-axis intercept of the largest microbubble shown (size of 6.0 μm) was -27 kPa. This microbubble did not show threshold behavior, but also in this case, the oscillation amplitude values did not increase fully proportional to the acoustic pressure applied, which resulted in a negative pressure-axis intercept.

Figure 10.6 shows the responses to the increasing acoustic pressure as well as the responses to the decreasing acoustic pressure. The microbubbles with sizes of 2.0 and 6.0 μm diameter appeared to behave the same for both directions of the acoustic pressure. The 4.0 μm diameter microbubble responded with different amplitudes when the acoustic pressure was decreased, whereby it must be noted that in contrast to the other microbubbles, the size of this microbubble had decreased from 4.0 μm to 3.5 μm after being exposed to the series of insonations ($\approx 13\%$).

The average pressure-axis intercepts for each category of microbubble size are shown in Fig 10.7. For all types of phospholipid-coatings, it was observed that the pressure-axis intercepts for microbubble sizes up to a diameter of 4.0 μm diameter were positive, which indicates that these microbubbles showed 'threshold behavior'. Microbubble sizes

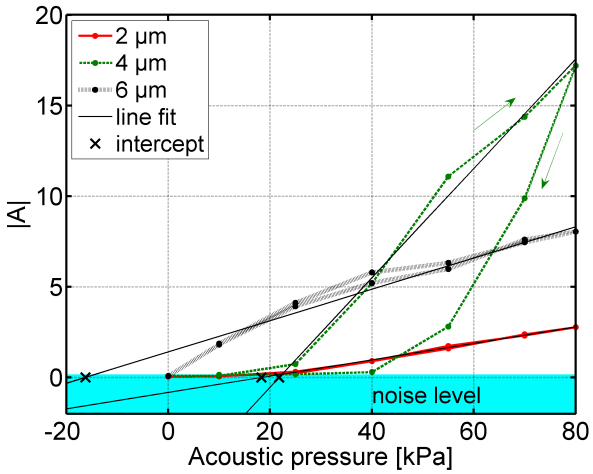

Figure 10.6: Magnitude of radial response as function of acoustic pressure applied.

of 5 μm diameter and above had negative pressure-axis intercepts.

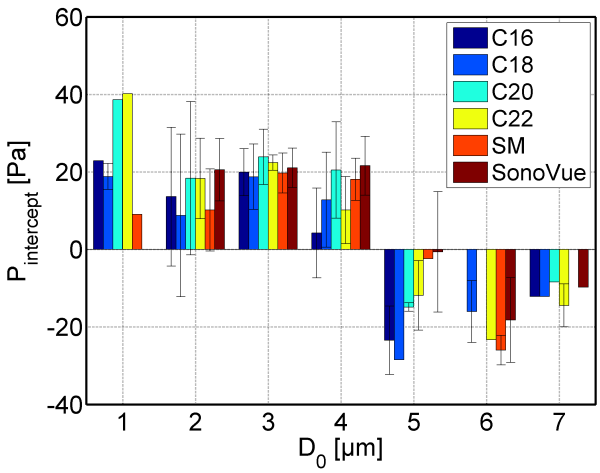

Figure 10.7: Pressure-axis intercepts as a function of microbubble resting diameter.

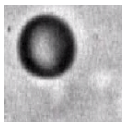

10.4 Discussion and conclusions

Nonlinear behavior of contrast agent microbubbles such as compression-only and threshold behavior is beneficial for contrast agent imaging at low acoustic pressures. We investigated if this nonlinear behavior can be enhanced by adapting the composition of the phospholipid-coating.

Unfortunately, we did not observe significant differences in behavior between microbubbles with different phospholipid-coating compositions. Independent of the coating composition, all microbubbles had a resonant size of approximately 4.0 μm diameter and showed compression-only and threshold behavior for sizes below and at resonance. There appears to be a large intravariability within each group of microbubble size, which is explained by the inhomogeneous character of the coating (Borden et al., 2004; Kim et al., 2003). This intravariability also appeared for example in Fig 9.7.

The different compositions of phospholipid-coatings have one similarity, they all contain PEG stearate. PEG stearate enhances the stability of the coatings. It could be that the influence of PEG stearate dominated the other effects such as the hypothesized influences of a longer acyl chain length or additional hydrogen bonds on the stiffness of the bubble coating. Future plans therefore include composing phospholipid-coated bubbles without PEG stearate to investigate if in this way nonlinear behavior at low acoustic pressures of coated bubbles can be enhanced.

Before this research, the strong relationship between bubble size and nonlinear bubble behavior was not shown for this large number of investigated microbubbles. It appears that compression-only behavior ($E/C < 0.5$) as well as threshold behavior ($P_{intercept} > 0$ kPa) only occur for bubble sizes below and at resonance (Figs 10.5 and 10.7). Sijl et al. (2008) have recently shown that below resonance, the bubble responses are dominated by the coating, whereas above resonance, inertia dominates and the response of the coated bubble resembles that of a free gas bubble. This is consistent with the hypothesis that compression-only and threshold behavior result from the influence of the coating on the bubble's response (Marmottant et al., 2005; de Jong et al., 2007; Emmer et al., 2007b).

In Fig 10.5, we do see E/C values smaller than 1.0 for bubble sizes above 5.0 μm diameter, but the nature of the oscillations of these large microbubbles is different from what we have termed 'compression-only behavior'. This becomes clear when Fig 10.6 is regarded. The 6.0 μm diameter bubble has according to the definition an E/C value smaller than 1.0, but it shows clearly an expansion phase, which is different from the diameter-time response of the 2.0 μm diameter bubble.

Figure 10.7 shows that the acoustic pressure threshold values are not related to microbubble size as was also observed in previous work (Fig 5.6) (Emmer et al., 2007b). Figure 10.6 shows that the threshold pressure of the resonant microbubble with a size of 4.0 μm is even a little higher than that of the microbubble of 2.0 μm diameter.

This resonant microbubble in Fig 10.6 is furthermore interesting, because it shows the influence of microbubble shrinkage on threshold behavior, which agrees with our hypothesis concerning the background of threshold behavior (Emmer et al., 2007b). Af-

ter the second series of decreasing acoustic pressure (80-10 kPa), the acoustic pressure threshold value appeared to be higher than during the first series of insonation (10-80 kPa). It is believed that this is explained by the high oscillation amplitude of this resonant microbubble at 70 and 80 kPa, which caused gas release from the gas core of the bubble. The gas release resulted in an increased concentration of phospholipids at the bubble's surface and as a result the coating stiffness increased (Marmottant et al., 2005). This increased stiffness inhibited the oscillation amplitude at the second series of insonation with the result that the acoustic pressure threshold value was lower.

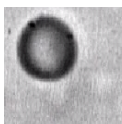

11 Discussion and conclusions

11.1 Discussion

In this thesis, we investigated the behavior of coated microbubbles in an ultrasound field. In the quest for answers, some aspects came forward. These aspects are good starting points for further research and are therefore identified in this section.

11.1.1 Clinical relevance compression-only and threshold behavior

Compression-only (chapter 4) and threshold behavior (chapter 5) are relevant for low-MI imaging techniques that are used in clinical applications. The advantage of using low acoustic pressures is that the microbubbles are not destroyed so readily, permitting continuous real-time imaging.

We have shown in chapter 7 and 8 of this thesis that threshold behavior can be exploited in a power modulation imaging technique. In chapter 9, compression-only behavior appeared to be relevant for radial modulation imaging although it does not seem to enhance this technique. We did not further investigate the use of compression-only behavior in an imaging technique. It is expected that this highly nonlinear behavior results in highly nonlinear acoustic responses, which is supported by the observation of increased harmonic energy for filtered microbubble suspensions in chapter 6 (Fig 6.7). Imaging techniques that exploit harmonic energy such as second harmonic imaging (Schrope and Newhouse, 1993), pulse inversion (Hope Simpson et al., 1999), and power modulation (Brock-Fisher et al., 1996) are expected to benefit from compression-only behavior.

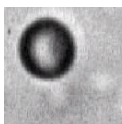

In addition, it is commented that current imaging techniques probably have already profited or suffered from compression-only or threshold behavior. We expect that many researchers must have observed unexpected high signals after signal processing while the acoustic pressure was expected to be in the linear regime of microbubble oscillation.

Futhermore, it is noted that the experiments described in this thesis were all performed *in vitro*, which means that it was in a controlled environment in the laboratory. The influence of the human blood circulation on compression-only and threshold behavior is not known and should be investigated in future research.

11.1.2 New approaches for coated microbubble modeling

The ultimate coated bubble model has not been developed yet (chapter 2). To achieve improvements on coated bubble modeling, we first should abandon the idea of an ultimate model. It should be focused on the specific characteristics of the ultrasound contrast agent considered. For example a phospholipid-coating has very different properties compared to a polymeric shell. Moreover, it should be taken into account that microbubbles within a population of a contrast agent can have different properties. Figure 9.7 shows that even such an important parameter as the resonance frequency has a statistical character and that microbubbles of equal sizes can show different responses. Thus models will always have a sort of general character.

This thesis has shown that in order to model a phospholipid-coated microbubble, compression-only and threshold behavior need to be taken into account. Recently, three models have done so, which are the models by Marmottant et al. (2005), Stride (2008), and Tsiglifis and Pelekasis (2008). The difference between these models and previous models is that in these models the coating does not have fixed properties (chapter 2). The coating parameters are defined as variables that change with the bubble radius. Tsiglifis and Pelekasis (2008) used for this purpose a constitutive law and Marmottant et al. (2005) and Stride (2008) defined a relationship between the coating surface area and the coating properties. These models can be further improved and need to prove themselves. However, they have shown that to model phospholipid-coated microbubble behavior, dynamical coating parameters should be included.

11.1.3 Recent developments on threshold behavior

Tsiglifis and Pelekasis (2008) investigated the effect of an increasing acoustic pressure on the bubble response predicted by their model. One of their results (Fig 4) shows a sudden increase in oscillation amplitude. The bubble showing this behavior was modeled using a neo-Hookean law for the coating ($b = 0$). When the acoustic pressure exceeded 400 kPa, the oscillation amplitude increased abrupt from $\Delta D/D_0 = 1$ to $\Delta D/D_0 = 3$. Also when a Kelvin-Voigt constitutive equation was applied, which ignores material nonlinearity, such a sudden increase in oscillation amplitude was obtained by Tsiglifis and Pelekasis (2008).

Tsiglifis and Pelekasis (2008) explain that the reason for this abrupt increase in oscillation amplitude (which they call threshold behavior) is the change of resonant frequency with sound amplitude. The microbubble showing this behavior is first driven below resonance. As the amplitude of sound increases, the resonant frequency of this microbubble decreases, until the resonant frequency hits the driving frequency. Then an intense bubble response is obtained. This effect also occurs without the presence of a nonlinear material law, because inertia can have the same effect. For an increasing nonlinear oscillation, the influence of inertia becomes more important and this also results in a decrease in resonant frequency. A nonlinear material law can amplify this effect of decreasing resonant frequency.

When comparing Fig 4 from the paper by Tsiglifis and Pelekasis (2008) with Fig 5.5 from this thesis, it appears that there is an order difference between simulated results by Tsiglifis and Pelekasis (2008) and the experimental results shown in this thesis. Tsiglifis and Pelekasis (2008) observe an abrupt increase in oscillation amplitude at a much higher acoustic pressure and for much higher oscillation amplitudes. This abrupt increase in oscillation amplitude occurs when the microbubble has already been oscillating with large amplitude ($\Delta D/D_0 = 1$) and the nature of these oscillations are most likely highly nonlinear. This is different from the data presented in Fig 5.5. Here, threshold behavior was observed for oscillation amplitudes ($\Delta D/D_0$) between 0 and 0.05.

We do however believe that threshold behavior is accompanied by a decrease of the bubble resonant frequency. Recently, Overvelde et al. (2008) have shown this decrease in resonant frequency applying 'the Marmottant model' and demonstrated threshold behavior at acoustic pressures 7-25 kPa. These acoustic pressure threshold values seem to be more consistent with our experimental observations.

It is noted here that a decrease in resonant frequency at an increasing acoustic pressure is not the origin of threshold behavior, but it is threshold behavior itself. The origin of threshold behavior is explained by changing properties of the bubble's coating as a result of an increasing osillation amplitude (chapter 5).

Marmottant et al. (2005) has modeled such coating properties by defining an effective surface tension. The effective surface tension in this model depends on the state of the coating and can be in three different regimes, which are the buckling regime, the linear elastic regime and the ruptured regime. The coating of a microbubble in the linear elastic regime is stiffer than that of a microbubble in the buckling or ruptured regime. Because the resonant frequency of a system increases with an increasing stiffness of the system, it follows that the resonant frequency of a microbubble in the elastic regime is higher than that of a microbubble in the other regimes. Threshold behavior is then described as follows. A microbubble in rest is insonified below resonance. By increasing the acoustic pressure the state of the microbubble coating can change from the linear elastic regime to the buckling and ruptured regimes. In the buckling and ruptured regimes, the oscillation amplitude is less dampened and the resonant frequency of the microbubble decreases with the result that the oscillation amplitude increases.

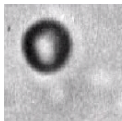

11.1.4 Linear and nonlinear regimes

It is appreciated in chapter 2 that the development of theoretical descriptions of coated bubble dynamics in most cases resulted in a study in the linear regime or at least the shell parameters were derived in the linear regime. 'Linear' and 'nonlinear regime' are frequenly used indications that go without reference. Conditions for the ultrasound field which yield a linearly oscillating coated microbubble cannot be found in literature. A frequently mentioned guess is that the acoustic pressure should not exceed 50 or 100 kPa (see for example Becher and Burns (2000); Deng and Lizzi (2002); Blomley et al. (2007); Goldberg et al. (2001); O'Brien (2007)). The observations of 'compression-only' and 'threshold behavior' by coated microbubbles offer a different perspective to the linear regime as both observations were done at acoustic pressures below 50 and 100 kPa. In future research, assumptions concerning linear behavior of coated microbubbles should be further substantiated.

A common way to substantiate the linear regime is following the definition for the nonlinear regime. The nonlinear regime starts at the first acoustic pressure whereby nonlinear microbubble oscillations are observed. These oscillations are automatically large amplitude oscillations. Thus all acoustic pressures below the nonlinear regime result in linear small amplitude oscillations. This approach was followed in the studies byMarmottant et al. (2005) and Tsiglifis and Pelekasis (2008). Here we philosophize a bit further on the value of regarding microbubble oscillations in the linear regime.

Based on our observations on compression-only and threshold behavior, we can define two different categories of microbubbles. In the first category we find microbubbles that are insonified above their resonance frequency. For these microbubbles neither 'compresssion-only' nor 'threshold behavior' is expected and we observe a linear relationship between acoustic pressure and oscillation amplitude. However, the negative threshold pressure values that are found for these bubbles indicate that this relationship is not perfectly linear. The amplitudes appeared to increase less than proportional to the acoustic pressure (see Fig 5.5 and 10.6). This trend is visible from the first acoustic pressure that we measured, which was 10 and 20 kPa. Thus the linear regime must be found somewhere below these acoustic pressure values, which is lower than acoustic pressures generally used in clinical applications.

In the second category, microbubbles are insonified below their resonance frequency and these microbubbles do show compresssion-only and threshold behavior. In chapter 5, it was observed that many microbubbles show both threshold behavior and compression-only behavior. When these microbubbles were observed to start oscillating, the compression amplitudes of these oscillations were larger than the expansion amplitudes. Following above mentioned definition of nonlinear behavior, these microbubbles were observed to start oscillating with large amplitude oscillations. In Fig 5.5, it can be observed that these 'large' amplitudes had values normalized to the resting diameter of approximately 0.05 ($\Delta/D_0 < 0.05$), which is generally considered to be well within the linear regime. Unfortunately, we could not establish if microbubbles showing threshold behavior were oscillating below the threshold pressure. It is an interesting question for further

research whether these microbubbles oscillate linearly below the threshold value or that they do not oscillate linearly at all. It is however concluded that for microbubbles showing compression-only and threshold behavior the linear regime is not relevant to predict behavior at clinically applied acoustic pressures.

11.1.5 Microbubble shrinkage

Another important aspect in this thesis is microbubble shrinkage. This shrinkage may occur before or while the microbubbles are insonated with ultrasound. First, shrinkage before insonation is considered. In contrast to shrinkage occuring while the microbubble is being insonated, this shrinkage was not observed, but it is part of a hypothesis to explain compression-only and threshold behavior. In chapter 3, it was hypothesized that microbubble shrinkage is connected to aging of the microbubbles. Over time, gas difuses from the microbubble gas core into the surrounding liquid. As the gas core shrinks, the phospholipid molecules are compressed towards each other, resulting in a decreased surface tension between the gas core and the surrounding liquid, which inhibits further gas diffusion such that the microbubble does not disappear. A microbubble with such a compressed phospholipid coating is expected to show compression-only and threshold behavior (see chapter 4 and 5).

At the time of the paper by Marmottant et al. (2005), it was assumed that the process of gas diffusion took hours, which was inspired by the claim of the manufacturer that the contrast agent SonoVue should not be used after six hours after reconsitution of the vial (Schneider, 1999; Bokor, 2000). In chapter 9 and 10, only 'fresh' microbubbles were investigated and compression-only behavior was also observed within minutes after reconstitution of the contrast agent vial. Without the application of ultrasound we did not observe shrinkage under the microscope during the high-speed camera experiments. It is furthermore remarkable that even more than a year after reconstitution of the vial, contrast agent microbubbles are found in the vial and can be used for testing. Currently, we do not fully understand these observations. To explain phenomena as compression-only and threshold behavior, we should increase our knowledge concerning the process of coated microbubble formation and subsequent development of the microbubble, such as the time scales for gas diffusion into the liquid and the consequences for the phospholipid-coating.

Another case is the observation of microbubble shrinkage during insonation in the high-speed camera recordings. We mostly excluded these microbubbles from the results as is indicated in the text. These shrinking microbubbles were either insonified at their resonance frequency and oscillated with high amplitude or they were smaller than approximately < 2 μm in diameter (see for example Fig 9.9) and oscillated with a relatively small amplitude. In the case of a resonant microbubble, the high amplitude causes a rupture of the coating and gas is able to diffuse into the surrounding liquid. Hereby it must be noted that this rupture does not necessarily lead to the destruction of the microbubble such as with hard-shelled polymer microbubbles (Bouakaz et al., 2005). In many cases, the microbubble continues oscillating with a smaller size.

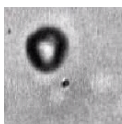

Microbubbles smaller than < 2 μm diameter were often observed to disappear after rupture, but it also was observed that shrinkage stopped when the bubble reached some size. Figure 9.9 is an interesting example of such a bubble. Under insonation, this bubble oscillated and shrunk and suddenly ceased shrinking and oscillating at a certain size. The ceasing of the oscillations may be threshold behavior, but it is not understood why these microbubbles loose gas, whereas a bit larger microbubbles do not show this gas release. These observations are interesting for further research.

11.2 Conclusions

Ultrasound contrast agents are great tools to visualize blood in the human body. Their properties are exploited in several diagnostic imaging techniques and more and more their main constituent, the coated microbubble, is used in different therapeutic applications.

In this thesis, the behavior of the coated microbubble in an ultrasound field was studied. It is fascinating to see that such a simple concept as a coated gas microbubble can do so many things in an ultrasound field. It is also fascinating to reduce all of these observations to the execution of a few physical laws. What have we learned in this thesis?

At the onset of the vibration of a gas bubble, there is a linear relationship between the vibration amplitude and the acoustic pressure applied. Adding a coating to the microbubble changes this relationship. Threshold behavior was observed for microbubbles with sizes smaller than 5.0 μm in diameter at a transmitted frequency of 1.7 MHz. These microbubbles were not observed to oscillate before the acoustic pressure had exceeded values between 30 and 120 kPa for the individual bubbles. This is comparable with the situation of a stationary box positioned on the ground. A box does not start to move before the static friction has overcome.

At the onset of vibration for coated microbubbles, the relationship between vibration amplitude and acoustic pressure applied is not always linear, neither is the shape of the radial oscillations at low acoustic pressures. Previously, it was assumed that at acoustic pressures as low as 50 kPa the compression amplitude equals the expansion amplitude. When the acoustic pressure is increased, especially the expansion amplitude grows, because the compression of the microbubble is limited. In this thesis, compression-only behavior of the coated microbubbles was described. At acoustic pressures from 20 to 200 kPa, we observed asymmetrical radial excursion whereby the compression amplitude was at least a factor of two greater than the expansion amplitude.

Threshold behavior and compression-only behavior are explained using properties specific for phospholipid-coatings, such as the density of the phospholipid molecules on the surface of the coating.

Threshold behavior and compression-only behavior are relevant for imaging at low acoustic pressures. It has been shown in this thesis that threshold behavior can be utilized for clinical application in a power modulation imaging technique. It is also expected that compression-only and threshold behavior have implicitly already been exploited in current imaging methods based on nonlinear contrast agent responses.

The imaging of contrast agent microbubbles could be further improved when the phospholipid-coatings of these microbubbles are modified such that threshold or compression-only behavior are further enhanced. This thesis reports first results from such modifications to the composition of phospholipid-coated microbubbles.

Gained knowledge presented in this thesis has been implemented in theoretical descriptions of coated microbubble dynamics. The first attempt to model specifically a phospholipid-coated microbubble is included in this thesis and is able to predict compression-only behavior (Marmottant et al., 2005). Since then other models which also aim at predicting compression-only and threshold behavior have followed (Stride, 2008; Tsiglifis and Pelekasis, 2008). Phospholipid-coated microbubble models still need to be improved, which shows that we will have to continue our research on the behavior of phospholipid-coated microbubbles in an ultrasound field.

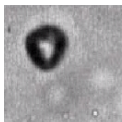

References

J.S. Allen and M.M. Rashid. Dynamics of a hyperelastic gas-filled spherical shell in a viscous fluid. *J Appl Mech*, 71:195–200, 2004. 2.6.7, 2.7

B.A.J. Angelsen and R. Hansen. Surf imaging - a new method for ultrasound contrast agent imaging. In *Proc IEEE Ultrasonics Symposium*, pages 531–541, 2007. 9.1, 9.4

D. Barthès, A. Diaz, and E. Dhenin. Effect of constitutive laws for two-dimensional membranes on flow-induced capsule deformation. *J Fluid Mech*, 460:211–222, 2002. 2.6.12

H. Becher and P.N. Burns. *Handbook of contrast echocardiography: LV function and myocardial perfusion*. Springer-Verlag, Berlin, 2000. 1.3, 7.1, 11.1.4

M. Blomley, M. Claudon, and D. Cosgrove. WFUMB safety symposium on ultrasound contrast agents: clinical application and safety concerns. *Ultrasound Med Biol*, 33(2):180–186, 2007. 1.2.1, 1.3, 1.4, 1.4, 11.1.4

D. Boal. *Mechanics of the cell*. Cambridge University Press, Cambridge, 2002. 3.5

D. Bokor. Diagnostic efficacy of sonovue. *Am J Cardiol*, 86(suppl):19G–24G, 2000. 11.1.5

M.A. Borden and M.L. Longo. Dissolution behavior of lipid monolayer-coated, air-filled microbubbles: Effect of lipid hydrophobic chain length. *Langmuir*, 18:9225–9233, 2002. 3.1, 3.3.2

M.A. Borden, G. Pu, G.J. Runner, and M.L. Longo. Surface phase behavior and microstructure of lipid/peg-emulsifier monolayer-coated microbubbles. *Colloids and Surfaces*, 35:209–223, 2004. 5.4, 10.4

A. Bouakaz and N. de Jong. WFUMB safety symposium on echo-contrast agents: nature and types of ultrasound contrast agents. *Ultrasound Med Biol*, 33(2):187–196, 2007. 10.1

A. Bouakaz, S. Frigstad, F.J. Ten Cate, and N. de Jong. Super harmonic imaging: a new imaging technique for improved contrast detection. *Ultrasound Med Biol*, 28:59–68, 2002. 4.1

A. Bouakaz, M. Versluis, and N. de Jong. High-speed optical observations of contrast agent destruction. *Ultrasound Med Biol*, 31(3):391–399, 2005. 1.3, 5.1, 5.2.2, 6.4, 11.1.5

A. Bouakaz, M. Versluis, J. Borsboom, and N. de Jong. Radial modulation of microbubbles for ultrasound contrast imaging. *IEEE Trans Ultrason Ferroelectr Freq Control*, 54(11):2283–2290, 2007. 4.4, 9.1, 9.4

M.P. Brenner, S. Hilgenfeldt, and D. Lohse. Single-bubble sonoluminescence. *Rev Mod Phys*, 74 (2):425–484, 2002. 2.4, 3.2.2

G.A. Brock-Fisher, M.D. Poland, and P.G. Rafter. *Means for increasing sensitivity in non-linear ultrasound imaging systems*. US patent no 5577505, 1996. 1.3, 6.1, 6.4, 9.1, 11.1.1

P.N. Burns, T. Wilson, and D. Hope Simpson. Pulse inversion imaging of liver blood flow: An improved methode for characterization of focal masses with microbubble contrast. *Invest Radiol*, 35(1):58–71, 2000. 4.1, 4.4

S. Casciaro, R.P. Errico, F. Conversano, C. Demitri, and A. Distante. Experimental investigations of nonlinearities and destruction mechanisms of an experimental phospholipid-based ultrasound contrast agent. *Invest Radiol*, 42(2):95–104, 2007. 6.1, 6.4

C. Caskey, D. Kruse, P. Dayton, and K. Ferrara. On the oscillations of microbubbles in tubes with diameters as small as 12 microns. *IEEE Ultrason Symp*, pages 854–857, 2005. 5.4

D. Chatterjee and K. Sarkar. A newtonian rheological model for the interface of microbubble contrast agents. *Ultrasound Med Biol*, 29(12):1749–1757, 2003. 2.6.6, 2.6.6, 2.6.8, 2.6.8, 2.6.9, 2.7, 3.2.2, 10.1

D. Chatterjee, K. Sarkar, P. Jain, and N.E. Schreppler. On the suitability of broadband attenuation measurement for characterizing contrast microbubbles. *Ultrasound Med Biol*, 31(6):781–6, 2005. 6.1

Q. Chen, J. Zagzebski, T. Wilson, and T. Stiles. Pressure-dependent attenuation in ultrasound contrast agents. *Ultrasound Med Biol*, 28(8):1041–51, 2002a. 5.1, 6.1, 6.4

W.S. Chen, T.J. Matula, and L.A. Crum. The disapearance of ultrasound contrast bubbles: observations of bubble dissolution and cavitation nucleation. *Ultrasound Med Biol*, 28(6):793–803, 2002b. 2.5

W.S. Chen, T.J. Matula, A.A. Brayman, and L.A. Crum. A comparison of the fragmentation thresholds and inertial cavitation doses of different ultrasound contrast agents. *J Acoust Soc Am*, 113(1):643–51, 2003. 7.1

E. Chérin, J. Brown, S.-E. Måsøy, H. Shariff, R. Karshafian, R. Williams, P.N. Burns, and S. Foster. Radial modulation imaging of microbubble contrast agents at high frequency. *Ultrasound Med Biol*, 34(6):949–962, 2008. 9.1, 9.4

C.T. Chin, C. Lancée, J. Borsboom, F. Mastik, M. Frijlink, N. de Jong, M. Versluis, and D. Lohse. Brandaris 128: a 25 million frames per second digital camera with 128 highly sensitive frames. *Rev Sci Instru*, 74(12):5026–5034, 2003. 1.6, 3.3.1, 4.2, 5.2.2, 9.2.2, 10.2

J.E. Chomas, P. Dayton, D. May, and K. Ferrara. Threshold of fragmentation for ultrasonic contrast agents. *J Biomed Opt*, 6(2):141–150, 2001. 5.1

J.E. Chomas, P. Dayton, D. May, and K. Ferrara. Nondestructive subharmonic imaging. *IEEE Trans Ultrason Ferroelectr Freq Control*, 49(7):883–892, 2002. 1.3

C.C. Church. A theoretical study of cavitation generated by an extracorporeal shock wave lithotripter. *J Acoust Soc Am*, 86:215–227, 1989. 2.6.4

C.C. Church. The effects of an elastic solid surface layer on the radial pulsations of gas bubbles. *J Acoust Soc Am*, 97(3):1510–1521, 1995. 2.6.2, 2.6.2, 2.6.3, 2.6.3, 2.6.5, 2.6.7, 2.7, 2.8, 3.5, 5.1, 5.2.1, 6.1, 10.1

J.M. Crane and S.B. Hall. Rapid compression transforms interfacial monolayers of pulmonary surfactant. *Biophys J*, 80(4):1863–1872, 2001. 3.1, 3.1, 3.2.1

J.M. Crane, G. Putz, and S.B. Hall. Persistence of phase coexistence in disaturated phosphatidylcholine monolayers at high surface pressures. *Biophys J*, 77(6):3134–3143, 1999. 3.1

P.-G. De Gennes, F. Brochard-Wyart, and Quéré. *Capillarity and wetting phenomena: drops, bubbles, pearls, waves*. Springer, 2004. 3.2.2

N. de Jong and L. Hoff. Ultrasound scattering properties of albunex microspheres. *Ultrasonics*, 31 (3):175–181, 1993. 2.6.1, 2.6.2, 2.6.12, 6.2.1, 10.1

N. de Jong, F.J. Ten Cate, C.T. Lancée, J.R.T.C. Roelandt, and N. Bom. Principles and recent developments in ultrasound contrast agents. *Ultrasonics*, 29(4):324–330, 1991. 10.1

N. de Jong, L. Hoff, T. Skotland, and N. Bom. Absorption and scatter of encapsulated gas filled microbubbles: theoretical considerations and some measurements. *Ultrasonics*, 30(2):95–103, 1992. 6.2.1

N. de Jong, R. Cornet, and C.T. Lancée. Higher harmonics of vibrating gas-filled microspheres. part one: simulations. *Ultrasonics*, 32(6):447–453, 1994. 2.6.2, 2.6.5, 2.6.9, 2.7, 2.8, 3.2.2, 3.2.3, 4.3, 4.3, 9.2.1

N. de Jong, A. Bouakaz, and F.J. ten Cate. Contrast harmonic imaging. *Ultrasonics*, 40(1):567–573, 2002. 5.1

N. de Jong, M. Emmer, C.T. Chin, A. Bouakaz, F. Mastik, D. Lohse, and M. Versluis. "compression-only" behavior of phospholipid-coated contrast bubbles. *Ultrasound Med Biol*, 33(4):653–656, 2007. 2.6.9, 5.4, 6.1, 6.4, 9.1, 9.2.1, 10.1, 10.4

C.X. Deng and F.L. Lizzi. A review of physical phenomena associated with ultrasonic contrast agents and illustrative clinical applications. *Ultrasound Med Biol*, 28(3):277–86, 2002. 1.3, 5.1, 5.4, 11.1.4

C.X. Deng, F.L. Lizzi, A. Kalisz, A. Rosado, R.H. Silverman, and D.J. Coleman. Study of ultrasonic contrast agents using a dual-frequency band technique. *Ultrasound Med Biol*, 26(5): 819–831, 2000. 9.1

C. Devin, Jr. Survey of thermal, radiation, and viscous damping of pulsating air bubbles in water. *J Acoust Soc Am*, 31(12):1654–1667, 1959. 2.4, 2.6.2

P.A. Dijkmans, L.J. Juffermans, R.J. Musters, A. van Wamel, F.J. ten Cate, W. van Gilst, C.A. Visser, N. de Jong, and O. Kamp. Microbubbles and ultrasound: From diagnosis to therapy. *Eur J Echocardiogr*, 5:245–56, 2004. 1.5

P.A. Dijkmans, C.A. Visser, and O. Kamp. Adverse reactions to ultrasound contrast agents: Is the risk worth the benefit? *Eur J Echocardiogr*, 6:363–366, 2005. 1.4

A. Doinikov and P. Dayton. Maxwell rheological model for lipid-shelled ultrasound microbubble contrast agents. *J Acoust Soc Am*, 121(6):3331–3340, 2007. 2.6.10, 2.7, 2.8

F.A. Duck. *Physical properties of tissue*. Academic Press Limited, London, 1990. 6.1, 6.3.1, 6.3, 7.1, 7.4

F.A. Duck. Nonlinear acoustics in diagnostic ultrasound. *Ultrasound Med Biol*, 28:1–18, 2002. 9.1

P.B. Duncan and D. Needham. Test of the Epstein-Plesset model for gas microparticle dissolution in aqueous media: Effect of surface tension and gas undersaturation in solution. *Langmuir*, 20 (7):2567–2578, 2004. 3.1, 5.4

B.C. Eatock, R.Y. Nishi, and G.W. Johnston. Numerical studies of the spectrum of low-intensity ultrasound scattered by bubbles. *J Acoust Soc Am*, 77(5):1692–1701, 1985. 2.6.1

R.J. Eckersley, C.T. Chin, and P.N. Burns. Optimising phase and amplitude modulation schemes for imaging microbubble contrast agents at low acoustic power. *Ultrasound Med Biol*, 31(2): 213–9, 2005. 4.1, 5.1

A.I. Eller. Damping constants of pulsating bubbles. *J Acoust Soc Am*, 47(5 (Part2)):1469–1470, 1950. 2.4, 2.6.2

EMEA. www.emea.europe.eu/humandocs/humans/epar/sonovue/sonovue.htm, scientific discussion, 2004a. 1.4

EMEA. www.emea.europe.eu, document reference: Emea/cpmp/212/04, 2004b. 1.4

M. Emmer, D.E. Goertz, A. Van Wamel, M. Versluis, and N. De Jong. Threshold behavior of vibrating microbubbles. *IEEE Ultrasonics Symposium*, pages 1545–1547, 2006. 7.1, 8.1

M. Emmer, G. Matte, P. van Neer, A. van Wamel, and N. de Jong. Improved ultrasound contrast agent detection in a clinical setting. In *IEEE Ultrasonics Symposium*, pages 2235–2238, 2007a. 6.1, 6.4, 7.4, 10.1

M. Emmer, A. van Wamel, D.E. Goertz, and N. de Jong. The onset of microbubble vibration. *Ultrasound Med Biol*, 33(6):941–949, 2007b. 2.6.12, 6.1, 6.4, 7.1, 7.4, 8.1, 9.2.2, 10.1, 10.2, 10.4

M. Emmer, H.J. Vos, D.E. Goertz, A. van Wamel, M. Versluis, and N. de Jong. Vibrating microbubbles at low acoustic pressures. *Abstr. 12th Eur Symp Ultrasound Contrast Imaging*, page 84, 2007c. 6.1, 6.4, 7.1, 7.4, 8.1, 8.4, 10.1

M. Emmer, H.J. Vos, A. van Wamel, D.E. Goertz, M. Versluis, and N. de Jong. Clinical relevance of pressure-dependent scattering at low acoustic pressures. *Ultrasonics*, 47(1-4):74–77, 2007d. 8.1, 8.3

P. Epstein and M. Plesset. On the stability of gas bubbles in liquid-gas solutions. *J Chem Phys*, 18 (11):1505–1509, 1950. 2.5

FDA. www.fda.gov/cder/drug/infosheets/hcp/microbubblehcp.htm, 2008. 1.4

R.P. Frigg and S. Hartmann. *Models in science*. Stanford Encyclopedia of Philosophy, http://plato.stanford.edu/entries/models-science/, 2006. 2.1

P.J. Frinking, N. de Jong, and E.I. Céspedes. Scattering properties of encapsulated gas bubbles at high ultrasound pressures. *J Acoust Soc Am*, 105(3):523–533, 1999. 1.3

P.J. Frinking, E.I. Céspedes, J. Kirkhorn, H.G. Torp, and N. de Jong. A new ultrasound contrast imaging approach based on the combination of multiple imaging pulses and a separate release burst. *IEEE Trans Ultrason Ferroelect Freq Contr*, 48(3):643–651, 2001. 5.1

M. Fyrillas and A.J. Szeri. Dissolution or growth of soluble spherical oscillating bubbles. *J Fluid Mech*, 277:381–407, 1994. 3.3.2

G. Gaines and L. George. *Insoluble monolayers at liquid-gas interfaces*. Interscience Publishers, New York, 1966. 3.2.1

T.W. Galema, M.L. Geleijnse, W.B. Vletter, L. de Laat, and F.J. ten Cate. Clinical usefullness of sonovue contrast echocardiography: the Thorax Centre experience. *Neth Heart J*, 15(2):55–60, 2007. 1.1, 1.4

R.E. Glazman. Effects of adsorbed films on gas bubble radial oscillations. *J Acoust Soc Am*, 74 (3):980–986, 1983. 2.6.4, 3.2.2

D.E. Goertz, N. de Jong, and A.F. van der Steen. Attenuation and size distribution measurements of Definity(tm) and manipulated Definity(tm) populations. *Ultrasound Med Biol*, 33(9):1376–1388, 2007. 6.2.1

B.B. Goldberg, J.S. Raichlen, and F. Forsberg. *Ultrasound Contrast Agents, Basic principles and clinical applications, 2nd edition*. Martin Dunitz, London, 2001. 1.2.1, 1.2.2, 1.3, 2.5, 10.1, 11.1.4

J.-M. Gorce, M. Arditi, and M. Schneider. Influence of bubble size distribution on the echogenicity of ultrasound contrast agents: A study of Sonovue(tm). *Invest Radiol*, 35(11):661–671, 2000. 2.6.12, 3.3.1, 4.3, 4.3, 5.1, 5.2.1

R. Gramiak and P.M. Shah. Echocardiography of the aortic root. *Invest Radiol*, 3(5):356–366, 1968. 1.2.1

F. Graner, S. Perez-Oyarzun, A. Saint-Jalmes, C. Flament, and F. Gallet. Phospholipidic monolayers on formamide. *J Phys II France*, 5:313–322, 1995. 3.1

R. Hansen, B.A.J. Angelsen, P.N. Burns, A. Bouakaz, J. Borsboom, M. Versluis, and N. De Jong. Radial modulation imaging. In *The tenth European symposium on ultrasound contrast imaging, Rotterdam*, pages 90–91b, 2005. 9.1

S. Hilgenfeldt, D. Lohse, and M.P. Brenner. Phase diagrams for sonoluminescing bubbles. *Phys. Fluids*, 8(11):2808–2826, 1996. 2.3, 3.3.2

S. Hilgenfeldt, D. Lohse, and M. Zomack. Response of bubbles to diagnostic ultrasound: a unifying theoretical approach. *Eur Phys J B*, 4:247–255, 1998. 9.2.1

L. Hoff, P. Sontum, and J. Hovem. Oscillations of polymeric microbubbles: Effect of the encapsulating shell. *J Acoust Soc Am*, 107(4):2272–2280, 2000. 2.6.3, 2.6.6, 2.6.7, 2.6.8, 2.7, 4.1, 5.2.1, 10.1

D. Hope Simpson, C.T. Chin, and P.N. Burns. Pulse inversion doppler: A new method for detecting nonlinear echoes from microbubble contrast agents. *IEEE Trans Ultrason Ferroelectr Freq Control*, 46(2):372–382, 1999. 1.3, 9.1, 11.1.1

J.B. Keller and M. Miksis. Bubble oscillations of large amplitude. *J Acoust Soc Am*, 68(2):628–633, 1980. 2.3, 2.6.9, 2.6.12, 9.2.1

D.B. Khismatullin. Resonance frequency of microbubbles: Effect of viscosity. *J Acoust Soc Am*, 116(3):1463–73, 2004. 1.2.3, 10.1

D.B. Khismatullin and A. Nadim. Radial oscillations of encapsulated microbubbles in viscoelastic liquids. *Physics of fluids*, 14(10):3534–3557, 2002. 2.2, 2.6.5, 2.7

D.H. Kim, M.J. Costello, P.B. Duncan, and D. Needham. Mechanical properties and microstructure of polycrystalline phospholipid monolayer shells: Novel solid microparticles. *Langmuir*, 19: 8455–8466, 2003. 3.1, 5.2.1, 5.4, 10.4

A.L. Klibanov. Ligand-carrying gas-filled microbubbles: ultrasound contrast agents for targeted molecular imaging. *Bioconjugate Chem*, 16:9–17, 2005. 1.5

A.L. Klibanov. Ultrasound contrast agents: Development of the field and current status. *Top Curr Chem*, 222:73–106, 2002. 3.1

A.L. Klibanov, P.T. Rasche, M.S. Hughes, J.K. Wojdyla, K.P. Galen, J.H. Wible, and G.H. Brandenburger. Detection of individual microbubbles of ultrasound contrast agents: imaging of free-floating and targeted bubbles. *Invest Radiol*, 39(3):187195, 2004. 10.2

K. Kooiman, M. Harteveld, N. de Jong, and A. van Wamel. Transiently increased endothelial layer permeability by ultrasound-activated microbubbles. *IEEE Ultrasonics Symposium*, pages 529–531, 2006. 1.5

K. Kooiman, M.R. Böhmer, M. Emmer, H.J. Vos, C. Chlon, W.T. Shi, C.S. Hall, S.H. de Winter, K. Schroën, M. Versluis, N. de Jong, and A. van Wamel. Oil-filled polymer microcapsules for ultrasound-mediated delivery of lipophilic drugs. *J Contr Release*, page In Press, 2008. 1.5

L.L. Kusnetzky, A. Khalid, T.M. Khumri, T.G. Moe, P.G. Jones, and M.L. Main. Acute mortality in hospitalized patients undergoing echocardiography with and without an ultrasound contrast agent. *J Am Coll Cardiol*, 51(17):1704–1706, 2008. 1.4

W. Lauterborn. Numerical investigation of nonlinear oscillations of gas bubbles in liquids. *J Acoust Soc Am*, 59(2):283–293, 1976. 2.2

S. Lee, D.H. Kim, and D. Needham. Equilibrium and dynamic interfacial tension measurements at microscopic interfaces using a micropipet technique. 2: Dynamics of phospholipid monolayer formation and equilibrium tensions at the water-air interface. *Langmuir*, 17(18):5544–5550, 2001. 3.1

T.G. Leighton. *The acoustic bubble*. Academic Press Limited, London, 1994. 1.2.3, 2.2, 2.2, 2.2, 2.4, 5.1, 5.2.1, 10.1

T.G. Leighton and H.A. Dumbrell. New approaches to contrast agent modelling. *Journal of Physics: Conference Series*, 1:91–96, 2004. 2.2, 2.4

H.-D. Liang and M.J.K. Blomley. The role of ultrasound in molecular imaging. *Br J Radiol*, 76: S140–S150, 2003. 1.5

M.M. Lipp, K.Y.C. Lee, D.Y. Takamoto, J.A. Zusadzinski, and A.J. Waring. Coexistence of buckled and flat monolayers. *Phys. Rev. Lett.*, 81:1650–1653, 1998. 5.4

M.L. Main, J.H. Goldman, and P.A. Grayburn. Thinking outside the "box" - the ultrasound contrast controversy. *J Am Coll Cardiol*, 50(25):2434–2437, 2007. 1.4, 1.4

P. Marmottant, S. van der Meer, M. Emmer, M. Versluis, N. de Jong, S. Hilgenfeldt, and D. Lohse. A model for large amplitude oscillations of coated bubbles accounting for buckling and rupture. *J Acoust Soc Am*, 118(6):3499–3505, 2005. 2.6.4, 2.6.9, 2.6.11, 2.6.11, 2.7, 2.8, 4.3, 4.4, 5.4, 6.1, 6.4, 9.1, 9.2.1, 9.2.1, 9.2.1, 9.4, 10.1, 10.4, 11.1.2, 11.1.3, 11.1.4, 11.1.5, 11.2

S.-E. Måsøy, Ø. Standal, P. Näsholm, T.F. Johansen, B.A.J. Angelsen, and R. Hansen. Surf imaging: In vivo demonstration of an ultrasound contrast agent detection technique. *IEEE Trans Ultrason Freeoelectr Freq Control*, 55:1112–1121, 2008. 9.1, 9.4

H. Medwin. Counting bubbles acoustically: a review. *Ultrasonics*, 15:7–13, 1977. 2.2, 2.4, 2.6.1

K.E. Morgan, J.S. Allen, P.A. Dayton, J.E. Chomas, A.L. Klibanov, and K.W. Ferrara. Experimental and theoretical evaluation of microbubble behavior: effect of transmitted phase and bubble size. *IEEE Trans Ultrason Ferroelect Freq Contr*, 47(6):1494–1509, 2000. 2.6.4, 2.7, 3.2.2, 5.1

S.L. Mulvagh, A.N. DeMaria, S.B. Feinstein, P.N. Burns, S. Kaul, M. Miller, J.G. Monaghan, T.R. Porter, L.J. Shaw, and F.S. Villanueva. Contrast echocardiography: current and future applications. *J Am Soc Echocardiogr*, 13(4):331–342, 2000. 1.1

E.M. Nakamura, L. Cordi, G.S.G. Almeida, N. Duran, and L.H.I. Mei. Study and development of LDPE/starch partially biodegradable compounds. *J Mat Proc Tech*, pages 162–163, 2005. 5.4

V.L. Newhouse and P. Mohana Shankar. Bubble size measurements using the nonlinear mixing of two frequencies. *J Acoust Soc Am*, 75(5):1473–1477, 1984. 9.1, 9.4

R.I. Nigmatulin, N.S. Khabeev, and F.B. Nagiev. Dynamics, heat and mass transfer of vapour-gas bubbles in liquid. *Int J Heat Mass Trans*, 24:1033–1044, 1981. 2.4

B.E. Noltingk and E.A. Neppiras. Caviation produced by ultrasonics. *Proc Phys Soc London B*, 63:674–685, 1950. 2.2

W.D. O'Brien, Jr. Ultrasound-biophysics mechanisms. *Prog Biophys Mol Biol*, 93:212–255, 2007. 1.3, 11.1.4

M. Overvelde, V. Garbin, B. Dollet, N. de Jong, D. Lohse, and M. Versluis. Nonlinear shell dynamics near the resonance frequency of ultrasound contrast agents. *IEEE Ultrasonics Symposium*, 2008. 2.6.9, 11.1.3

N.G. Pace, A. Cowley, and Campbell A.M. Short pulse acoustic excitation of microbubbles. *J Acoust Soc Am*, 102(3):1474–1479, 1997. 1.2.3

M.-C. Pauzin, S. Mensah, and J.-P. Lefebvre. Development of a finite element model of ultrasound contrast agent. *IEEE Ultrasonics Symposium*, pages 1989–1992, 2007. 2.2

F. Pétriat, E. Roux, J.-C Leroux, and S. Giasson. Study of molecular interactions between a phospholipidic layer and a pH-sensitive polymer using the langmuir balance technique. *Langmuir*, 20(4):1393–1400, 2004. 3.1

M. Plesset. The dynamics of cavitation bubbles. *J Appl Mech*, 16:277–282, 1949. 2.2

M. Postema, A. Bouakaz, C.T. Chin, and de Jong N. Simulations and measurements of optical images of insonified ultrasound contrast microbubbles. *IEEE Trans Ultrason, Ferroelect, Freq Contr*, 50(5):523–536, 2003. 5.1, 5.2.2, 5.3.2

M. Postema, A. van Wamel, C.T. Lancée, and N. de Jong. Ultrasound-induced encapsulated microbubble phenomena. *Ultrasound Med Biol*, 30(6):827–840, 2004. 5.1

A. Preston, T. Colonius, and C.E. Brennen. A reduced-order model of heat transfer effects on the dynamics of bubbles. *Proceedings of ASME FEDSM'02*, 2002. 2.4

A. Prosperetti. Thermal effects and damping mechanisms in the forced radial oscillations of gas bubbles in liquid. *J Acoust Soc Am*, 61(1):17–27, 1977. 2.4

A. Prosperetti. Bubble phenomena in sound fields: part one. *Ultrasonics*, 22(2):69–77, 1984. 3.2.2

A. Prosperetti. The thermal behaviour of oscillating gas bubbles. *J Fluid Mech*, 222:587–616, 1991. 2.2, 2.4

L. Rayleigh. On the pressure developed in a liquid during collapse of a spherical cavity. *Philosophical Magazine*, 34:94–98, 1917. 2.2

R.A. Roy, S.I. Madanshetty, and R.E. Apfel. An acoustic backscattering technique for the detection of transient cavitation produced by microsecond pulses of ultrasound. *J Acoust Soc Am*, 87(6): 2451–8, 1990. 9.1

A. Saint-Jalmes and F. Gallet. Buckling in a solid langmuir monolayer: light scattering measurements and elastic model. *Eur Phys J B*, 2(4):489–494, 1998. 3.1

A. Saint-Jalmes, F. Graner, F. Gallet, and B. Houchmandzadeh. Buckling of a bidimensional solid. *Europhys Lett*, 28:489–494, 1994. 3.1

M.I. Sández, A. Suárez, and A. Gil. Surface pressure-area isotherms and fluorescent behavior of phospholipids containing labeled pyrene. *Colloid Interface Sci*, 250(1):128–133, 2002. 3.1

K. Sarkar, W.T. Shi, D. Chatterjee, and F. Forsberg. Characterization of ultrasound contrast microbubbles using in vitro experiments and viscous and viscoelastic interface models for encapsulation. *J Acoust Soc Am*, 118(1):539–50, 2005. 2.6.6, 2.6.6, 2.6.8, 2.6.10, 2.6.11, 2.6.12, 2.7

V. Sboros, C.A. MacDonald, S.D. Pye, C.M. Moran, J. Gomatam, and W.N. McDicken. The dependence of ultrasound contrast agents backscatter on acoustic pressure: theory versus experiment. *Ultrasonics*, 40(1-8):579–83, 2002. 5.1

M. Schneider. Sonovue, a new ultrasound contrast agent. *Eur Radiol*, 9:347–348, 1999. 10.2, 11.1.5

M. Schneider, M. Arditi, M.-B. Barrau, J. Brochot, A. Broillet, R. Ventrone, and F. Yan. BR1: A new ultrasonic contrast agent based on sulfur hexafluoride-filled microbubbles. *Invest. Radiol.*, 30(8):451–457, 1995. 3.1, 3.2.1, 3.3.1

M. Schneider, A. Broillet, P. Bussat, N. Giessinger, J. Puginier, R. Ventrone, and F. Yan. Gray-scale liver enhancement in VX2 tumorbearing rabbits using BR14, a new ultrasonographic contrast agent. *Invest Radiol*, 32(7):410–417, 1997. 3.3.1

B.A. Schrope and V.L. Newhouse. Second harmonic ultrasonic blood perfusion measurement. *Ultrasound Med Biol*, 19(7):567–79, 1993. 1.3, 9.1, 11.1.1

B.A. Schrope, V.L. Newhouse, and V. Uhlendorf. Simulated capillary blood flow measurement using a nonlinear ultrasonic contrast agent. *Ultrasonic Imaging*, 14(2):134–158, 1992. 1.3, 6.4

H. Shariff, P. Bevan, R. Karshafian, R. Williams, and P.N. Burns. Radial modulation imaging: Raising the frequency for contrast imaging. In *IEEE Ultrasonics Symposium*, pages 104–107, 2006a. 9.1, 9.4

H.H. Shariff, P.D. Bevan, R. Karshafian, M. Karakolis, M. Banerjee, and P.N. Burns. Radial modulation imaging: A dual frequency ultrasound imaging technique for microbubble contrast. In *The eleventh European symposium on ultrasound contrast imaging, Rotterdam*, pages 64–66, 2006b. 9.1

W.T. Shi and F. Forsberg. Ultrasonic characterization of the nonlinear properties of contrast microbubbles. *Ultrasound Med Biol*, 26(1):93–104, 2000. 1.3, 6.1

W.T. Shi, F. Forsberg, J.S. Raichlen, L. Needleman, and B.B. Goldberg. Pressure dependence of subharmonic signals from contrast microbubbles. *Ultrasound Med Biol*, 25(2):275–283, 1999. 5.1

J. Sijl, E. Gaud, P.J.A. Frinking, M. Arditi, N. de Jong, D. Lohse, and M. Versluis. Acoustic characterization of single ultrasound contrast agent microbubbles. *J Acoust Soc Am*, 2008. 9.4, 10.4

W. Silvert. Modelling as a discipline. *Int J General Systems*, pages 1–22, 2000. 2.1

D.M. Skyba, R.J. Price, A.Z. Linka, T.C. Skalak, and S. Kaul. Direct in vivo visualization of intravascular destruction of microbubbles by ultrasound and its local effects on tissue. *Circulation*, 98:290–293, 1998. 1.5

O.I.I. Soliman, M.L. Geleijnse, F.J. Meijboom, A. Nemes, O. Kamp, P. Nihoyannopoulos, N. Masanid, S.B. Feinstein, and F.J. Ten Cate. The use of contrast echocardiography for the detection of cardiac shunts. *Eur J of Echocardiography*, 8(3):s2–s12, 2007. 1.2.1

E. Stride. The influence of surface adsorption on microbubble dynamics. *Phil Trans R Soc*, 366: 2103–2115, 2008. 2.2, 2.6.11, 2.6.11, 2.6.11, 2.7, 2.8, 11.1.2, 11.2

E. Stride and N. Saffari. Theoretical and experimental investigation of the behaviour of ultrasound contrast agent particles in whole blood. *Ultrasound Med Biol*, 30(11):1495–1509, 2004. 9.2.1

E. Stride, K. Pancholi, M.J. Edirisinghe, and S. Samarasinghe. Increasing the nonlinear character of microbubble oscillations at low acoustic pressures. *J R Soc Interface*, 5(24):807–811, 2008. 10.1

M.-X. Tang and R.J. Eckersley. Frequency and pressure dependent attenuation and scattering by microbubbles. *Ultrasound Med Biol*, 33(1):164–168, 2007. 6.1, 6.4, 7.1

M.-X. Tang, R.J. Eckersley, and J.A. Noble. Pressure-dependent attenuation with microbubbles at low mechanical index. *Ultrasound Med Biol*, 31(3):377–384, 2005. 5.1, 5.4, 6.1, 7.1

C.J.P.M. Teirlinck, R.A. Bezemer, C. Kollmann, J. Lubbers, P.R. Hoskins, P. Fish, K.-E. Fredfeldt, and U.G. Schaarschmidt. Development of an example flow test object and comparison of five of these test objects, constructed in various laboratories. *Ultrasonics*, 36(1):653–660, 1998. 7.2

R. Tögel and D. Lohse. Phase diagrams for sonoluminescing bubbles: A comparison between experiment and theory. *J Chem Phys*, 118(4):1863–1875, 2003. 2.4

K. Tsiglifis and N.A. Pelekasis. Nonlinear radial oscillations of encapsulated microbubbles subject to ultrasound: The effect of membrane consitutive law. *J Acoust Soc Am*, 123(6):4059–4070, 2008. 2.6.7, 2.6.12, 2.7, 2.8, 11.1.2, 11.1.3, 11.1.4, 11.2

E.C. Unger, T. Porter, W. Culp, R. Labell, T. Matsunaga, and R. Zutshi. Therapeutic applications of lipid-coated microbubbles. *Adv Drug Deliv Rev*, 56(9):1291–314, 2004. 1.5

G. van Camp, S. Droogmans, and B. Cosyns. Bio-effects of ultrasound contrast agents in daily clinical practice: fact or fiction? *Eur Heart J*, 28:1190–1192, 2007. 1.4, 1.5

S.M. van der Meer, B. Dollet, M.M. Voormolen, C.T. Chin, A. Bouakaz, N. de Jong, M. Versluis, and D. Lohse. Microbubble spectroscopy of ultrasound contrast agents. *J Acoust Soc Am*, 121 (1):648–656, 2007. 1.2.3, 2.4, 4.2, 6.1, 9.2.1, 9.2.2, 10.1, 10.2

A. van Wamel, K. Kooiman, M. Harteveld, M. Emmer, F.J. ten Cate, M. Versluis, and N. de Jong. Vibrating microbubbles poking individual cells: Drug transfer into cells via sonoporation. *J Contr Release*, 112:149–155, 2006. 1.5

K. Vokurka. Comparison of Rayleigh's, Herring's, and Gilmore's models of gas bubbles. *Acustica*, 59(3):214–219, 1986. 2.3, 2.6.4

M. Wyczalkowski and A.J. Szeri. Optimization of acoustic scattering from dual-frequency driven microbubbles at the difference frequency. *J Acoust Soc Am*, 113(6):3073–9, 2003. 9.1

S. Zhao, K. Ferrara, and P. Dayton. Asymmetric oscillation of adherent targeted ultrasound contrast agents. *Appl Phys Lett*, 87:134103, 2005. 5.4

Summary

Ultrasound imaging is widely used in clinical radiology and cardiology applications. Blood is a poor ultrasound scatterer and remains dark in an echo image. To enhance the acoustic backscattering from blood and thus the ability to detect blood flow in soft tissue, ultrasound contrast agents have been developed. These contrast agents consist of fluids with coated gas filled microbubbles, which are introduced in the body by an intravenous injection.

The contrast agent microbubbles are effective scatterers owing to the large compressibility difference between the surrounding fluid and the coated gas. Under the influence of an ultrasound field, the microbubbles can vibrate linearly and nonlinearly. Nonlinear vibrations result in a backscattered signal containing higher harmonics of the incident frequency. These harmonic signals are exploited in contrast agent detection techniques.

Whereas the behavior of free gas microbubbles at low and moderate amplitudes can be predicted, the impact of an additional coating on the microbubble behavior has currently not been fully elucidated. Various models have been defined to describe the dynamics of ultrasound driven coated microbubbles (chapter 2). This has however not resulted in a model that is able to fully predict experimentally observed coated microbubble behavior.

The aim of this thesis is to contribute to an enhanced understanding of the behavior of coated microbubbles in an ultrasound field. We hereby use a unique high-speed camera system, which allows us to study single oscillating microbubbles in ultrasound pressure fields with MHz frequencies.

Our results show highly nonlinear behavior of phospholipid-coated microbubbles at low acoustic pressures (10-250 kPa). This behavior was not predicted by the theoretical descriptions of coated bubble behavior. The first observation of nonlinear behavior was termed 'compression-only behavior' (chapter 4). This behavior implies asymmetrical radial responses whereby the compression amplitude outweighs the expansion amplitude with at least a factor of two.

Furthermore, we observed 'threshold behavior' (chapter 5). This term indicates that microbubbles showing this behavior do not have a linear oscillation onset. The acoustic pressure had to exceed a certain threshold value before oscillations of microbubbles with sizes smaller than 5.0 μm diameter at a frequency of 1.7 MHz were observed. Compression-only and threshold behavior seem to be related to the resonance frequency of the microbubble and occur when the microbubble is insonified with a frequency below the resonance frequency and at a low acoustic pressure.

The knowledge that was gained from the high-speed camera experiments was applied to develop a new theoretical description of the vibrations of phospholipid-coated microbubbles (chapter 3). In previous theoretical descriptions, the properties of the coating have been modeled using parameters with constant values. In this new model, the influence of the coating on the microbubble response depends on the coating surface area. Using these dynamic coating properties, it appeared that compression-only behavior can be predicted.

In addition, acoustic experiments were performed (chapter 6). It appeared in chapter 5 that smaller microbubble sizes show threshold behavior. Thus contrast agent suspensions were mechanically filtered such that these filtered suspensions contained smaller bubble sizes only. The pressure dependency of the acoustic responses of these filtered suspensions was compared to that of native suspensions containing the unfiltered contrast agent from the vial. According to theory, these acoustic responses should be pressure-independent. The filtered suspensions however showed highly pressure-dependent responses, from which it was concluded that threshold behavior results in pressure-dependent acoustic behavior.

Pressure-dependent scattering can be utilized for imaging. This was tested applying a power modulation imaging technique at the fundamental frequency (chapter 7 and 8). Filtered suspensions with mainly microbubbles showing threshold behavior were compared to native suspensions. The filtered suspensions gave higher contrast-to-tissue ratios than the native suspensions, thus threshold behavior can be utilized to enhance the contrast in a power modulation imaging technique.

The radial modulation imaging technique was investigated in chapter 9. This imaging technique is based on dual-frequency insonation of the microbubbles. We studied the effect of compression-only behavior on the radial modulation of phospholipid-coated microbubbles. Microbubbles that showed strong compression-only behavior, appeared to be highly radially modulated. However, these microbubbles were less effective sound scatterers. Larger microbubbles were less modulated, but scattered more sound. This appeared to be a more effective combination for radial modulation imaging than the highly radially modulated smaller microbubble sizes.

As compression-only and threshold behavior of phospholipid-coated microbubbles can be exploited for imaging, it was investigated if we were able to enhance these nonlinear responses (chapter 10). For this purpose, the composition of the phospholipid-coatings was modified. The responses to ultrasound from the custom-made coated microbubbles were compared to the responses of a commercially available contrast agent. Currently, these modifications resulted in neither a significantly increased compression-only nor an increased threshold behavior. It is however expected that in future, such coating modifications will lead to enhanced nonlinear effects, which is relevant for imaging and the development of new contrast agents.

Samenvatting

Echografie is een beeldvormende techniek die gebruik maakt van ultrageluid. Een scanner zendt ultrageluid uit. In het lichaam wordt dit ultrageluid (gedeeltelijk) gereflecteerd bij overgangen tussen verschillende soorten weefsel. Deze reflecties (echo's) worden weer opgevangen in de scanner en verwerkt tot een beeld. Dit beeld laat de structuur en grootte van het weefsel zien, maar ook mogelijke afwijkingen. Echografie wordt veelvuldig gebruikt in de kliniek, onder andere voor allerlei toepassingen in de radiologie en cardiologie.

In een echobeeld zijn structuren in het weefsel goed te zien, maar omdat bloed weinig ultrageluid reflecteert, is bloed is niet goed zichtbaar. Om bloed en dus de doorbloeding van weefsel zichtbaar te maken, zijn er ultrageluidscontrastmiddelen ontwikkeld. Deze ultrageluidscontrastmiddelen worden via een injectie in een ader in het lichaam gebracht en bestaan uit een vloeistof met daarin gasbelletjes ter grootte van enkele micrometers. Deze gasbelletjes zijn gecoat met een eiwit, polymeer of vet om te voorkomen dat het belletje (te snel) oplost.

Deze microbelletjes reflecteren (verstrooien) veel ultrageluid vanwege hun grote samendrukbaarheid in vergelijking met omliggende vloeistof en weefsel. Door deze samendrukbaarheid gaan zij in een ultrageluidsveld vibreren. Deze vibratie kan zowel lineair als niet lineair zijn. Wanneer het belletje niet-lineair trilt, zal het door het belletje gegenereerde ultrageluidssignaal zowel de frequentie van het uitgezonden ultrageluidssignaal bevatten als harmonische frequenties. In vergelijking met het ultrageluid van de bellen, zal het ultrageluid dat gereflecteerd wordt door het weefsel veel minder energie op de harmonische frequenties bevatten. Dit maakt deze harmonische frequenties zeer bruikbaar om de bellen te onderscheiden van het weefsel en zo het contrast tussen bellen en weefsel nog meer vergroten.

Het gedrag van vrije gasbellen in een ultrageluidsveld is bekend. Het is echter nog niet volledig bekend welke invloed het toevoegen van een coating op het gedrag van de bel heeft. Er zijn verschillende modellen gedefinieerd om de dynamica van gecoate bellen te voorspellen (zie hoofdstuk 2), maar geen van deze modellen is in staat om al het experimenteel waargenomen gedrag theoretisch te voorspellen.

Het doel van dit proefschrift is het vergroten van de kennis over het gedrag van gecoate microbellen in een ultrageluidsveld. We gebruiken hierbij een unieke hogesnelheidscamera waarmee we de individuele microbellen optisch in een ultrageluidsveld kunnen bestuderen. Deze camera kan tot 25 miljoen beelden per seconde opnemen. Deze hoge snelheid is noodzakelijk om vibraties met frequenties in de orde van MHz te kunnen

bestuderen.

Niet-lineair gedrag van een bel wordt normaal gesproken veroorzaakt doordat de bel niet oneindig kan worden ingedrukt, terwijl expansie van de bel in beginsel geen limiet kent. Dit betekent dat naarmate de amplitude van de vibratie van de bel groter wordt, de bel meer zal neigen naar niet-lineair gedrag. De amplitude van de belvibratie hangt af van de ultrageluidsfrequentie en resonantiefrequentie van de bel, maar ook van de akoestische druk. Een grotere akoestische druk zorgt voor een grotere amplitude van de vibratie van de bel.

In dit proefschrift keken we vooral naar lage akoestische drukken en zagen we twee typen niet-lineair gedrag van fosfolipide gecoate bellen, die anders waren dan het algemeen niet-lineaire gedrag zoals hierboven beschreven. We noemden deze twee typen *compression-only* gedrag en *threshold* gedrag (hoofdstuk 4 en 5). Bij bellen die *compression-only* gedrag lieten zien werd niet de expansie amplitude groter, maar de compressie amplitude van deze bellen was groter dan hun expansie amplitude. De expansie amplitude was soms zelfs geheel afwezig.

Bellen die *threshold* gedrag lieten zien, lieten geen vibraties zien bij de laagste akoestische drukken terwijl die drukken nu juist in het lineaire regime lagen en daarvoor een lineaire vibratie werd verwacht. Voor deze bellen moest de akoestische druk eerst een bepaalde grenswaarde overstijgen, voordat hun vibratie kon worden waargenomen. Zowel *compression-only* als *threshold* gedrag werden alleen waargenomen als de bellen ultrageluid ontvingen met een frequentie lager dan hun resonantiefrequentie. Deze gedragingen worden toegeschreven aan invloeden van de coating.

Tot voor kort waren contrastbelmodellen niet in staat *compression-only* of *threshold* gedrag te voorspellen. In deze modellen hebben de parameters om de coating te beschrijven een vaste waarde. Dit proefschrift beschrijft een model waarbij de eigenschappen van de coating veranderen afhankelijk van de grootte van het beloppervlak en het blijkt dat een dergelijk model *compression-only* gedrag wel kan voorspellen (hoofdstuk 3).

Vervolgens hebben we onderzocht of *threshold* gedrag gebruikt zou kunnen worden in een klinische toepassing. Hiervoor moest worden bepaald of *threshold* gedrag akoestisch gemeten zou kunnen worden. Het blijkt dat bellen in een ultrageluidsveld die optisch *threshold* gedrag laten zien, ook in hun akoestische signaal een niet-lineaire geluidsdrukafhankelijkheid laten zien (hoofdstuk 6).

In hoofdstuk 7 en 8 wordt deze niet lineaire geluidsdrukafhankelijkheid gebruikt om de bellen te onderscheiden van weefsel in een echobeeld. Weefsel reflecteert namelijk geen geluid met een dergelijke drukafhankelijkheid. Dit is nieuw in vergelijking met bestaande contrast verhogende methoden, omdat hier alleen gebruik wordt gemaakt van de fundamenteel uitgezonden frequentie en niet van de harmonischen. Het voordeel hiervan is dat deze methode in de praktijk toegepast kan worden met een eenvoudige klinische scanner.

De ontdekkingen van *compression-only* en *threshold* gedrag hebben verstrekkende gevolgen, omdat bij de ontwikkeling van bestaande contrastmiddeldetectietechnieken geen rekening is gehouden met deze typen niet-lineair gedrag. *Compression-only* en *threshold* gedrag kunnen huidige contrastmiddeldetectietechnieken positief beïnvloeden,

maar ook negatief. We hebben dit onderzocht voor de recentelijk ontwikkelde contrastmiddeldetectietechniek *radial modulation imaging* (hoofdstuk 9) waarbij we keken naar de invloed van *compression-only* gedrag. Het blijkt dat *compression-only* gedrag eerder een nadeel is dan een voordeel voor deze techniek, omdat de extra harmonische frequenties in het gereflecteerde ultrageluid nadelig zijn voor de resolutie in het echobeeld.

Bij andere contrastmiddeldetectietechnieken kan de extra niet-lineariteit in het gereflecteerde ultrageluid wel benut worden, zie bijvoorbeeld hoofdstuk 7 en 8. We hebben daarom in hoofdstuk 10 onderzocht of we bellen konden maken die meer *compression-only* of *threshold* gedrag laten zien in vergelijking met commercieel verkrijgbare contrastbellen. We hebben hiervoor bellen gemaakt die gecoat waren met verschillende fosfolipiden en deze bellen onderzocht met de hogesnelheidscamera. We zagen geen significante verschillen, maar verwachten wel dat in de toekomst een dergelijk aangepaste contrastbel tot meer contrast in echobeelden zal leiden wanneer deze toegepast wordt in combinatie met een detectietechniek die gebruik maakt van *compression-only* of *threshold* gedrag.

Dankwoord

"En als je dan die experimenten gedaan hebt enzo, wat doe je dan verder nog?", aldus een bezoekende student van de Technische Universiteit Delft. Menig verjaardag of kapperbezoek verloopt vergelijkbaar. Hoe leg je uit dat je bijna vijf jaar van je werkzame (en meer) leven wijdt aan $1.4 \times 10^{-17} m^3$ gas gescheiden van water door een 3.0 nm dik laagje vet. Natuurlijk is daar het grote einddoel, toepassing van onze ontdekkingen bij de patiënt in het ziekenhuis, maar de dagelijkse praktijk is het beteugelen van lekkages in waterbakjes, het opsporen van aardlussen en andere stoorzenders, het begrijpen van rammelende formules en het verklaren van onverklaarbare resultaten met als einddoel een gladgestreken artikel. Ik weet nu dat dit niet uit te leggen valt. Je moet ervaren hoe boeiend het is om na elke oplossing op zoek te gaan naar het volgende probleem.

Het *Biomedical Engineering* Lab op de 23ste heeft alles (behalve ruimte) wat nodig is om deze zoektocht tot een succes te maken. Er heerst een goede sfeer waarbij gezelligheid gecombineerd wordt met actie en wetenschappelijke diepgang. De drijvende krachten achter het lab zijn mijn promotoren Ton van der Steen en Nico de Jong. Ik wil dan ook graag hen en alle collega's bedanken, die altijd bereid waren mij van goede raad te voorzien, mijn formulieren in te vullen, mijn opstellingen vorm te geven, mijn computer tot de orde te roepen en natuurlijk met mij de koetjes en de kalfjes te bespreken.

Mijn (ex)kamergenoten Klazina Kooiman, Miranda Harteveld en Annemieke van Wamel draaiden hun hand niet om voor de calorie-index van taai taai tot gevulde koek of voor het wel en wee van vis tot proefschrift. Meiden, bedankt voor de gezelligheid en Klazina, bedankt voor het lezen van intro en discussie!

Ook dank aan de *Physics of Fluids* groep in Twente. Ik heb veel geleerd van de aanpak van '*bubble trouble*' in deze groep, evenals van onze discussies en de grote bereidheid om mijn vragen te beantwoorden.

In het bijzonder wil ik graag Nico bedanken. Nico benadert de ideale begeleider. Hij stelt vragen, maar geeft desgewenst ook (mogelijke) oplossingen. Zoals een goed wetenschapper betaamt, is hij open-minded en nieuwsgierig, maar ook zorgt hij samen met Mieke Pruijsten voor de broodnodige input voor een onderwerp dat ondanks dat het de belangrijkste bijzaak in het leven is, toch onderbelicht blijft in het lab.

Ik weet nog dat Nico suggereerde dat Rik Vos en ik maar eens wat meer moesten gaan samenwerken. Dat was een vruchtbare zet. Rik bleek de perfecte sparring partner. Soms is het even slikken als hij weer de vinger op de zere plek weet te leggen, maar het paper werd er altijd beter van. Rik, bedankt voor je hulp!

Voor Rik was er Dave Goertz. Dave heeft mij een belangrijk deel van de methoden

die ik gebruikt heb in dit proefschrift geleerd. Dave combineert een grote kennis met een scherp oog voor detail en een bereidheid die kennis te delen. Dave, ook bedankt voor je geduld als ik dezelfde vraag nog een keer (of twee) stelde.

Dan zijn er nog de mensen die ter elfder uren gevraagd werden zich met het promotieproces te bemoeien. De kaft is ontworpen door iemand die zich niet heeft laten afschrikken door de krappe deadline en mijn vage aanwijzingen (het ging over belletjes en blauw is mijn lievelingskleur). Pascale, bedankt voor je creativiteit en inzet!

Ik zie vol vertrouwen de verdediging tegemoet met twee geweldige paranimfen naast me, Wilma van de Wassenberg en Olga Schouten. Bedankt dat jullie me bij willen bijstaan in een van de meest zenuwachtige momenten van mijn leven. Jullie maken deel uit van respectievelijk mijn studievriendinnen- en voetbalmeiden-toen-ik-nog-een-jongtalent-was-clubje. Het onderhouden van het contact met jullie, maar ook met de meiden van de middelbare school en vriendinnen vanuit Eindhoven, valt me soms niet mee. Ik waardeer jullie onvoorwaardelijke vriendschap. Het is altijd gezellig als we elkaar weer zien. Heel erg bedankt meiden en ik heb zin in onze komende uitjes, jubilea en andere feesten!

Twee mensen verdienen nog het meest bedankt te worden en dat zijn mijn ouders. Zij hebben aan de basis gestaan van alles. Zij hebben mij in staat gesteld mij volledig te kunnen concentreren op mijn studie en altijd waren zij daar voor de morele steun. Pa en ma, bedankt!

Tot slot, mijn leven is al ruim twee jaar verrijkt met een leuke vrouw en sinds kort zelfs met twee harige monsters. Samen zorgen zij ervoor dat ik met plezier naar huis ga. De harige monsters doen dat door volledig voorbij te gaan aan iets als werk. Een toetsenbord of artikel ligt nu eenmaal lekkerder. Voor begrip en steun kan ik gelukkig bij Sally terecht. Zij was altijd bereid om te luisteren naar beschouwingen over het boeiende leven van de microbel (‘*beam me up, Scotty!*’), maar verschafte ook het beste excuus om niet te werken. Sally, bedankt voor alles en we gaan voor een mooi vervolg post-proefschrift!

Marcia Emmer
Rotterdam, januari 2009

About the author

Marcia Emmer was born on May 4th, 1980 in Heerhugowaard, the Netherlands. In the course of secondary school (VWO) at the Han Fortmann College in Heerhugowaard, she discovered her broad interest, especially in the exact sciences and her fascination for the working of the human body. After graduation in 1998, she therefore went to the Technical University in Eindhoven to study Biomedical Engineering. In 2001, she obtained the BSc degree and chose the division Biomechanics and Tissue Engineering to continue her Master studies.

At the end of 2002, she went for a three-month externship to the Politecnico di Milano in Italy. There she built an experimental model to investigate the fluid dynamics around the heart after a palliative procedure to improve pulmonary blood flow in some forms of congenital heart disease.

In 2003, she started her MSc graduation project at the Technical University in Eindhoven. In this project, a lumped parameter model was defined to study the effect of leakage after repair of an abdominal aortic aneurysm.

She graduated in April 2004 and moved her activities to the Erasmus Medical Center in Rotterdam, at the department of Biomedical Engineering from Prof Ton van der Steen. At this department, she was employed by the Stichting voor Fundamenteel Onderzoek der Materie (FOM) in order to pursue a PhD degree. In the doctoral research, she performed optical and acoustical measurements to investigate the behavior of contrast agent bubbles in an ultrasound field under the supervision of Prof Nico de Jong.

List of publications

Peer-reviewed articles

M. Emmer, H.J. Vos, N. de Jong. Radial modulation of single microbubbles. *IEEE Trans Ultrason Ferroelectr Freq Control*, submitted, 2008.

K. Kooiman, M.R. Böhmer, **M. Emmer**, H.J. Vos, C. Chlon, W.T. Shi, C.S. Hall, S.H.P.M. de Winter, K. Schroën, M. Versluis, N. de Jong, A. van Wamel. Oil-filled polymer microcapsules for ultrasound-mediated delivery of lipophilic drugs. *J Control Release*, in press, 2008.

B.D.M. Meijering, L.J.M. Juffermans, R.H. Henning, I.S. Zuhorn, **M. Emmer**, W. Paulus, W.H. van Gilst, K. Kooiman, N. de Jong, A. van Wamel, R. Musters, O. Kamp, L.E. Deelman. Ultrasound and microbubbles targeted delivery of macromolecules is regulated by the induction of endocytosis and pore formation. *Circulation Research*, submitted, 2008.

M. Emmer, H.J. Vos, D.E. Goertz, A. van Wamel, M. Versluis, N. de Jong. Pressure-dependent attenuation and scattering of phospholipid-coated microbubbles at low acoustic pressures. *Ultrasound Med Biol*, in press, 2008.

M. Emmer, H.J. Vos, D.E. Goertz, A. van Wamel, M. Versluis, N. de Jong. Clinical relevance of pressure-dependent scattering at low acoustic pressures. *Ultrasonics*, 47:74-77, 2007.

M. Emmer, A. van Wamel, D.E. Goertz, N. de Jong, The onset of microbubble vibration, *Ultrasound Med Biol*, 33(6):941-949, 2007.

N. de Jong, **M. Emmer**, C.T. Chin, A. Bouakaz, F. Mastik, D. Lohse, M. Versluis. "Compression-only" behavior of phospholipid-coated contrast bubbles. *Ultrasound Med Biol*, 33(4):653-656, 2007.

B.J.B.M. Wolters, **M. Emmer**, M.C.M. Rutten, G.W.H. Schurink, F.N. van de Vosse, Assessment of endoleak significance after endovascular repair of abdominal aortic aneurysms: A lumped parameter model, *Med Eng Phys*, 29(10):1106-1118, 2007.

A. van Wamel, K. Kooiman, M. Harteveld, **M. Emmer**, F. ten Cate, M. Versluis, N. de Jong, Vibrating microbubbles poking individual cells: Drug transfer into cells via sonoporation, *J Control Release*, 122(2):149-155, 2006.

P. Marmottant, S. van der Meer, **M. Emmer**, M. Versluis, N. de Jong, S. Hilgenfeldt, D. Lohse, A model for large amplitude oscillations of coated bubbles accounting for buckling and rupture, *J Acoust Soc Am*, 118(6):3499-3505, 2005.

Conference proceedings

H.J. Vos, **M. Emmer**, N. de Jong. Oscillation of single microbubbles at room versus body. *Proc IEEE Ultrasonics Symp, Beijing, China*, 2008.

K. Kooiman, M.R. Böhmer, **M. Emmer**, H.J. Vos, C. Chlon, W.T. Shi, C.S. Hall, S.H. de Winter, K. Schroën, M. Versluis, N. de Jong, A. van Wamel. Oil-filled polymeric ultrasound contrast agent as local drug delivery system for lipophilic drugs. *Proc IEEE Ultrasonics Symp, Beijing, China*, 2008.

M. Emmer, H.J. Vos, N. de Jong. Dual-frequency insonation of single microbubbles. *J Acoust Soc Am, Acoustics'08 Paris, France*, 123(5):3110, 2008.

K. Kooiman, M.R. Böhmer, **M. Emmer**, H.J. Vos, C. Chlon, M. Foppen-Harteveld, M. Versluis, N. de Jong, and A. van Wamel. Ultrasound-triggered local release of lipophilic drugs from a novel polymeric ultrasound contrast agent. *Proc 10th European Symposium on Controlled Drug Delivery, Noordwijk aan Zee, the Netherlands*, 2008.

M. Emmer, G. Matte, P. van Neer, A. van Wamel, N. de Jong. Improved ultrasound contrast agent detection in a clinical setting. *Proc IEEE Ultrasonics Symp, New York, NY, USA*, 2235-2238, 2007.

W.T. Shi, M.R. Böhmer, A. van Wamel, M. Celebi, A.L. Klibanov, C.T. Chin, C. Chlon, **M. Emmer**, K. Kooiman, N. de Jong, C.S. Hall. Ultrasound therapy with drug loaded microcapsules. *Proc IEEE Ultrasonics Symp, New York, NY, USA*, 773-776, 2007.

M. Emmer, H.J. Vos, A. van Wamel, D.E. Goertz, M. Versluis, N. de Jong. Vibrating microbubbles at low acoustic pressures. *Proc International Congress on Ultrasonics, Vienna, Austria*, 2007.

K. Kooiman, **M. Emmer**, M. Harteveld, N. de Jong, A. van Wamel. Drug delivery to extravascular tissue by ultrasound-activated microbubbles. *Proc International Congress on Ultrasonics, Vienna, Austria*, 2007.

M.R. Böhmer, C. Chlon, C. Guédon, W. Shi, C. Hall, B. Schmidt, A. van Wamel, K. Kooiman, **M. Emmer**, N. de Jong. Polymer-shelled, gas containing capsules for ultrasound mediated drug delivery, *Proc 19th International Congress on Acoustics, Madrid, Spain*, 2007.

M. Emmer, A. van Wamel, D.E. Goertz, M. Versluis, N. de Jong. Threshold behavior of vibrating microbubbles. *Proc IEEE Ultrasonics Symp, Vancouver, Canada*, 1545-1547, 2006.

W. Shi, M.R. Böhmer, S. de Winter, J. Steenbakkers, **M. Emmer**, A. van Wamel, N. de Jong, C.S. Hall. Ultrasonic characterization of novel monodispersed contrast agents. *Proc IEEE Ultrasonics Symp, Vancouver, Canada*, 301-304, 2006.

A. van Wamel, K. Kooiman, **M. Emmer**, F.J. ten Cate, M. Versluis, N. de Jong, Ultrasound microbubble induced endothelial cell permeability. *Proc 9th European symposium on controlled drug delivery, Noordwijk aan Zee, the Netherlands*, 2006.

M. Emmer, J. Borsboom, A. van Wamel, M. Versluis, N. de Jong. Optical investigation of ultrasound induced encapsulated microbubble oscillations: threshold and hysteresis effects. *Proc IEEE Ultrasonics Symp, Rotterdam, the Netherlands*, 577-578, 2005.

C.T. Chin, A. van Wamel, **M. Emmer**, N. de Jong, C.S. Hall, A.L. Klibanov. Mechanisms of ultrasonically-mediated drug delivery: high speed camera observations of microbubbles with attached microbead. *Proc IEEE Ultrasonics Symp, Rotterdam, the Netherlands*, 142-143, 2005.

P. Marmottant, S. van der Meer, **M. Emmer**, M. Versluis, N. de Jong, S. Hilgenfeldt, D. Lohse. A model for large amplitude oscillations of coated bubbles accounting for buckling and rupture. *Proc IEEE Ultrasonics Symp, Rotterdam, the Netherlands*, 575-576, 2005.

A. van Wamel, K. Kooiman, **M. Emmer**, F.J. ten Cate, M. Versluis, N. de Jong. Microbubbles reforming Endothelium. *Proc 5th International Symposium on Therapeutic Ultrasound, Boston, MA*, 2005.

Abstracts (selection of)

H.J. Vos, **M. Emmer**, N. de Jong. Radial manipulation of single microbubbles. *13th European Symposium on Ultrasound Contrast Imaging, Rotterdam, the Netherlands*, 13-14, 2008.

K. Kooiman, M.R. Böhmer, **M. Emmer**, H.J. Vos, C. Chlon, M. Foppen-Harteveld, N. de Jong, and A. van Wamel. A new drug delivery system for lipophilic drugs using polymeric ultrasound contrast agents. *13th European Symposium on Ultrasound Contrast Imaging, Rotterdam, the Netherlands*, 34-35, 2008.

W.T. Shi, M.R. Böhmer, A. van Wamel, M. Celebi, A. L. Klibanov, C. Chin, **M. Emmer**, K. Kooiman, N. de Jong, C. S. Hall. Ultrasound therapy with drug loaded microcapsules. *The Leading Edge in Diagnostic Ultrasound Annual Conference, Atlantic City, NJ, USA*, 2008.

A. van Wamel, V. Garbin, H.J. Vos, M. Overvelde, J. Sijl, **M. Emmer**, D. Lohse, M. Versluis, N. de Jong. Targeted versus free circulating ultrasound contrast agents: Towards new molecular imaging strategies. *World Molecular Imaging Congress, Nice, France*, 2008.

M. Emmer, H.J. Vos, A. van Wamel, D.E. Goertz, M. Versluis, N. de Jong. Vibrating microbubbles at low acoustic pressures. *12th European Symposium on Ultrasound Contrast Imaging, Rotterdam, the Netherlands*, 84, 2007.

N. de Jong, H.J. Vos, B. Dollet, M. Overvelde, V. Garbin, A. van Wamel, S. van der Meer, **M. Emmer**, M. Versluis, D. Lohse, A. Bouakaz. Spherical, rectangular, and triangular bubble vibrations. *12th European Symposium on Ultrasound Contrast Imaging, Rotterdam, the Netherlands*, 78-80, 2007.

M. Emmer, J. Borsboom, A. van Wamel, M. Versluis, N. de Jong. The onset of bubble vibration. *11th European Symposium on Ultrasound Contrast Imaging, Rotterdam, the Netherlands*, 60-61, 2006.

A. van Wamel, K. Kooiman, **M. Emmer**, F.J. ten Cate, N. de Jong. Ultrasound contrast boosted efficacy of therapeutic agents. *Bubbleconference Chicago, IL, USA*, 2006.

M.R. Böhmer, S. de Winter, J. Steenbakkers, C. Hall, W. Shi, A. van Wamel, **M. Emmer**, N. de Jong. Synthesis, acoustic and optical characterization of monodisperse polymer-shelled ultrasound contrast agents. *11th European Symposium on Ultrasound Contrast Imaging, Rotterdam, the Netherlands*, 10-12, 2006.

PhD portfolio summary

Name PhD Student: Marcia Emmer
Erasmus MC Dep.: Biomed. Engineering
Research School: Coeur

PhD period: May 2004-Jan 2009
Promotors: N. de Jong/T. van der Steen
Supervisor: -

PhD Training	Year	Workload (ECTS)
General academic skills		
Biomedical English writing and communication (NIHES)	2004	3
Research skills		
Classical methods for data analysis (NIHES)	2004	6
In-depth courses		
Animal imaging workshop (MOLMED)	2008	0.9
Medical Imaging - 1, Principles, ultrasound and magnetic resonance, (ESMP, Archamps, France)	2006	1.5
Cardiovascular imaging and diagnostics (COEUR)	2006	1.5
Mastercourse Medical Acoustics (Biomedical Engineering, University of Twente)	2005	5
International conferences		
IEEE International Ultrasonics Symposium (Beijing, China)	2008	0.9
Acoustics'08 (Paris, France)	2008	1.8
The thirtheenth European Symposium on Ultrasound Imaging (Rotterdam, the Netherlands)	2008	0.6
IEEE International Ultrasonics Symposium (New York, NY, USA)	2007	0.9
International Congress on Ultrasonics (Vienna, Austria)	2007	1.2
The twelfth European Symposium on Ultrasound Imaging (Rotterdam, the Netherlands)	2007	0.6

PhD Training	Year	Workload (ECTS)
International conferences (continued)		
IEEE International Ultrasonics Symposium (Vancouver, Canada)	2006	0.9
ISTU6 - International Symposium on Therapeutic Ultrasound (Oxford, UK)	2006	1.2
SPIE Medical Imaging Conference (San Diego, CA, USA)	2006	1.8
The eleventh European Symposium on Ultrasound Imaging (Rotterdam, the Netherlands)	2006	0.6
IEEE International Ultrasonics Symposium (Rotterdam, the Netherlands)	2005	0.9
The tenth European Symposium on Ultrasound Imaging (Rotterdam, the Netherlands)	2005	0.6
Seminars and workshops		
Workshop Subsidie aanvragen (NWO, Den Haag)	2007	3
Ultrasound contrast agents: theory and experimental results (IEEE course, Vancouver, Canada)	2006	0.15
Nonlinear acoustics and harmonics imaging (IEEE course, Vancouver, Canada)	2006	0.15
Fundamentals of medical image processing and analysis (SPIE course, San Diego, USA)	2006	0.15
Recent trends in beamformation in medical ultrasound (IEEE course, Rotterdam)	2005	0.15
Didactic skills		
Presentatietechnieken: “the art of presenting physics” (FOM course, Utrecht)	2006	0.9
Other		
Loopbaantraining (FOM course, Utrecht)	2007	3
Doelgericht werken en plannen (FOM course, Utrecht)	2004	0.6

Teaching activities	Year	Workload (ECTS)
Supervising practicals and excursions		
Animal imaging workshop (MOLMED)	2008	0.4
Supervising student project		
Bachelor project	2007	1.5